Ion Solvation Dynamics in Helium Nanodroplets

Simon Høgh Albrechtsen

PhD Dissertation

Department of Physics and Astronomy
Aarhus University
Denmark

Originally submitted on
July 24, 2024
Revised version finished on
September 23, 2024

Preface

This thesis was submitted to the Graduate School of Natural Science of Aarhus University on the 24th of July, 2024. The printed version that you are currently reading includes minor revisions, and was completed on the 23rd of September, prior to the PhD defence. The specific revisions are detailed below.

The revised version containes a multitude of fixed typos and minor changes of wording for better readability, largely thanks to helpful corrections from the two external opponents, Prof. Paul Scheier and Dr. Lionel Poisson. Due to these corrections, a mistake in Eq. (5.7) was also fixed.

A mistake in the code producing Fig. 2.2 was fixed. In the corrected version, taking the droplet size distribution into account lessens leads to a smaller change in the doping probability as a function of doping pressure curve. The conclusions drawn from the figure remain the same. The format of the figure has been changed, combining the previous four panels into two. All of related math presented in Section 2.5 remains unchanged.

Contents

Summary in English

This thesis describes an experiment measuring the initial solvation dynamics of an ion that is introduced into a liquid helium droplet, with atomic resolution and femtosecond time resolution. The response of a solvent when a solute changes state has previously been measured by ultrafast time-dependent spectroscopy and x-ray scattering. However, no experiment has previously measured the solvation dynamics that follow when an isolated ion is first introduced to a solvent.

The measurement is based on a pump-probe scheme, realized by two femtosecond laser pulses. The initial system is a helium nanodroplet doped with one alkali atom on the surface and one xenon atom in the interior. The pump pulse ionizes the alkali atom, initiating the solvation of this into the liquid helium, which involves the building of a solvation shell of helium atoms around the ion. The probe pulse ionizes the xenon atom, and the created xenon ion repels the alkali-helium solvation complex from the droplet. The number of helium atoms attached to the alkali ion is measured by time-of-flight mass spectrometry realized in a velocity-map-imaging spectrometer. The distribution of this number of helium atoms is measured as a function of the time delay between the pump- and probe-pulses.

It is found that the first few helium atoms attach at a constant rate and that the distribution of the number of attached He atoms is Poissonian. It is found that Na^+, Li^+ and K^+ attach their first 5, 3 and 11 helium atoms at a rate of 1.8 He/ps, 1.8 He/ps and 1.7 He/ps respectively. This is in good correspondence of TDDFT simulations of the process. Furthermore, the amount of binding energy dissipated to the droplet has been measured as a function of time, finding that the average amount of dissipated energy follow the expectation of macroscopic thermodynamics.

The distribution of distances between the xenon atom and the alkali atom in the droplet has been measured, based on the kinetic energy that the alkali ion gains when both are ionized at the same time. The distribution corresponds well with the distribution of droplet radii. This technique is applied to the above described experiment, resolving the solvation dynamics in terms of the alkali-xenon distance. New insight into the mechanisms of the ion ejection from the droplet is obtained, as well as a potential method for measuring the droplet size dependence of alkali ion solvation.

Resumé på Dansk

Denne afhandling beskriver et eksperiment der måler den indledende opløsningsdynamik af en ion der introduceres ind i en helium dråbe, med atomar opløsning og femtosekund tidsopløsning. Responsen af et solvent efter et opløst stof ændrer tilstand er tidligere blevet målt med ultrahurtig tidsopløst spektroskopi og røntgenspredning. Intet eksperiment har dog tidligere målt opløsningsdynamikken der sker når en isoleret ion først introduceres til et solvent.

Målingen er baseret på et pumpe-probe skema, opnået ved brug af to femtosekund laserpulser. Startsystemet er en heliumdråbe dopet med et alkali-atom på overfalden og et xenon-atom indeni. Pumpepulsen ioniserer alkali-atomer, og starter dermed opløsningen af denne ion ind i heliumvæsken, hvilket involverer opbyggelsen af opløsningsskaller rundt om ionen. Probe pulsen ioniserer xenon-atomet, og den dermed skabte xenon-ion frastøder alkali-helium opløsnings komplekset fra dråben. Antallet af helium atomer der sidder fast på alkali ionen måles med flyvetids (eng. time of flight) spektroskopi, opnået i et et hastighedsafbildnings (eng. velocity map imaging) spektrometer. Fordelingen af dette antal af helium atomer måles som funktion af tidsforskellen mellem pumpe- og probe-pulsen.

Det findes at de første få heliumatomer sætter sig fast ved en konstant rate, og at fordelingen af det fastsatte antal er Poisson-agtig. Det findes at Na^+, Li^+ and K^+ binder deres først 5, 3 og 11 helium atomer med en rate af henholdsvis 1.8 He/ps, 1.8 He/ps and 1.7 He/ps. Dette er i god overensstemmelse med TDDFT simuleringer af processen. Endvidere er mængden af bindingsenergi der optages i dråben blevet målt som funktion af tid, og det findes at den gennemsnitlige mængde optaget energi følger forventningen fra makroskopisk termodynamik.

Fordelingen af afstande mellem xenon-atomet og alkali-atomet i dråben er blevet målt, baseret på den kinetiske energi som alkali ionen får når begge ioniseres samtidigt. Fordelingen stemmer godt overens med fordelingen af dråberadier. Denne teknik er brugt på det ovenstående eksperiment for at opløse opløsningsdynamikken i forhold til alkali-xenon afstanden. Dette giver ny indsigt i de mekanismer der skubber alkali ionen ud af dråben, så vel som en potentiel måling af dråbestørrelses afhængigheden af alkali ion opløsning.

Acknowledgments

Firstly, I need to thank my PhD supervisor Prof. Henrik Stapelfeldt, for his guidance, enthusiasm, curiosity, never-ending stream of ideas and for his patience and trust in my process. I want to thank him for being very involved in the work, while always making me feel that my opinions and ideas mattered.

I thank the rest of Femtolab group. Adam S. Chatterley, Constant A. Schouder and Albert V. Muñoz shaped a new bachelor student into a self-sufficient PhD student, and I thank them for this, and for the good times in the lab. Jeppe Kjædegaard Christensen for being my closest collaborator for what I consider to be the best part of my work. I thank the ever-present Henrik Høj Kristensen, for continuous sparring and for being a great travel-buddy. Lorenz Kranabetter and Rico M. P. Tanyag for their technical expertise. Nicolaj T. Jyde, Emil Hansen, Jean Goudot, Christian E. Petersen and Flora A. K. Hübschmann for ongoing discussions and for creating a great working environment. I need to thank Jan Thøgersen for his enduring technical support, guidance and expertise. Torben Hyltoft, Rene Warthoe, Tommy Kessler, Erik Ejler and Jeppe Mikkelsen for mentoring me in their technical skills and solving so many issues. I also need to thank Henrik S., Christian and Jean for their valuable feedback and corrections for this thesis.

Thanks to everyone I met during my short stay at Attolab and ISMO in Paris-Saclay. And a special thanks to the participants and organizers of the QFC 2022 and 2024 conferences, which were especially inspiring. Thanks to Manuel Barranco, Martí Pi, Ernesto García-Alfonso and Nadine Halberstadt for the fantastic TDDFT simulations and for many valuable discussions. A genuine thanks to the three referees of the solvation paper [2], because we learned so much during the thorough review process.

I acknowledge and admire the work that goes into developing the open source software critical to the work presented in this thesis, with a special mention of SciPy, NumPy, Matplotlib, the LaTeXclass Memoir and Pymepix.

Lastly, I want to thank my friends and family for their enduring support, I could not have done it without you.

Simon Høgh Albrechtsen,
Aarhus, September 23, 2024.

List of publications

The work presented in this thesis has lead to the following publications.

[A1] *Observing the primary steps of ion solvation in helium droplets*
Simon H. Albrechtsen, Constant A. Schouder, Albert Viñas Muñoz, Jeppe K. Christensen, Christian Engelbrecht Petersen, Martí Pi, Manuel Barranco, and Henrik Stapelfeldt
Nature, 623(7986):319–323, November 2023, doi: 10.1038/s41586-023-06593-5

[A2] *Laser-induced Coulomb explosion of heteronuclear alkali-metal dimers on helium nanodroplets*
Simon H Albrechtsen, Jeppe K. Christensen, Rico Mayro P. Tanyag, Henrik H. Kristensen, and Henrik Stapelfeldt
Phys. Rev. A., 109:043112, March 2024, doi: 10.1103/PhysRevA.109.043112

The work presented in this thesis is expected to also lead to the following future publications. All titels and author lists are subject to change.

[B1] *Solvation dynamics of K^+ and Li^+ ions in helium droplets*
Jeppe K. Christensen, Simon H. Albrechtsen, Constant A. Schouder, Tomás González-Lezana, Albert Viñas Muñoz, Christian Engelbrecht Petersen, and Henrik Stapelfeldt
In preparation

[B2] *Measuring the distance between surface- and inner-bound dopants in helium droplets*
Simon H. Albrechtsen, Jeppe K. Christensen, Constant A. Schouder, Albert Viñas Muñoz, Christian Engelbrecht Petersen, and Henrik Stapelfeldt
In preparation

[B3] *Probing the droplet size dependence of ion solvation dynamics in helium droplets*
Simon H. Albrechtsen, Jeppe K. Christensen, Constant A. Schouder, Tomás González-Lezana, Christian Engelbrecht Petersen, and Henrik Stapelfeldt
In preparation

I have contributed to the following publication, which has not been included in the thesis.

CHAPTER 1

Introduction

This chapter will give an introduction to the subject of the thesis, a brief historical overview of earlier work, and an overview of the purpose and goals of the different chapters included.

1.1 What is solvation?

The main research goal of this thesis is to measure the solvation dynamics that happen when a single ion is introduced into a liquid solvent. The concept of solvation describes the interaction between the atoms or molecules in a *solute* and the atoms or molecules in a *solvent*, creating a *solution*. According to Wikipedia; *"Solvation is the process of reorganizing solvent and solute molecules into solvation complexes and involves bond formation, hydrogen bonding, and van der Waals forces."* [118]. In other words, solvation is the concept of atoms and molecules getting surrounded by solvent particles, building up *solvation shells*. This lowers the overall energy of the system, and allows the solute particles to move around freely in the liquid solvent. For many solids, it is more energetically favorable for each solid particle to be surrounded by a solvent shell than it is to be in the crystal lattice of the solid, which will therefore be *dissolved* when introduced into the liquid solvent.

One reason why solvation is interesting to study is that it is ever-present both in everyday life, in the natural sciences, and especially in life sciences. Almost all

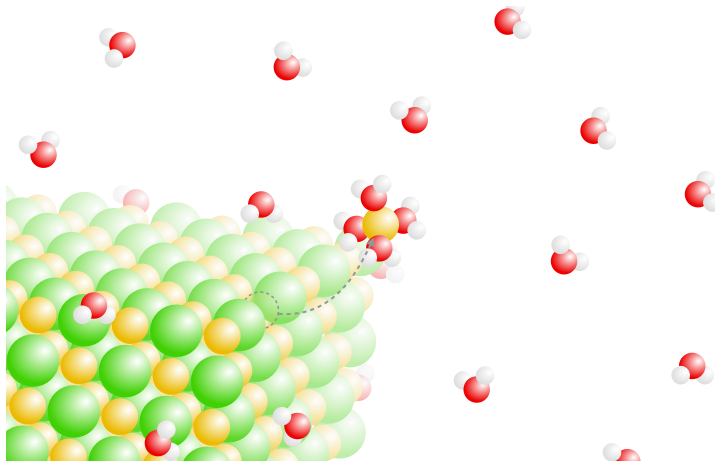

Figure 1.1: Schematic drawing of a salt (NaCl) crystal, just after it is put in contact with water. A single Na^+ ion has just left its position in the crystal, and a solvation shell of water molecules starts to form.

chemical reactions, both in research and in industry, happen between molecules in solution. Our bodies are made up of about 60% water, because they are mostly one large and very complex mix of different solutions.

On a macroscopic level, solvation has been studied for centuries. Most properties are therefore very well understood, for example, how much salt (NaCl) can be dissolved in a certain amount of water and how much heat is released in this exothermic process, and how much the entropy of the system changes. However, these thermodynamic quantities only describe the change between the initial steady state system (like a salt crystal and a volume of pure water) and a final steady state system (like the salt dissolved in the water).

Let's take a closer look at the time dynamics of dissolving a salt crystal in water. Fig. 1.1 illustrates the first step of solvation, which must be when some arbitrary ion on the surface of the crystal is removed from its lattice position, and starts getting surrounded by a solvation shell of water molecules. If we want to measure the solvation dynamics of this single ion, we should thereby measure how quickly this solvation shell builds up, as well as how quickly the binding energy of the solvation shell is dissipated into the bulk. Finding a way to measure these observables experimentally is the main goal of this thesis.

1.2 Previous solvation dynamics studies

Previously, other observables than the building of the solvation shells have been studied experimentally. The presence of the solute changes the solvent by building solvation shells, but the solute itself is also affected by the presence of the solvation shell. For instance, the spectra of different molecules are changed by the presence of different solvents, which is referred to as "solvent shifts" [93]. This enables the measurement of solvation dynamics through time-resolved spectroscopy.

For example, a molecule can be electronically excited, changing its charge distribution and the optimal arrangement of the solvation shell. Therefore, the solvent molecules will relocate and reorient themselves to the more favorable configuration, and during this reorganization, the solvent shift of the spectrum of the excited molecule changes. This has been measured by time-resolved pump-probe spectroscopy, finding that the solvent relaxes on a timescale of picoseconds [54, 56], or in some cases 50 fs [55]. The solvent relaxation dynamics are important to understand and describe the effect of solvents in chemical reactions like electron- and proton-transfer [64].

More recently, the structure of molecules and their solvation shells in solution can be probed by a technique called X-ray solution scattering, and advancements in XFEL technology has enabled time-resolved X-ray solution scattering (TRXSS) measurements studying dynamics on the picosecond and femtosecond timescales. This has been used to probe photoinduced molecular reactions in solvents, and how the solvation shell changes during these reactions [53, 59].

All of these previous experiments measure how quickly the solvent adapts to a change in the solute. Measuring how quickly the solvation shells build up during the initial solvation process has however escaped real time observation. One obstacle is the ability to accurately control when the initial solvation starts. Another is the ability to measure the number of solvent particles in the solvation shell at a given time after this start of solvation.

1.3 Solvation dynamics in helium droplets

The technique presented in this thesis differs from previous work on solvation dynamics in several ways. The solvent used is liquid helium in the form of a nanodroplet. These droplets are doped with neutral alkali atoms, which sit just outside the surface of the droplets in a dimple structure[40, 107], as illustrated in

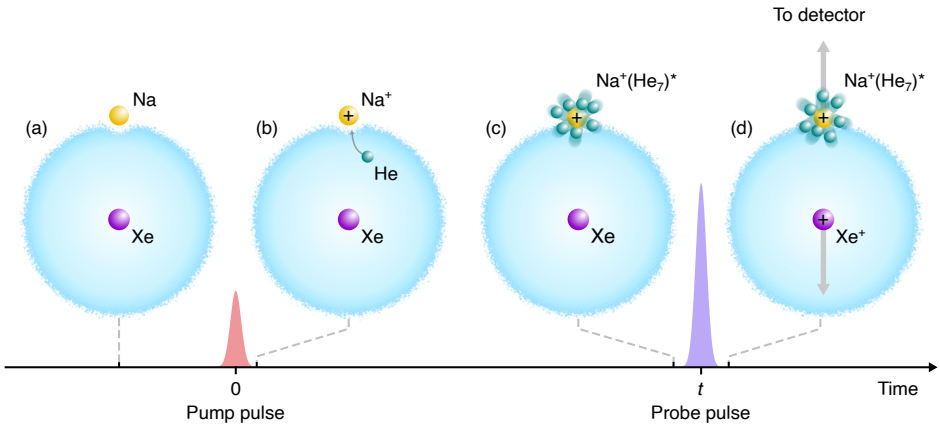

Figure 1.2: Schematic drawing of an experiment that measures the solvation dynamics of Na^+ ions in helium droplets. (a) Initial configuration of the doped droplet. (b) Just after the solvation has been started by the probe pulse. (c) Just before the probe pulse. (d) Just after the probe pulse, where the created Na^+He_n complex is ejected from the droplet.

Fig. 1.2(a). The droplets are cold [113], which means that the initial structure of the alkali on the droplet is very well known. The alkali atoms can be ionized at a very precise moment in time by a femtosecond laser pulse, whereby an alkali ion is created at a well-defined distance to the nearby helium droplet surface. Since the ion-helium attraction is much stronger than the neutral-helium attraction, the ion will get solvated into the droplet, as illustrated in Fig. 1.2(b-c). Thereby, the solvation of an alkali ion has been started at a well-defined time.

To measure the solvation dynamics, we need to be able to measure the size of the solvation complex at a given time after the solvation has started. To enable this, the initial droplet is doped with a single xenon (Xe) atom which will be located inside the droplet [10], like shown in Fig. 1.2(a). This Xe atom is used as a site that can be ionized by a second femtosecond laser pulse. The Coulomb repulsion of the newly created Xe^+ ion will eject the alkali ion and its solvation shell from the helium droplet, see Fig. 1.2(d). Once the solvation complex is free from the droplet, the number of attached He atoms can be measured by Time of Flight mass spectrometry, which has previously been realized without time resolution in electron impact ionization studies [8, 43, 92]. By controlling the time delay between the two laser pulses, we can measure the time dynamics of how the solvation shell builds up. Because each solvation complex must correspond to a

certain amount of binding energy dissipated to the droplet, we are furthermore able to measure the amount of dissipated energy as a function of time.

1.4 Experiments beyond solvation

In the experiment, we are not only able to measure the mass of the created ions, but also their kinetic energies. This kinetic energy can be used to measure the distance between the alkali-helium complex and the Xe^+ ion just after both are ionized.

To investigate this further, a separate experiment was made where both the alkali and the xenon atom were ionized by the same laser pulse. This was done to further the understanding of the structure of the co-doped droplets which form the basis of the solvation experiment. However, this experiment also provides interesting observables that relate to the radius of the helium droplets, the position of the xenon atoms, and the distributions of these.

Applying this new analysis, we are able to resolve the solvation results in terms of the distance between the alkali atom and the xenon atom. This is interesting, because it illustrates how the strength of the kick which the alkali-helium complex receives to leave the droplet affects the experimental results. Also, it gives a potential avenue to explore droplet size effects in the experiment, although this effect is inevitably convoluted with the exact position of the xenon atom.

One last experiment is presented in the thesis, concerning the experimental measurement of the internuclear separation distribution of the mixed alkali heterodimers on helium droplets. Experimentally, this study is related to the other experiments presented in this thesis, and it also determines an initial distance between two ions based on their final kinetic energies. Furthermore, it is enabled by the use of a specifically developed coincidence filter, which separates the different recorded ions according to which homo- or hetero-dimer they originated from. This provides an extension of earlier work on the alkali homodimers[62, 63], and enables the future measurement of the rotational and vibrational dynamics of the heterodimers. Furthermore, it points the way towards possible future extension of the solvation measurement, which could enable measuring the formation of complexes between alkali ions and molecules inside the droplets.

1.5 Overview of chapters

Chapter 1 introduces solvation, gives a brief overview of previous experimental studies of solvation dynamics, and an introduction to the work of this thesis in the context of this earlier work.

Chapter 2 introduces to the subject of helium droplets, the basic properties of liquid helium and superfluidity. It also introduces how helium droplets can be made and doped in the lab, and goes into some detail about the size distribution and statistics of the doping process, as this is critical for the understanding of the experiments presented in later chapters.

Chapter 3 gives a thorough overview of the experimental setup, and the most important experimental techniques needed to realize the experiments. This is split into three parts: 1: The vacuum chambers including helium droplet creation and doping. 2: The laser setup including laser systems, optical setup and pulse characterization. 3: Ion detection, including the VMI spectrometer and ion detection with TPX3Cam.

Chapter 4 gives a brief overview of some data analysis methods that are common to all experiments in the thesis.

Chapter 5 treats the experiment on ion solvation in helium nanodroplets. This includes an introduction to the principle of the experiment, previous related work, the experimental setup, a detailed account of the data analysis that yields the helium attachment rate to the alkali ions and the rate of dissipation of the binding energy of the solvation complexes. This is treated for three different alkalis: Sodium, lithium and potassium.

Chapter 6 introduces the second experiment, where the distribution of distances between the xenon atom and alkali atom in a co-doped helium droplet is found.

Chapter 7 combines the results of Chapter 5 and Chapter 6 to resolve the helium attachment rate and energy dissipation rate in the solvation experiment in terms of the distance between the alkali atom and the xenon atom.

Chapter 8 introduces an experiment where distribution of internuclear distances of alkali heterodimers can be extracted using coincidence filtering, even when

a mixed ensemble of many different homo- and hetero-dimers is present on the helium droplets.

Chapter 9 Gives a summary and conclusion of the work presented in the thesis, and an outlook of potential future experiments extending the work.

CHAPTER 2

Helium Droplets

Helium nanodroplets have many unique and special properties, that shape and enable all of the experiments presented in this thesis. This chapter gives an overview of these properties, starting with helium as an element, then liquid helium in the normal fluid and superfluid phases, and finally discussing the creation, size distribution and doping of helium droplets.

2.1 Helium

Helium (He) is the second element in the periodic table, and the lightest noble gas. It exists in two stable isotopes, ^{4}He with an abundance on earth of 99.99987% and ^{3}He with an abundance of 0.00013% [20]. In the following, ^{4}He will be referred to simply as He, due to the extreme rarity of ^{3}He.

As an element, helium has many useful and interesting physical and chemical properties. Chemically, it is the least reactive out of all elements, which is of course very useful in experiments where chemical reactions are to be avoided. It has an ionization potential of 24.6 eV and its first electronically excited states lies 19.8 eV above its ground state [60]. This means that helium is very transparent to light, which is very useful when used in conjunction with high intensity laser pulses. When kept below $\sim$25 bar, helium does not have a solid phase. At atmospheric pressure, it transitions from gas to liquid phase at 4.2 K, and it remains a liquid all the way down to 0 K. This very low gas-to-liquid transition makes it very useful

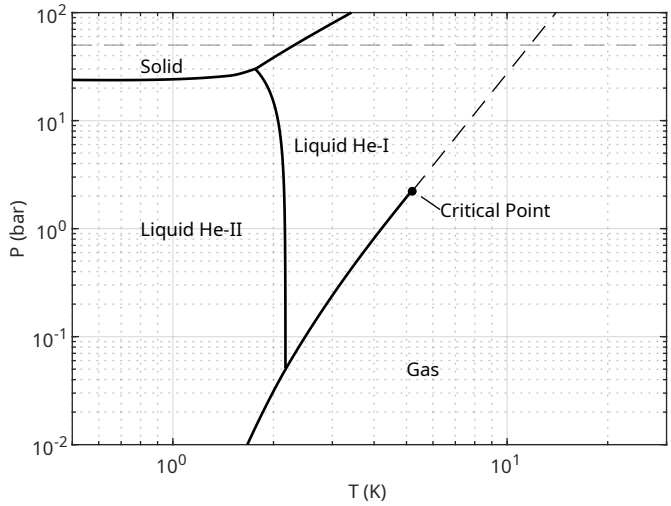

Figure 2.1: The PT phase diagram of ^{4}He, showing the borders between the solid, gaseous, normal fluid (He-I) and superfluid (He-II) phases in thick black lines. A dashed gray line marks 50 bar, the stagnation pressure used for creating helium droplets in all experiments presented in this thesis. The black dashed line shows an adiabatic expansion, ending at the critical point. Data taken from [12].

for cryogenic cooling applications. Furthermore, there are two distinct phases of liquid helium which will be discussed in detail later in this chapter.

All of these unique properties enable the use of helium as a matrix to cool, assemble and contain structures of atoms and molecules for scientific experiments [113]. When small clusters of liquid helium are used, it is even possible to study the interaction of single atoms and molecules in a liquid, which is the overarching topic of this thesis.

2.2 Liquid helium and superfluidity

The phase diagram of ^{4}He shown in Fig. 2.1, shows a remarkable property of this element: It has two distinct liquid phases, He-I and He-II. He-I is a regular fluid, with classical thermodynamic and mechanical properties. However, when this fluid is further cooled, it undergoes a phase transition into He-II, which is a superfluid. The fundamental property of the superfluid is that a particle moving

through it will experience no friction and no viscosity when it moves slower than a characteristic velocity known as the Landau velocity $58\,\mathrm{m\,s^{-1}}$. Kaptiza first reported that He-II has a remarkably lower viscosity than He-I, and speculated that He-II could be a superfluid [57]. Landau later predicted theoretically that a particle moving below the Landau velocity would feel no viscosity at all [69], and for these studies of superfluidity he was awarded the Nobel Prize in Physics in 1962. This property was later measured to hold for single ions, where the drag on an ion was measured to vanish for velocities lower than the Landau velocity, and suddenly rise for velocities above [5].

He-II has a very high heat conductivity [89]. This can also be understood through Landaus theoretical treatment of He-II, which describes two coexisting states in the liquid: The superfluid fraction and the normal fluid fraction. If heat is applied to one end of a bath of He-II, this heat can be absorbed by the liquid converting some of the superfluid fraction into normal fluid. This normal fluid can then exchange position with superfluid from the other (cold) end of the bath, where it can deliver heat by getting cooled back down to a superfluid. As these two fluids have no mutual friction, they can move in opposite directions without resistance. Thereby, this convective heat transfer cycle is very effective.

2.3 Droplet creation

For the experiments in this thesis, the droplets are created by continuously expanding high pressure, cold helium gas into vacuum. This further cools the gas, which condenses into small droplets of liquid. Other droplet creation schemes exist, with the most used alternative being liquid break up [113], however, in the following, the discussion will be limited to the gas condensation scheme which has been used for all experiments presented in this thesis.

To understand this expansion, it is useful to look at the phase diagram of helium, shown in Fig. 2.1. For all experiments in this thesis, the pressure of the helium before expansion was 50 bar, while the temperature is varied in the range 12 K to 25 K. Furthermore, the expansion happens through a 5 µm round orifice, a standard in the field, which will be described in further detail in Section 3.2. As seen in Fig. 2.1, these expansion temperatures are above the crossing point between the adiabatic expansion leading to the critical point (black dashed) and the 50 bar pressure line (gray dashed). Thereby, the adiabatic expansion of the gas will only reach the liquid phase below the critical point, or in other words, the

helium will condense into a liquid from gas phase. These expansion conditions are called "sub-critical" conditions and are in contrast to "super-critical" conditions, which behave more like a liquid being expanded into the vacuum and breaking up into droplets [113]. Importantly, the sub-critical expansion leads to small ($\sim$1000-20000 atoms in each) and well characterized helium droplets.

A short time after leaving the expansion nozzle, the helium has expanded and condensed into separate independent droplets in vacuum. He atoms will evaporate off the droplets, and cool them further. The droplets will reach a final temperature of 0.37 K after about 1 ms [113]. At this temperature, liquid helium has a dielectric constant of $\varepsilon_r = 1.0057$ [26, 72]. Importantly, this temperature is below the lambda point 2.18 K [12], and the helium droplets are therefore expected to be superfluid. Experimental proof of the superfluid properties of the relative small helium droplets was historically difficult to obtain. However, one often cited observation of droplet superfluidity is reference [45], which measured the rotational spectrum of OCS molecules embedded inside helium droplets. It was found that the rotational spectrum was well resolved into sharp lines, corresponding to the molecules rotating freely in the droplets. Furthermore, the experiment was repeated with ^{3}He droplets, which are not expected to be superfluid, and correspondingly, the rotational spectrum of OCS lost its sharp features, corresponding to a non-free rotation in a normal fluid.

From the same experiment [45], the relative populations of the rotational states were extracted, resulting in a measured rotational temperature of 0.37 K. This shows that dopants in the droplets are efficiently cooled down to the droplet temperature, without any heating of the droplets. Even when heating the droplet on purpose by collisions with gas molecules, only a minor increase in droplet temperature is seen [51]. The reason for this is that the superfluid droplet effectively equilibrates the temperature across the droplet due to its high heat conductivity, and will thereafter cool down by evaporating helium from the surface. In total, the droplet temperature is always approximately 0.37 K, even when a large amount of energy is dissipated into the droplet. In the field, this effect is referred to as the droplets having a large "effective heat capacity"[1]. To calculate how many helium atoms are evaporated off in this process, the only quantity needed is the bulk binding energy per helium atom of 0.62 meV (5.0 cm^{-1} or 7.2 K) [113].

The created droplets are confined in a beam where the speed distribution of

[1] Although of course, only the remaining helium in the droplet is cold, while the evaporated helium is hot.

droplets is very narrow ($\Delta v/v \approx 0.01 - 0.03$) [113]. The mean droplet speed dependents on the expansion conditions, but are in the range 200 m s^{-1} to 400 m s^{-1}. This means that all the droplets in the beam can be treated as having the same velocity, which is essential when we apply the velocity map imaging (VMI) technique, as will be discussed in Section 3.5. Even with the maximum speed of 400 m s^{-1}, the droplets only move 40 cm in the time it takes them to cool down to their ultimate temperature of 0.37 K. Experimentally, the confined beam makes it possible to interact with the droplets sequentially, simply by passing them though different components, like doping cells and laser focal regions.

2.4 Droplet size distribution

When the helium droplets are created for use in an experiment, the droplet source will inevitably make a distribution of droplet sizes. Commonly, only the average droplet size is reported, however, as we will see below, the average droplet size uniquely determines the full droplet size distribution for a specific set of expansion conditions.

Average droplet sizes Experimentally recorded average droplet sizes have been reported for a range of different expansion conditions using the same 5 µm expansion orifice as is used in this work [113, Fig. 6]. The reference does not give results for the exact stagnation pressure used in this work. However, by careful visual interpolation, the expected average droplet sizes for the used conditions are given in Table 2.1. It should be noted that some variance in average droplet sizes should be expected between different droplet sources using the same 5 µm orifice. One source of this variance comes because the exact shape and size of the orifices vary somewhat[2]. As we do not have an accurate way to measure the droplet sizes produced in our specific machine, the sizes presented in Table 2.1 are taken as the best available estimate.

N Distribution To further quantify the droplet size distributions rather than just the average droplet sizes, we need to look into the experiments that measure the droplet sizes in the first place. The experiment presented in reference [74] and [50] are based on crossing a droplet beam with a molecular beam. The droplets pick

[2] I was told this by Lorenz Kranabetter, who measured it himself with a scanning electron microscope. As far as I know, this knowledge has not been published in a peer reviewed format.

T_{nozzle}	14 K	16 K	18 K	20 K	22 K	24 K
$\langle N \rangle$	13000	9000	5200	3600	2100	1200
$\langle R \rangle$	5.49 nm	4.86 nm	4.05 nm	3.57 nm	2.99 nm	2.48 nm

Table 2.1: Average helium droplet sizes for different nozzle temperatures, T_{nozzle}, 50 bar stagnation pressure, and 5 µm orifice diameter, both in terms of average number of helium atoms $\langle N \rangle$ and in terms of average hard-sphere droplet radius $\langle R \rangle$, calculated using Eq. (2.10). Average number of helium atoms read from reference [113, Fig. 6].

up the molecules, and are thereby deflected at some small angle. By measuring the distribution of these small angles, the distribution of droplet sizes can be reconstructed. The experiments find that the droplet sizes follow a lognormal distribution, which can be written as [50],

$$P(N) = \frac{1}{\sqrt{2\pi} N \delta_N} \exp\left(-\frac{(\ln N - \mu_N)^2}{2\delta_N^2} \right), \tag{2.1}$$

where N is the number of helium atoms in the droplet, δ_N and μ_N are the two parameters needed to completely describe the distribution. From this, the average N is

$$\langle N \rangle = \exp\left(\mu_N + \frac{\delta_N^2}{2} \right), \tag{2.2}$$

while the FWHM of the distribution is [21]

$$\begin{aligned} \Delta N_{\text{FWHM}} = &\exp(\mu_N - \delta_N^2 + \delta_N \sqrt{2\ln 2}) \\ &- \exp(\mu_N - \delta_N^2 - \delta_N \sqrt{2\ln 2}) \end{aligned} \tag{2.3}$$

Importantly, the data presented in reference [50] shows that the ratio of the ΔN_{FWHM} and $\langle N \rangle$ can be taken to be constant, with

$$\frac{\Delta N_{\text{FWHM}}}{\langle N \rangle} \approx 0.88. \tag{2.4}$$

Thereby, δ_N and μ_N can be calculated, giving the full droplet size distribution $P(N)$. δ_N turns out to be a constant for all sub-critical expansions, and μ_N is thereby

uniquely determined by $\langle N \rangle$,

$$\delta_N \approx 0.55, \tag{2.5}$$

$$\mu_N = \ln(\langle N \rangle) - \frac{\delta_N^2}{2}. \tag{2.6}$$

Droplet radii While expressing the droplet sizes in terms of number of helium atoms N is very useful, it is critical that we are able to relate this quantity to other expressions of droplet size, like the radius of the droplets. Density Functional Theory (DFT) is the standard of modelling the density of helium droplets, and this theoretical approach has been used to study the structure of helium droplets. Such studies find that the helium density in the center of the droplets with $N \geq 1000$ are the same as that of bulk He-II, $\rho_{\text{bulk}} = 0.022\,\text{Å}^{-3}$, regardless of droplet size [50]. At the surface however, the droplets have a region of lower density that is of equal shape and thickness across droplet sizes, characterized by the $10-90\%$ thickness of 6 Å, in good correspondence with experimental results [50]. In this thesis however, I will report the droplet radii as *hard sphere* radii, that is, assuming a consistent density of ρ_{bulk} throughout. Thereby, the hard-sphere radius R_D of the spherical droplets can be found from N as

$$R_D(N) = \left(\frac{3}{\rho_{\text{bulk}} 4\pi}\right)^{1/3} N^{1/3} = 0.222\,\text{nm} \cdot N^{1/3}. \tag{2.7}$$

Following Section A.3, Eq. (2.7) can be used to transform the droplet size distribution from N space to R_D space. As Eq. (2.7) is of the general form $R_D(N) = a \cdot N^p$, $P(R_D)$ will be a lognormal distribution with the parameters

$$\delta_{R_D} = \frac{1}{3}\delta_N, \tag{2.8}$$

$$\mu_{R_D} = \frac{1}{3}\mu_N + \ln\left(\left(\frac{3}{\rho_{\text{bulk}} 4\pi}\right)^{1/3}\right), \tag{2.9}$$

see Eq. (A.13). A few examples of these $P(R_D)$ for selected $\langle N \rangle$ relevant to this thesis are shown in Fig. 2.2(b).

One thing to note is that $\langle N \rangle$ cannot simply be substituted for N in Eq. (2.7) to calculate $\langle R_D \rangle$, due to asymmetry of the lognormal distribution. However,

following Eq. (A.19) from Section A.3.1,

$$\langle R_D \rangle = \left(\frac{3}{\rho_{\text{bulk}} 4\pi} \right)^{1/3} \langle N \rangle^{1/3} \exp\left(\frac{\delta_N}{2} \right)^{1/3}, \tag{2.10}$$

where the correction factor turns out to be $\exp\left(\frac{\delta_N}{2}\right)^{1/3} \approx 1.052$. While neglecting the correction factor would only yield a small error, it has been included in Table 2.1.

Droplet Cross Sections One property where the surface thickness of the droplets is important is the cross section. The droplet cross sections have been found to match poorly with the hard-sphere cross sections, but match well with a simple surface thickness correction to this [50],

$$\sigma_D = \pi \left(\left(\frac{3}{\rho_{\text{bulk}} 4\pi} \right)^{1/3} N^{1/3} + \Delta R_D \right)^2, \tag{2.11}$$

where ΔR_D was found experimentally to be 6.51 Å.

2.5 Droplet doping

The droplets can be doped simply by passing them through a diffuse gas. By controlling the pressure of this gas, the number of dopants introduced into the droplets can be indirectly controlled. However, due to this being a stochastic process, this will result in a distribution of the number of dopants. In the following, we will see that this distribution is a Poisson distribution.

The physical system we are describing is that of a sphere, the helium droplet, moving through a length of gas with some temperature. We assume that each collision between the helium droplet and a gas particle will result in that particle being trapped in the droplet. For each droplet size N and doping pressure p_d, this results in a Poisson distribution of the number of doped particles k, which can be written as [21, Sec. 2.4.2]

$$P(k; N, p_d) = \frac{(\beta_N p_d)^k}{k!} \exp\left(-\beta_N p_d\right). \tag{2.12}$$

This distribution of k is parametrized in terms of the doping pressure p_d and the number of He atoms in the droplet N. The parameter β_N is introduced for notational convenience, with the definition

$$\beta_N = \frac{F_{a0}\left(\infty, \frac{v_D}{\hat{v_d}}\right) L_d \sigma_D(N)}{k_B T_d}, \tag{2.13}$$

where v_D is the speed of the droplets, assumed to be equal for all droplets, $\hat{v_d} = \sqrt{2k_B T_d/m_d}$ is the most probable speed of the dopant particles, $\sigma_D(N)$ is the droplet cross section discussed above, k_B is the Boltzmann constant, T_d is the temperature of the dopant gas, L_d is the length the droplets move through gas, and F_{a0} is a correction factor for the fact that the droplets and gas particles are not stationary,

$$F_{a0}\left(\infty, \frac{v_D}{\hat{v_d}}\right) = \frac{1}{\sqrt{\pi}}\left(\frac{\hat{v_d}}{v_D}\exp\left(-\left(\frac{v_D}{\hat{v_d}}\right)^2\right) + \left(2 + \frac{\hat{v_d}^2}{v_D^2}\right)\mathrm{erf}\left(\frac{v_D}{\hat{v_d}}\right)\right), \tag{2.14}$$

where $\mathrm{erf}(x)$ is the Gaussian error function [21, Sec. 2.4.2]. We here assume that the doping gas behaves as an ideal gas.

Thereby, the distribution of the number of dopants k can be found for any given droplet size N and doping pressure p_d. An example is shown in Fig. 2.2(a), for conditions relevant to the experiments included in this thesis. The distribution is a pure Poisson distribution. This means that as the doping pressure increases, so does the average number of dopants. It is however not possible to only have droplets doped with a specific number of dopants. If $k = 1$ (single doping) is needed in the experiment, then one must choose a doping pressure that will also lead to some amount of $k = 0, 2, 3$ and so on.

As discussed in Section 2.4, the droplets are not created only in a single size, but in an ensemble with a distribution of sizes. Thereby, to describe the expected distribution of k over the ensemble of droplets described by $P(N)$, we essentially need to find the expectation value of $P(k;N,p_d)$ with respect to $P(N)$, which is

$$\langle P(k;N,p_d)\rangle_{P(N)} = \int_0^\infty P(N)\cdot P(k;N,p_d)dN. \tag{2.15}$$

$\langle P(k;N,p_d)\rangle_{P(N)}$ is shown for a droplet size distribution corresponding to $\langle N\rangle = 5200$ is shown in Fig. 2.2(a). For the figure, the integral in Eq. (2.15) was calculated numerically. It is shown that the peaks are broader in the p_d direction, when

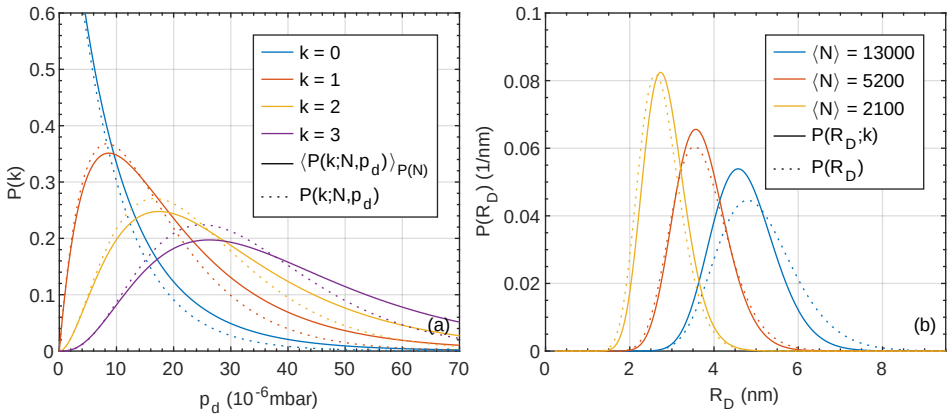

Figure 2.2: (a) the doping probability of having k dopants in droplets for the two cases of (dotted lines) all droplets have size $N = 5200$, see Eq. (2.12) and (full lines) an ensemble average over a droplet size distribution with $\langle N \rangle = 5200$, see Eq. (2.15). The parameters used to create this were $v_D = 400\,\mathrm{m\,s^{-1}}$, $L_d = 6.4\,\mathrm{cm}$, $m_d = 76\,\mathrm{u}$, $T_d = 295\,\mathrm{K}$. (b) distribution of droplet radii R_D for (dotted lines) the pure droplets and (full lines) droplets that have picked up $k = 2$ dopants. For the doped droplet size distribution, $p_d = 17.4 \times 10^{-6}\,\mathrm{mbar}$ was chosen, which optimizes having 2 dopants in the $\langle N \rangle = 5200$ ensemble of droplets, and the rest of the parameters were the same as for panel (a).

compared with $P(k;N,p_d)$ for a single droplet size $N = 5200$ in Fig. 2.2(a). The p_d that optimizes $P(k)$ for $k = 1,2,3$ and so on are the same those for a single droplet size, so using the pure Poisson distribution to plan out experiments would not be totally misguided. One especially important point for this thesis, however, is that it is impossible to create droplets which are doped with monomers, without also having the presence of dimers and trimers. And lastly, it is clear that if the doping pressure is optimized for monomer or dimer doping, then a significant fraction of the droplets will have no doping at all.

2.5.1 Size distribution of doped droplets

Some experiments require a specific k to get any signal at all from a given droplet, and thereby only address a specific part of the $P(k)$ distribution. However, as we have seen above, this will mean that we are more likely to address certain parts of the droplet size distributions $P(N)$, because certain N are more or less likely to lead to a specific k. Therefore, it is relevant to consider not only the size distribution of

pure droplets, but also the size distribution of the droplets which are doped with a specific number of dopants, which will be called $P(N;k)$. To calculate this, we simply multiply the droplet size distribution $P(N)$ with the probability of having k dopants for a droplet of size N, $P(k;N,p_d)$, and renormalize

$$P(N;k) = \frac{P(N)\cdot P(k;N,p_d)}{\int_0^\infty P(N)\cdot P(k;N,p_d)dN}. \tag{2.16}$$

The renormalization is needed to find the distribution of N for those droplets which contain k dopants, rather than the compound probability distribution of having a droplet of size N that contains k dopants.

In Fig. 2.2(b), $P(R_D;k)$ is shown for $k=2$, and for three different $\langle N\rangle$. Note that since $P(N;k)$ is not a lognormal distribution, Eq. (A.3) was applied numerically to convert to $P(R_D;k)$ using Eq. (2.9). p_d has been kept constant at the value which optimizes the probability of $k=2$ for the $\langle N\rangle = 5200$ ensemble. Comparing to the pure $P(R_D)$, see Fig. 2.2(b), it is seen that $P(R_D;k)$ is a narrower distribution in general. For the $P(R_D;k)$ for the larger $\langle N\rangle$, especially the larger droplet sizes are cut off, and the reverse is true for the $P(R_D;k)$ for the smaller $\langle N\rangle$.

Droplet evaporation One thing that has been neglected from this model is the cooling of the doped species. As discussed in Section 2.3, the droplet and dopant temperature is kept at 0.37 K by evaporating off helium, with each helium evaporated taking away 0.62 meV (5.0 cm^{-1} or 7.2 K). The average particle of an ideal gas a room temperature will have a kinetic energy of $3/2k_bT = 38.1$ meV [13, sec. 13C.2], and to cool this, 61.5 helium atoms would need to evaporate off the droplets. Furthermore, the internal energy of molecules needs to be cooled as well, which can lead to the evaporation of many hundreds of helium atoms when doping with large molecules. However, for the atomic dopants used in this thesis, this evaporation effect has been neglected.

2.5.2 Dopant positions

One property of high importance to this thesis is the positions of the dopants in the helium droplets. In general, closed shell systems are completely solvated in the helium droplet, while open shell systems like hydrogen radicals and the alkali metals reside on the surface of the droplets in a dimple structure [113]. This is essentially due to helium being electrophobic, whereby the outer-shell electron of for instance the alkalis repel helium. Thereby, it is too energetically expensive

for the system to create the bubble in the helium droplet that would be required to envelop the alkali atom inside the droplet [10]. This is summed up in the dimensionless parameter

$$\lambda_A = \rho_{\mathrm{He}} \varepsilon r_{\mathrm{min}} / (\sigma_{\mathrm{He}} 2^{1/6}) \tag{2.17}$$

commonly referred to as the Ancilotto parameter, where ρ_{He} is the number density of the helium, ε and r_{min} are the well depth and equilibrium distance of the helium-dopant pair potential and σ_{He} is the surface tension of the liquid helium. When λ_A is greater than 1.9, the dopant will reside inside the droplet, while for λ_A lesser than 1.9, the dopant will reside in a dimple on the surface. It should be noted that the larger ε and smaller r_{min} mean that all Ak^+ ions strongly prefer to be inside the droplets, measuring the dynamics of this surface to center transition is one of the major research goals of this thesis.

For the alkalis, the Ancilotto parameter model has been extended in a theoretical model to cover clusters of alkali atoms [107]. As electrostatic attraction between an alkali cluster and the droplet grows faster than the surface tension of the required bubble, for clusters larger than some critical size, the inside position is favored. This theoretical study found that Na clusters are the most easily solvated, which happens for clusters with more than 21 atoms. Critically, this means that all small clusters (oligomers) of all alkalis reside on the droplet surface. This theoretical prediction has been tested in experiments where Na, K and Rb clusters doped on helium droplets were ionized by electron impact ionization at varying electron energies [7, 9, 100]. At electron energies above the first excitation energy of helium (19.8 eV) but below the ionization energy (24.6 eV), the electrons create excited He*. This is heliophobic and will move to the surface, where it can ionize surface bound dopants by Penning ionization. At electron energies above 24.6 eV, the electron ionizes helium to create He^+, which migrates to the inside of the droplet, where it can ionize dopants located in the droplet center by charge transfer. By measuring at which energies the mass spectrometry signals of the different Ak_n^+ clusters appear, it was found that all alkali and their small clusters reside on the droplet surface. The critical sizes for submersion corresponded well with the theoretical predictions from reference [107]. Furthermore, the experiment was repeated for droplets co-doped with C_{60} and Na or Cs, to test if the added attraction of the C_{60} molecule would induce solvation of the alkali clusters [95]. It was found that the presence of the extremely polarizable C_{60} does seem to drag Na atoms and Cs dimers into the droplets. It should be noted C_{60} is many times more polarizable than any inside-bound dopant used in this thesis. Compare for instance

the experimental table values for the polarizability of C_{60} of $\alpha = 79\,\text{Å}^3$ with that of xenon of $\alpha = 4.0\,\text{Å}^3$[83].

The position of the neutral alkalis on the surface have been predicted by Density Functional Theory (DFT) calculations [2, 11, 40]. Furthermore, while the number is not directly reported in the paper, this gives how far above the hard-sphere surface (radius R_D) the alkalis reside. The energies associated with the surface position are reported both for Ak and Ak^+, as well as the inside position for Ak^+. All of these values will be very valuable for comparison with the results of the experiments presented in this thesis.

CHAPTER 3

Experimental Setup

In this chapter, the experimental setup used for all the experiments presented in this thesis will be thoroughly introduced. The focus will be to describe the setup in as much detail as necessary to reproduce the experiments, and includes both technical and methodological details. Throughout the chapter, specifications of manufacturers and part numbers will be given in parentheses after the first mention of the relevant piece of equipment.

The chapter can be roughly split into three parts: The vacuum chamber and droplet source, the laser setup and optical methods, and the ion spectroscopy and detection.

3.1 Vacuum chambers

For the best experimental conditions, it is essential to maintain a vacuum at as low pressure as possible. This section will give an overview of how this vacuum is pulled and maintained, while the following sections will go into detail about the components critical to the experiments. Note that the vacuum setup and droplet source was built by Ben Shepperson, and first described in reference [104].

A schematic of the vacuum setup is shown in Fig. 3.1. The setup is divided into four separate vacuum chambers, called the source, doping, target and supersonic source chambers. Overall, a beam of helium droplets is created in the source chamber, the droplets fly into the doping chamber where they are doped, and

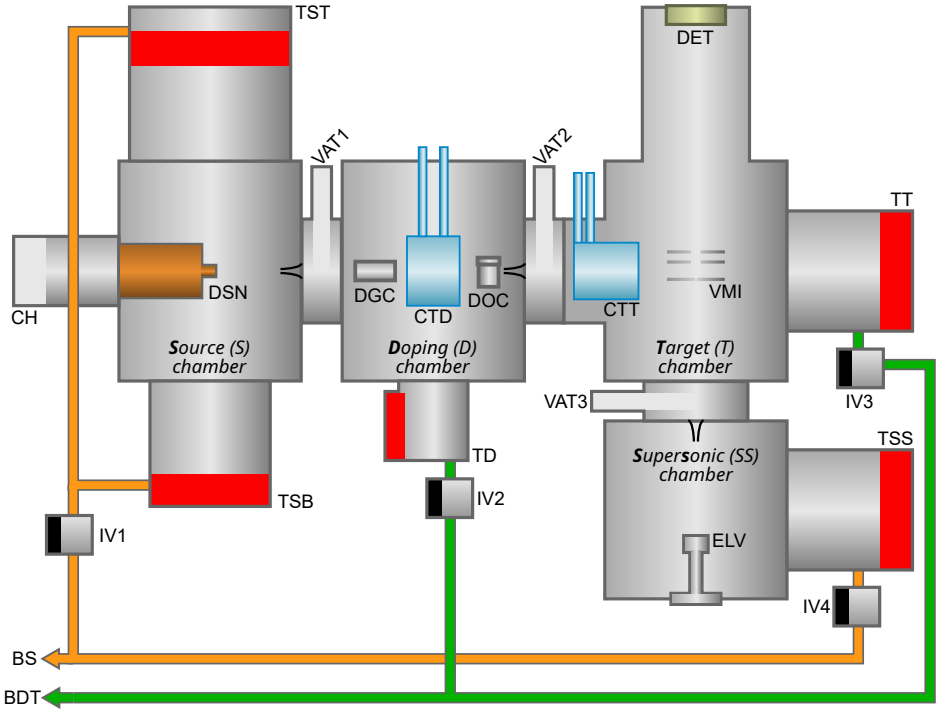

Figure 3.1: Schematic sketch of the vacuum system, not drawn to scale, and many components are missing. The abbreviations mean: TST: Source Turbopump Top, TSB: Source Turbopump Bottom, TD: Doping Turbopump, TT: Target Turbopump, TSS: Supersonic Turbopump, BS: Source Backing pump, BDT: Doping/Target Backing pump, IV1-4: Isolation Valve 1-4, VAT1-3: VAT brand chamber isolation valve 1-3, CH: ColdHead, DSN: Droplet Source Nozzle, DGC: Doping Gas Cell, DOC: Doping Oven Cell, CTD: Doping Cold Trap, CTT: Target Cold Trap, VMI: Velocity Map Imaging spectrometer, DET: Ion DETector, ELV: Even-Lavie Valve.

thereafter fly into the target chamber where the droplet beam is crossed with a beam of femtosecond laser pulses, and the resulting ions are recorded. Alternatively, a cold beam of atoms or molecules in a carrier gas can be created in the supersonic chamber by supersonic expansion, and this beam can likewise be passed into the target chamber for ionization and detection.

Practically, the chambers are made of thick stainless steel, which is mostly[1]

[1]The fact that a plate of stainless steel is not completely impermeable to gas tells us how extreme

	Turbopump		
Label	Model	N_2 pumping speed	Backing pump
TST	Pfeiffer Adixen ATH 2303M	$2150\,\mathrm{L\,s^{-1}}$	BS
TSB	Edwards STP-iXR2206	$2200\,\mathrm{L\,s^{-1}}$	BS
TD	Edwards STP-iX455	$450\,\mathrm{L\,s^{-1}}$	BDT
TT	Edwards STP-iXR1606	$1000\,\mathrm{L\,s^{-1}}$	BDT
TSS	Edwards STP-iXR1606	$1000\,\mathrm{L\,s^{-1}}$	BS
	Backingpump		
Label	Model	N_2 pumping speed	Ultimate pressure
BS	Edwards iGX600L	$600\,\mathrm{m^3/h}$	7×10^{-4} mbar
BDT	Busch Cobra BA 0100 A	$100\,\mathrm{m^3/h}$	1×10^{-2} mbar

Table 3.1: Technical specification of the turbopumps and backing pumps. Additionally, the compression ratio of all the turbopumps are (1e8 / 1e3) for (N_2 / H_2) respectively.

impermeable to gas, and thereby, "all" that is needed to create a vacuum is removing the air from inside these chambers. This is done using turbomolecular pumps.

The turbomolecular pumps, or just turbopumps, are mounted directly to vacuum chamber by ConFlat (CF) flanges, in which a copper gasket is compressed between two circular knife edges to ensure a vacuum tight seal. The operating principle of a turbomolecular pump is that individual gas atoms or molecules hit sets of rapidly spinning fan blades, and are thereby imparted with a momentum with a direction towards the back of the pump. By employing multiple stages of stators and rotors, high compression rations can be achieved. However, as collisions between the gas molecules need to be minimized, the outlets of the turbopumps need to be kept a low pressure[79, Sec. 3.4.1]. There are a total of 5 turbopumps mounted on the chamber, the technical specifications of these are given in Table 3.1.

The turbomolecular pumps are connected to two backing lines, one for the source and supersonic chambers, and one for the doping and target chambers, as seen in Fig. 3.1. The turbopumps of each chamber can be isolated from the backing line using isolation vales (IV). The source and supersonic chamber share a backing line (BS) because the gas load is highest for the source and supersonic

a condition ultra-high vacuum really is.

chambers, but only one of these chambers is used at a time. The gas load on the doping and target chambers is much lower, and they can share a backing line without lowering the vacuum performance. The backing lines are each pumped by a backing pump. The source/supersonic backing line (BS) is pumped by a dry vacuum pump (Edwards iGX600L), and the doping/target backing line (BDT) are pumped by a dry screw vacuum pump (Busch Cobra BA 0100), with technical specifications given in Table 3.1

The different chambers are connected together with pneumatic sliding gate valves (VAT Series 108 UHV), which can be closed to isolate specific chambers during experiments or maintenance. To maintain a differential pumping scheme between the chambers, the amount of gas that can pass between the chambers is restricted by the use of skimmers. A skimmer with a 1 mm opening (Beam Dynamics model 50.8) is used between the source and doping chambers. A 2 mm skimmer (Beam Dynamics, model 2) is used between the doping and target chambers, and a 4 mm skimmer (Unknown manufacturer) is used between the supersonic and target chamber.

The pressure in each chamber is monitored by pressure gauges (JevaTec ATMION standard[2]). These gauges combine a Pirani gauge and a Bayard-Alpert ionization gauge to cover the range of pressures 1000 mbar to 1×10^{-10} mbar. See reference [79, Sec. 3.3] for the operating principle of these gauge types. Separate Pirani gauges are used to measure the pressure in the backing lines BS and BDT.

If the chambers are run without gas load, the pressures in the source, doping and supersonic chambers reach well below 1×10^{-8} mbar, while the target chamber can reach below 1×10^{-9} mbar. These ultimate pressures are dictated by the rate of outgassing of atoms and molecules on the inside walls of the chambers. This can be reduced by baking the cambers by heating them to a high temperature for some days, and then cooling them back down to room temperature. While the steel chambers themselves could be heated to many hundred of degrees Celsius without damage, the vacuum gauges limit the maximum temperature of baking to about 100 °C, while the MCP detector is kept below 80 °C to avoid damage. Furthermore, the pressures in the chambers can be lowered by filling two cold traps with liquid nitrogen, thereby freezing residual gas. These are present in the doping and target chambers, and are marked as CDT and CTT in Fig. 3.1. The coldtraps are especially useful for reducing the partial pressure of water, which is often the strongest background signal in the experiment. The actual pressures

[2]The company has changed name from "VACOM" since the gauges were originally bought.

during experiments depend heavily on the actual gas load introduced by running the droplet nozzle or the Even-Lavie valve. Typical running conditions for an experiment with helium droplets might have source chamber pressures in the low 1×10^{-4} mbar range, doping chamber pressures in the 1×10^{-6} mbar range and target chamber pressures in the 1×10^{-8} mbar range.

3.2 Droplet source

The working principle of the droplet source is described in Section 2.3. Cold helium gas at a high pressure is expanded through a small orifice into vacuum, further cooling the gas in an adiabatic expansion, whereby it condenses into helium droplets.

The droplet source was designed and built by Benjamin Shepperson, based on the "Göttingen" design from Peter Toennies group [99, 105]. The specific nozzle was made by Alkwin Slenczkas group in Regensburg in 2014. A technical drawing of the nozzle can be seen in Fig. 3.2. The specific orifice used is a Plano A0200P platinum/iridium alloy aperture (Outer diameter 2 mm, hole diameter 5 µm, thickness 0.6 mm), made for electron microscopes.

The nozzle is mounted on a Sumitomo Heavy Industries RDK-408D2 cold-head, which is attached to a Sumitomo Heavy Industries F-50H compressor. It is based on the Gifford-McMahorn cooling cycle [41]. This system has a cooling capacity of 1 W at 4.2 K. A resistive heater is used to apply heat to the nozzle to keep it at a specific cryogenic temperature. This is controlled by a PID loop with a Lake Shore 331 Cryogenic Temperature Controller, which measures the temperature of the nozzle with a temperature sensitive diode.

Helium with a purity of 99.9999% is used both to ensure that the created helium droplets are without impurities, and to ensure that the nozzle does not clog from contaminants freezing on cold surfaces. The nozzle is operated with a helium pressure of 50 bar, and a temperature in the range 12 K to 25 K, giving the range of average droplet sizes shown in Table 2.1.

3.3 Droplet doping

As explained in Section 2.5, the helium droplets can be doped by passing the droplet beam through a cell containing a gas at some doping pressure p_d. In the setup, two such cells are used, to allow co-doping of two different species in the

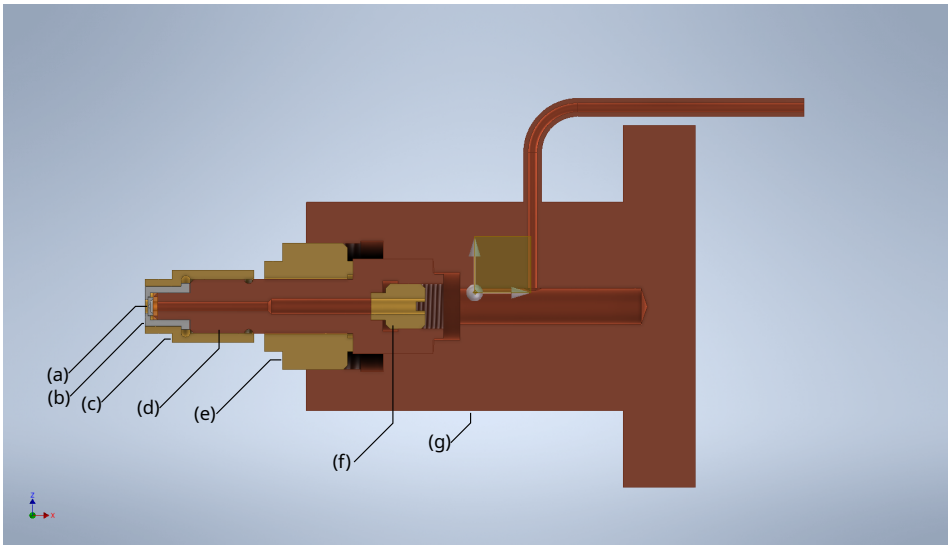

Figure 3.2: Technical drawing of the helium droplet nozzle. (a) Platinum orifice and gold gasket. (b) Stainless steel orifice cap. (c) Brass nut. (d) Copper tube. (e) Brass nut. (f) Brass holder for sintered filter. (g) Copper main body, witch is bolted onto the tip of the cold-head. An indium wire seal is used between (d) and (g). Own work, based on technical drawing provided by Alkwin Slenczka.

droplets. The first cell is referred to as the "gas cell" (DGC in Fig. 3.1), which is used for dopants that have a high enough vapor pressure at room temperature to achieve a useable doping pressure. The second cell is referred to as the "oven cell" (DOC in Fig. 3.1), and is used for dopants that need to be heated above room temperature to achieve a useable doping pressure.

3.3.1 Gas cell

The gas cell is a 7.4 cm long tube with an inside diameter of 1.4 cm. The opening which the droplets enter though has been reduced to 8 mm in diameter, while the exit opening has been reduced to 3 mm. On top of the tube there is a gas inlet, which is connected though a thin metal tube and a CF flange to the outlet of a leak valve (Kurt J. Lesker LVM Series Stainless Steel Leak Valve) on the outside of the chamber. The inlet of the leak valve is connected to what is referred to as the "doping manifold", a system of connected steel tubes and valves, to which a utility

vacuum pump (Busch Fossa FO 0035 B), a Pirani pressure gauge (Inficon PGE300), and a sample holder is connected. Gas samples can be connected directly to the manifold, replacing the sample holder with a gas tube connected to a regulator. All gas pressures below 1 bar have been found to function with the leak valve. Solid and liquid doping samples can be loaded into the sample holder, whereby a gas at its vapor pressure will be present in the doping manifold. The doping pressure can thereby be regulated by the opening of the leak valve. To rid the doping manifold of atmospheric gas after loading a new sample, the sample holder is cooled down to cryogenic temperatures with liquid nitrogen, and the whole doping manifold is pumped using the utility pump for a short time. Throughout the doping manifold, Swagelok VCR copper gasket fittings are used for the connections that regularly need to be opened and closed, securing a leak free system even after many opening-closing cycles.

3.3.2 Doping oven

The doping oven consists of multiple parts. The inside part ("crucible") is removable for cleaning and loading of sample. The outside part ("oven") remains stationary in the chamber to conserve the alignment of the setup, and is wrapped in a heating coil (Metal sheet mineral insulated coaxial cable, 40 cm length, 3.2 Ω Ohm resistance.). The droplets fly through a hole with a diameter of 3 mm, and the inside length of the oven is 17 mm. On the bottom, between the inside and outside part, the junction of a K-type thermocouple (Kapton insulated) is mounted. Lastly, a lid is placed on top of the assembly. The vapor pressure of the loaded samples is controlled by the temperature of the oven cell, which is heated by applying 12 V to the heating wire. This is controlled with a PID controller (Euroterm 3216, switching a solid state relay), which turns the heating on and off in a closed loop control scheme, according to the temperature measured through the K-type thermocouple. The system was designed by Lorenz Kranabetter to work at up to 500 °C.

All samples used in the oven cell for this thesis work were alkali metals. These need to be handled with care, due to their extreme reactivity both with water and oxygen present in the air. The alkali samples are loaded into the inner oven in a glove box filled with an inert argon atmosphere. Generally, a small lump of metal is loaded (an estimate could be 0.05 g), and pressed down to stick to the bottom of inner oven for optimal heat conductivity. Before being removed from the argon atmosphere, the sample is covered with anhydrous n-hexane, which prevents air exposure while the inner oven is loaded into the vacuum chamber and the vacuum

chamber is pumped down. The n-haxane rapidly evaporates in the vacuum and we generally see little contamination from this species in the experiment. When the alkali sample is to be changed, the inner oven is cleaned first with a weaker solvent (isopropanol, 96% ethanol) to limit explosive reactivity, then deionized water which dissolves all alkalis, and finally sonicated in acetone, which gets rid of the water.

For each experiment, the temperature of the oven is tuned to optimize the doping conditions for the specific droplet size used. When single atom alkali doping is needed, vapor pressures in the range of $\sim 5 \times 10^{-5}$ mbar used for droplets in the $\langle N \rangle \sim 5000$ size range, see [4]. One disadvantage of this control scheme is that the doping level takes about an hour to stabilize after the temperature of the oven is changed.

3.3.3 Effusive dopants in the target chamber

From both the gas cell and the oven cell in the doping chamber, doping atoms and molecules can fly in a straight line through a skimmer into the center of the VMI spectrometer, see Section 3.5, where the laser beam is focused. These are angularly confined by the skimmer, effectively creating a directional beam of doping particles. This means that at the laser focus, all of the particles move in the same direction, with a velocity dictated by the Boltzmann distribution. This beam is referred to as the "effusive beam", and it results in a characteristic narrow line of signal in the VMI images, in the direction corresponding to the droplet beam direction.

3.4 Laser setup

A schematic of the optical setup is shown in Fig. 3.3. The setup is built out of freestanding optics on a laser table, and its primary purpose is to transport the laser beam from the laser system to the vacuum chamber, while controlling the properties of the laser beam with a number of optical components. In this section, it will be discussed how these components are used to control the laser beams.

The beam path goes as follows. The 800 nm laser beam is split in two by the combination of a halfwave plate (HWP) and a thin film polarizer (TFP), into the pump beam (reflected) and probe beam (transmitted). Thereby, the division of laser power between the two beams can be controlled.

The probe beam is directed onto a long delay stage (DS2, "Schneeberger"), through a telescope (TS), and through a second delay stage (DS1, "Newport").

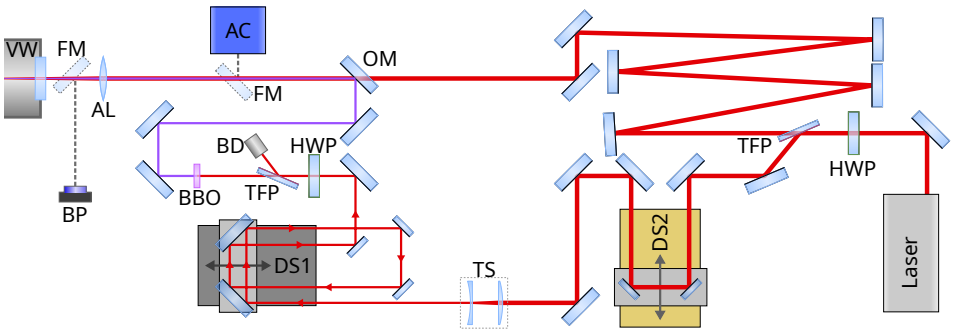

Figure 3.3: Simplified sketch of the optical setup used. HWP: Halfwave plate, TFP: Thin film polarizer, DS1/2: Delay stage, TS: Telescope, BD: Beam dump, BBO: BBO Crystal, OM: Overlap Mirror, FM: Flip mirror, AL: Achromatic lens, VW: Vacuum chamber window, BP: Beam Profiler.

The first delay stage is manually controlled, and is used for rough adjustments of the pulse timing, while the second is computer controlled, and used for scanning delays during measurements. After DS1, the probe beam is sent through a HWP and TFP power control unit, and then through a BBO crystal, which converts the 800 nm wavelength to 400 nm, through second harmonic generation. After a few bounces on 400 nm reflective mirrors to get rid of the residual 800 nm light, the probe beam is sent onto the reflective side of the overlap mirror.

The pump beam is simply sent through a series of bounces, to match the path length of the probe beam, and then through the back of the overlap mirror (OM).

The now collinear beams are sent through an achromatic lens (AL) with a focal length of 30 cm, and through a window into the target vacuum chamber. Thereby, they are focused in the center of the VMI spectrometer.

The beams can be optionally redirected in two places using flip mirrors (FM). In the first location, the beams can be redirected to an autocorrelator (AC) to measure the temporal length of the laser pulses. In the second position, the focused beam can be directed onto a beam profiler (BP), to measure the spatial profile of the focused beam.

3.4.1 Laser system

Two different laser systems have been used in the work for this thesis. Both are Titanium Sapphire (Ti:Sapph) based, and they thereby both operate at central

wavelength of 800 nm. Both are based on mode-locked oscillators, which give laser pulses with temporal lengths in the order of 10s of femtoseconds. Both are amplified by Chirped Pulse Amplification (CPA), giving pulse energies in the order of millijoules. The biggest difference between them is the repetition rate, as one operates at 1 kHz, while the other operates at 5 kHz. This makes a big difference when acquiring data, as the 5 kHz system can provide 5 times the amount of data in the same amount of time. Furthermore, the 5 kHz system provides shorter laser pulses, so in total, it is a direct upgrade over the 1 kHz system. The reason why it was not used for all experiments is that it was only acquired and installed in the last year of my PhD studies.

1 kHz **Spitfire Ace** The Spectra Physics Spitfire Ace regenerative chirped pulse amplifier is seeded by a mode-locked Spectra Physics MaiTai SP oscillator. Both operate using Ti:Sapph as the gain medium, and the central wavelength of the generated laser pulses are 800 nm, the nominal pulse length (FWHM) of the generated pulses is 35 fs. The amplifier is pumped by a Spectra Physics Empower 45 Q-swiched Nd:YLF laser. This gives measured pulse energy of 4.2 mJ at a repetition rate of 1 kHz.

Optionally, a controllable portion of the beam can be exported from the amplifier before the last pulse compression, to have a temporally long and heavily chirped pulse. In tandem with the Spitfire Ace system is a Spectra Physics TOPAS Prime Optical Parametric Amplifier (OPA), which can change the wavelength of the laser pulses while mostly conserving their short pulse lengths. Neither the uncompressed output nor the OPA were used for any experiments presented in this thesis.

5 kHz **Coherent Astrella** The Coherent Astrella HE USP is a one-box integrated laser system, consisting of a mode-locked oscillator seed laser, regenerative amplifier and pump laser. The oscillator and amplifier both use Ti:Sapph as their gain medium, and the system operates at a central wavelength of 810 nm. This system gives a nominal pulse energy of $>$2.0 mJ at a repetition rate of 5 kHz. The nominal pulse length (FWHM) is $<$35 fs. An OPA is also available to change the wavelength of the light, but this was not used for this thesis.

3.4.2 Beam splitting and power control

Halfwave plates and polarizers are used in the setup to split the beam and control their average power in the experiment. The halfwave plate rotates the linear polarization of the laser beams. In order to reduce dispersion zero-order halfwave plates are used. The thin film polarizers reflect s-polarized and transmit p-polarized light. The polarizers are placed so that they are perpendicular to the optical table and so that the laser beam is incident at the Brewster angle. Thereby, they transmit horizontally polarized light, and reflect vertically polarized light, relative to the laser table. By controlling the linear polarization with the halfwave plate, the ratio of transmitted and reflected light can be controlled. As shown in Fig. 3.3, this is used both for splitting the beam into the pump and the probe beam, and also for power control in the probe arm. These two combined provide complete control over the average power of each beam.

3.4.3 Delay stages

By controlling the relative path length of the pump and probe beam paths, the time delay between the pump and probe pulses can be controlled very accurately. This is achieved using delay stages in the setup.

Newport delay stage The primary delay stage is a Newport M-UTM100PP.1 linear translation stage [84], marked DS1 of Fig. 3.3. It has a travel range of 100 mm, a guaranteed repeatability of $\pm 1.4\,\mu$m across the full stage, and a resolution of 0.1 µm. As illustrated in Fig. 3.3, it is used in a double pass configuration, whereby the change in optical path length is four times the movement of the stage. This gives a total pulse delay range of 1.4 ns, and a guaranteed repeatability of 18.7 fs and a resolution of 1.3 fs. The stage is computer controlled, which is used to automate scans over different pump-probe delays in experiments.

Schneeberger delay stage The Schneeberger delay stage is marked as DS2 in Fig. 3.3. The stage is not computer controlled, and its position needs to be manually read off on a linear encoder with a display. It has a range of 48 cm. Typically, it is set up in a single pass configuration, where the beam is sent onto the stage and retroreflected back, thereby the optical path length can be changed by 96 cm, corresponding to $\sim$3 ns of pulse delay. This is very useful for finding the rough time overlap between the pump and probe pulse and for fine-tuning the path length.

3.4.4 Second Harmonic Generation

The fundamental Ti:Sapph laser wavelength of 800 nm is not always the optimal wavelength to use for experiments. For this reason, we often change this wavelength in the optical process of second harmonic generation. In this non-linear process, light is created which has double the frequency (half the wavelength) of the fundamental beam [78, sec. 10.5]. In the experiment, this is done in a beta barium borate crystal (BBO), which is a birefringent material with a large non-linearity coefficient [34]. Due to the dispersion of the material, the generated 400 nm light from the first part of the crystal that is hit will not necessarily be phase-matched with the 400 nm light created in other parts of the crystal, which can lead to destructive interference, and thereby a low conversion efficiency [78, sec. 10.6]. In order to mitigate this, the crystal is rotated to a certain phase matching angle, where birefringence of the crystal makes it so that the index of refraction is equal for fundamental and second harmonic wavelengths, thereby ensuring constructive interference of all the second harmonic light generated. One important note learned during the experimental work of this thesis is that the phase matching angles are given relative to the internal crystal axis, and that if the fundamental beam is not in normal incidence on the crystal, then refraction in the crystal surface has to be taken into account.

One important detail is that the fundamental wavelength will still largely be present in the beam, and needs to filtered out. In practice this is done by letting the beam reflect off of a few dielectric mirrors coated for the 400 nm second harmonic wavelength. These reflect about 99% of the 400 nm light, and a much lower fraction of the 800 nm light. In practice, 4 mirror bounces, like those shown in Fig. 3.3, are enough to reduce the remaining 800 nm light to a negligible amount.

Sum frequency generation The SHG described above can be seen as a specific case of three-wave mixing, in which the two incoming waves being the same. Another specific case of this is sum-frequency generation, where two lightwaves of different frequencies mix to form a third wave of the sum of the frequencies [78, sec. 10.7]. Like with SHG, a certain phase matching angle must be used to ensure an efficient conversion.

3.4.5 Characterizing beam focus

We assume that our beam is purely the fundamental TEM_{00} Gaussian beam mode, see reference [88, ch. 27] for a good introduction. The intensity profile follows a Gaussian distribution in the directions transverse to the propagation direction, and we thereby need to define a useful measure of the width of the beam. The *beam radius* w is therefore defined as the distance from the beam center at which the intensity has fallen to $\frac{1}{e^2}$ of the maximum value[3]. The *beam waist* is the position where w is minimized, with the minimum value denoted w_0, which could be called the beam radius at the focus[4]. When we want to characterize the beam focus, we want to measure w_0.

If a collimated laser beam with beam radius W and wavelength λ is focused by a lens with focal length f, then the beam radius in the focus will be [88, Sec. 27.6]

$$w_0 = \frac{f\lambda}{\pi W}. \tag{3.1}$$

That is, the larger the radius of the collimated beam, the smaller the radius of the focused beam. Furthermore, using a lens with a shorter focal length f will give a smaller focused beam radius w_0, and so will a beam with a shorter wavelength λ.

3.4.6 Telescopes

Telescopes are used in the setup to control the spotsizes and divergence of the laser beams before they are focused into the chamber, see TS in Fig. 3.3. This is mostly used to fine tune w_0 by controlling the collimated beam radius, see Eq. (3.1), and the exact position of the focus which is needed to overlap the focus of two beams.

The telescopes used are Galilean telescopes[88, Sec. 3.7], utilizing one focusing lens of focal length f_1 and one diverging lens of focal length f_2, placed a distance $f_1 - f_2$ apart. The beam radius is thereby reduced (increased) by a factor of $-f_2/f_1$ ($-f_1/f_2$) when the focusing (diverging) lens is placed first. Through Eq. (3.1) this is used to control the exact focused beam radius w_0 of the beams. One lens is placed on a manual translation stage, and the divergence of the outcoming beam can thereby be controlled. The divergence of a beam focused though a lens will change the distance from the lens to the beam waist, which is used to fine tune the position of the beam waist in the experiment.

[3] Note that w is commonly called the *spot size*, which I believe leads to a common misinterpretation of w being a diameter rather than a radius.

[4] Some sources call w_0 itself the beam waist.

3.4.7 Focused spot measurement

To measure the beam radius at the focus of the beams in the chamber, a beam profiler is used. A flip-mirror is inserted to catch the beam after the focusing lens and just before the vacuum chamber. The beam is focused onto the detector of a beam profiler (FemtoEasy Beampro LP6.3 UV). This profiler is sensitive in the wavelength range of 190 nm to 1100 nm, and can thereby be used for all the beams used for the experiments presented in this thesis.

In order to not damage the beam profiler with the focused beam, a stack of neutral density filters with total optical density $d = 11.5$ is used[5]. We have found that a maximum beam power of $p_{\text{avg}} = 20\,\text{mW}$ does not damage the detector when used with the $d = 11.5$ ND filter stack, even for the smallest focused beam radii of about $w_0 \approx 10\,\mu\text{m}$ that we achieve in the experiment.

A manual translation stage is used to control the exact position of the beam profiler. The profiler is translated back and forth along the laser propagation direction to find the exact focus of the beam. This position also provides a reference for focusing the two laser beams on the same spot, see Section 3.4.10.

The beam profiler is controlled by the FemtoEasy STAR software. This is set up to fit a 2D Gaussian distribution to the measured intensity profile, giving the $2w_0$ diameter ($1/e^2$) across the minor and major axis. Unless otherwise noted, the focused beam radii w_0 given in this thesis will be the mean of the major and minor $1/e^2$ radii, as the focus spots are all approximately round.

3.4.8 Characterizing pulse length

Pulse lengths are expressed by the FWHM (Full Width at Half Maximum) of the temporal profile of the laser pulse, which will be denoted τ_{FWHM}. In the lab, these are typically measured either by auto-correlation or cross-correlation.

Autocorrelation If possible, the most practical way to measure τ_{FWHM} we use in the lab is using a dedicated autocorrelator. The specific model we use is an APE PulseCheck 15 NIR, which can measure pulses in the wavelength range 700 nm to 1100 nm.

The autocorrector was used in the non-collinear mode, which means that the technique used is a background free intensity autocorrelation. For a thorough

[5]That is, the transmittance of the ND filter is $10^{-11.5}$.

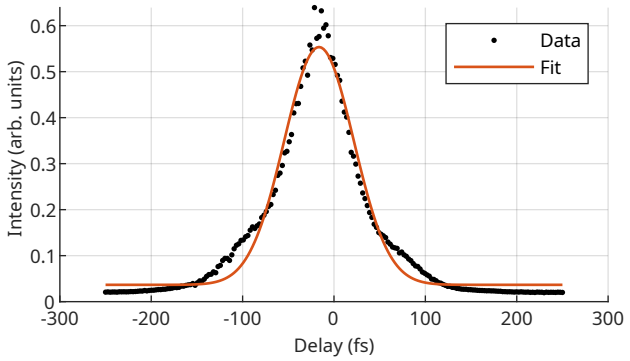

Figure 3.4: Background free intensity autocorrelation of the fundamental 800 nm pulse of the laser, after being transported to the vacuum chamber. Also shown is a Gaussian fit, which has the FWHM $\tau^{\mathrm{AC}}_{\mathrm{FWHM}} = 89.6\,\mathrm{fs}$, corresponding to a pulse length of $\tau_{\mathrm{FWHM}} = 63.4\,\mathrm{fs}$.

treatment of this measurement, see [58, Sec. 10.2.2]. The principle of the technique is that a laser beam is split in two by a beamsplitter, reflected back to the beamsplitter by two retroreflectors, in a geometry where the recombined beams are slightly noncollinear. By translating one of the retroreflectors, a delay is introduced between the split pulses. After recombination, the two beams are focused on the same spot on a non-linear crystal used for SHG, see Section 3.4.4. The created second-harmonic can be filtered spatially from the fundamental beams, which is why the technique is called "background free", and the intensity of this light is the autocorrelation signal.

An example of such a measurement is seen in Fig. 3.4. The autocorrelation intensity has the shape of the convolution of the pulse intensity profile with itself, and thereby, the relation between the temporal width of the autocorrelation intensity and the temporal width of the pulse depends on the pulse shape [58, Sec. 10.2.2]. For this measurement, we assume a Gaussian temporal pulse shape, and the FWHM of the (Gaussian) autocorrelation intensity $\tau^{\mathrm{AC}}_{\mathrm{FWHM}}$ is related to the FWHM of the pulse as $\tau_{\mathrm{FWHM}} = \tau^{\mathrm{AC}}_{\mathrm{FWHM}}/\sqrt{2}$. To find $\tau^{\mathrm{AC}}_{\mathrm{FWHM}}$ a Gaussian function is fitted to the autocorrelation intensity.

Crosscorrelation While the autocorrelation is both practical and accurate, it is technically limited because our model of the ABE pulseCheck only works for laser

wavelengths in the range 700 nm to 1100 nm. For laser pulses outside this range, we resort to an intensity crosscorrelation between the unknown laser pulse, and a laser pulse of known length.

As seen in Fig. 3.3, the optical setup used already provides collinear and overlapped laser beams, for which a delay can be introduced by controlling the delay stages. The cross correlation can be realized in two ways: By Sum Frequency Generation (SFG) in a non-linear crystal or by the non-linear ionization probability of molecules in the vacuum chamber.

For *SFG cross correlation*, the two overlapped beams are overlapped on a non-linear crystal, like a BBO crystal. Like explained in Section 3.4.4, when phase matching is achieved in the non-linear crystal, the two beams combine to produce a third beam with a frequency which is the sum of the two beam frequencies. For example, SFG light with a wavelength of 266 nm can be created from the 800 nm and 400 nm beams. The created beam can be separated from the incoming beams using a prism, and the intensity of the SFG light can be measured as a function of the delay between the two incoming pulses. The intensity profile of the produced light will be the convolution of the intensity profiles of the two pulses, and the pulse lengths will be related by,

$$\tau_{\mathrm{FWHM}}^{\mathrm{CC}} = \sqrt{(\tau_{\mathrm{FWHM}}^{1})^2 + (\tau_{\mathrm{FWHM}}^{2})^2}, \tag{3.2}$$

where $\tau_{\mathrm{FWHM}}^{\mathrm{CC}}$ is the FWHM of the cross correlation signal and τ_{FWHM}^{1} and τ_{FWHM}^{2} are the pulse lengths of the two pulses. Thereby, by measuring the intensity of the SFG beam as a function of the delay between known and unknown pulses, the length of the unknown pulse can be deduced.

Ion signal cross correlation. An alternative that is sometimes used in the lab is measuring the amount of ion signal of some molecules in the vacuum chamber as a function of the time delay between the two pulses. The non-linear multiphoton ionization process results in an amplified signal when the two pulses are temporally overlapped. It is therefore tempting to use ion signal as a function of pulse delay as the intensity cross correlation function. However, in the treatment of the autocorrelation and SFG cross correlation above, we utilized the fact that these are second-order non-linear processes, which means that the intensity profiles are the convolutions of the incoming pulses[98, Sec. 7.4.2]. The multiphoton ionization of an arbitrary molecule is, however, rarely a second-order non-linear process, and Eq. (3.2) does not apply. As the ionization process is of higher non-linear order than second, the cross correlation will be shorter than it should be for a second

order process. Thereby, if the ion signal is used as the cross correlation signal, the pulse length of the unknown pulse will be underestimated. The ion signal is, however, very useful for finding the temporal overlap between the two pulses, where the width of the signal does not matter.

3.4.9 Characterizing peak intensity

In the lab, we measure the *time-average beam power*, P_{avg}, because it is conveniently measured using a power meter. The laser field experienced by the species in the vacuum chamber is however better described by expressing the *peak intensity*, I_{peak}, for which the temporal and spatial profile of the laser pulse is taken into account.

Temporal profile The energy per pulse is given as $E_p = P_{\text{avg}}/f_{\text{rep}}$, where f_{rep} is the repetition rate of the laser. The pulse energy is distributed over the temporal pulse profile, and this profile is assumed to be Gaussian. Thereby, the power can be written as a function of time as

$$P(t) = \frac{E_p}{\sigma_t\sqrt{2\pi}} \exp\left(-\frac{(t-t_0)^2}{2\sigma_t^2}\right), \tag{3.3}$$

with the pulse length expressed in terms of the standard deviation σ_t. From this, it is easy to see that the power is maximized with the peak power $P_0 = P(t_0)$. When measuring the pulse length, the result is conventionally expressed as the FWHM, τ_{FWHM}, of Eq. (3.3). Half of the FWHM can be found by isolating t in the expression $P(t) = P_0/2$, giving

$$\tau_{\text{FWHM}} = 2\sqrt{2\ln(2)}\sigma_t. \tag{3.4}$$

The peak power can then be written as

$$P_0 = \frac{E_p}{\sigma_t\sqrt{2\pi}} = \frac{2\sqrt{\ln(2)}}{\sqrt{\pi}} \frac{E_p}{\tau_{\text{FWHM}}}. \tag{3.5}$$

Note that the constant $2\sqrt{\ln(2)}/\sqrt{\pi} \approx 0.94$ is sometimes omitted, but has been included in this thesis.

Spatial profile P_0 is distributed over the spatial intensity profile of the pulse. The spatial intensity profile is assumed to be a two-dimensional Gaussian function. For a constant beam power P, the spatial maximum of intensity, on the optical axis and at the beam focus, is given as $2P/\pi w_0^2$ [87]. Combining with Eq. (3.5), we find the peak intensity, at the spatial and temporal maximum, to be

$$I_0 = \frac{2\sqrt{\ln(2)}}{\sqrt{\pi}} \frac{2E_p}{\tau_{\mathrm{FWHM}} \pi w_0^2}. \tag{3.6}$$

3.4.10 Finding spatial and temporal overlap

In order to realize pump-probe experiments, it is of course critical that the pump and the probe laser pulses overlap spatially and temporally in the laser focus. The spatial overlap can be found independently of the temporal overlap, and is therefore practically found first.

Spatial overlap The spatial overlap is reached when the focus spot of the two pulses are focused on the same spot on whatever sample beam is used for the experiment, in the middle of the VMI spectrometer. The first beam is focused into the vacuum chamber. Here, the precise focus location is adjusted to give a symmetric distribution of ions from the VMI spectrometer, both in velocity and spatial focus.

The focus on the first beam is then sent to a beam profiler, as explained in Section 3.4.7, the beam profiler is adjusted to be in the exact focus plane of the beam, and the focus position is recorded. Thereby, the second beam can be sent onto the beam profiler, and the exact focus position can be adjusted to overlap with the first beam.

Temporal overlap The procedure for finding the temporal overlap is fundamentally only a question of ensuring that the effective optical path lengths of the two laser beams are equal. For ultrashort pulses, however, a change in path length of 30 µm, corresponding to a delay of 100 fs, could ruin the overlap. Therefore, multiple steps are taken to narrow in on the temporal overlap.

First, both laser pulses are sent onto a photodiode, and measured by an oscilloscope, whereby both pulses become visible. This measurement is however limited

by the rise time of the photodiode, and the overlap of the two pulses can be found with an uncertainty of about a nanosecond.

The next level of accuracy in the temporal overlap is doing an SFG intensity cross-correlation, like explained in Section 3.4.8. The cross-correlation signal will be maximized when the two pulses are temporally overlapped. Dispersive elements, like lenses, windows and air, between the placement of the BBO crystal and the actual focus in the laser chamber can, however, offset the found overlap from the true overlap by some picoseconds. Care has to be taken when two beams of equal wavelengths are used, as interference effects happen on length scales finer than the accuracy of the stage, making it much harder to find the cross correlation maximum.

The final level of temporal overlap is looking at the non-linear ion signal cross correlation in the vacuum chamber. As explained in Section 3.4.8, the maximum of the ion signal corresponds to the temporal overlap. For some specific wavelengths, molecular excitations can greatly aid in finding the temporal overlap. For instance, if the case of a 400 nm pulse coming before an 800 nm pulse, the water signal is enhanced compared to the reverse pulse order, even for hundreds of picoseconds of delay between the two pulses. Finding this signal is much easier than finding the direct time overlap between the two pulses, as it is three orders of magnitude longer in time.

3.5 Velocity map imaging (VMI)

We want to measure the mass and initial velocity of the ions created by the laser-pulses in the vacuum chamber, which is achieved with Velocity Map Imaging (VMI). The principle of VMI is to project ions onto a detector screen, so that the initial v_x and v_y velocity of ions are transformed into spatial positions x and y on the detector. This is achieved using ion optics, in a configuration first realized by Eppink and Parker [35], building on the original ion imaging idea of Houston and Chandler [25]. When *velocity focus* is achieved, the initial spatial position of the ions have minimal influence on their final detector locations x and y. Furthermore, the time of flight (TOF) of the ions between ionization and hitting the detector encodes the mass-to-charge ratio (m/q) of the ions.

Fig. 3.5 shows the electrodes in this setup and their dimensions, as well as the equipotential lines illustrating the bend electric field that realizes the ion optics. The three VMI electrodes are the repeller (R), extractor (E) and ground (G) plates.

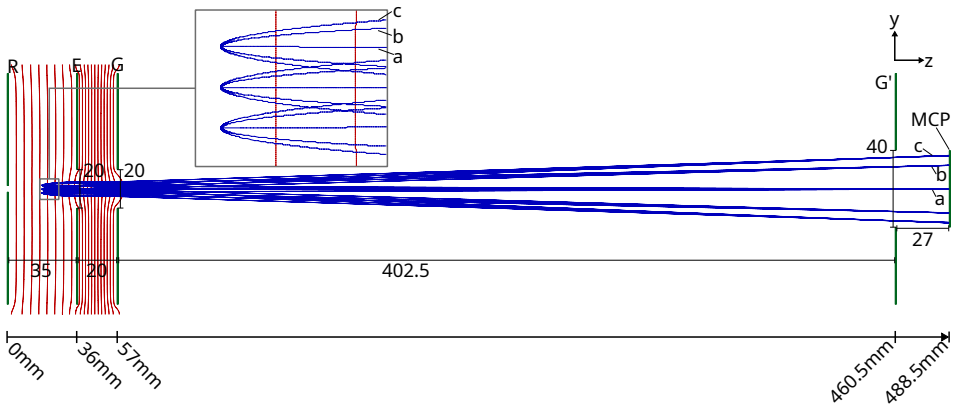

Figure 3.5: Schematic and simulation of the VMI spectrometer, showing a slice through the cylindrically symmetric setup. The electrodes are shown in green, equipotential lines shown in red. The ion trajectories for ions with 3 different velocities, a, b and c, and their opposites, as well as 3 different starting positions are shown in blue. The inset shows a zoom in of the first part of the ion trajectories. The most important distances are marked, with all lengths given in millimeters, note that each electrode has a thickness of 1 mm. The bottom axis shows the distance from the left of the setup to the left size of each electrode.

Optimizing for VMI focus, these plates are typically operated at $V_R = 6000\,\mathrm{V}$, $V_E \approx 3800\,\mathrm{V}$ and $V_G = 0\,\mathrm{V}$. Meanwhile, towards the end of the ion trajectories are a second ground plate (G'), and finally the MCP detector surface.

Fig. 3.5 also shows ion trajectories simulated with SIMION 8.0.4. The ions were given three different kinetic energies (0 eV, 2 eV, 4 eV) in both positive and negative y direction, making for 5 different initial velocities. This was repeated for 3 different positions (-2 mm, 0 mm, 2 mm relative to the center between the repeller and extractor plates). It can be seen that the ion trajectories converge to the same detector positions according to their velocities, while the effect of the different initial positions vanish.

3.5.1 VMI calibration

As explained above, the VMI spectrometer encodes the mass of the recorded ions as the TOF, and the initial v_x and v_y velocity components in the x and y spatial positions on the detector. Thereby, we need to find the calibration factors to retrieve these wanted values.

The square of the TOF should be proportional to the mass-over-charge ratio m/q, and the square of the radius of the hit position on the detector, r_d^2, should be proportional to the kinetic energy associated with the initial velocity components parallel to the detector plane $E_{kin}^{||}$ [35] [6]. To test if this holds for our specific VMI spectrometer, a simulation was made using SIMION 8.0.1. In this simulation, 2000 ions were created with charge 1 e, a random mass in the range 1 u to 200 u, a random direction, and a kinetic energy in the range 0 eV to 6 eV. The ions were created in random positions inside a cylindrical volume with a radius of 40 µm and a length of 1 mm, centered in the center between the repeller and extractor VMI electrodes, a typical ionization volume used in experiments. Each ion trajectory was simulated individually. The simulation was done with 10 grid units per mm. The results of this simulation is shown in Fig. 3.6, and these results will be analyzed to find the calibration factors below.

TOF to mass-over-charge calibration As shown in Fig. 3.6(a_1), the m/q ratio does indeed seem to be proportional to the square of the TOF. This is described by the equation,

$$m/q(TOF) = a_{\mathrm{TOF}} \cdot TOF^2 + c_{\mathrm{TOF}}, \tag{3.7}$$

where a_{TOF} and c_{TOF} are the calibration factors we are looking for. Fig. 3.6(a_1) shows the fit of Eq. (3.7) to the data, and Fig. 3.6(a_2) shows the residuals between the fit and the data points. The residuals show no significant systematic deviations, and the linear relation between m/q and TOF^2 is thereby confirmed. It is, however, seen that the size of the residuals are dependent on TOF^2, that is, the m/q uncertainty rises the larger the m/q.

In experiments, the calibration factors a_{TOF} and c_{TOF} are determined based on two (TOF, m/q) points. To do this, two peaks have to be identified in the TOF spectrum, for instance the ever-present H_2O^+ peak and the peak of whatever alkali is used in the experiment. These two points give a calibration good enough to identify the m/q ratio of the rest of the peaks in the TOF spectrum. If higher precision is needed, a fit to more peaks can be used, however, that has never been relevant for the work presented in this thesis.

[6] Note that VMI is limited in the fact that it only measure the projection of the ion velocities, Section 4.3 discusses how symmetry in the experiment can be exploited to reconstruct the full 3D velocity distribution.

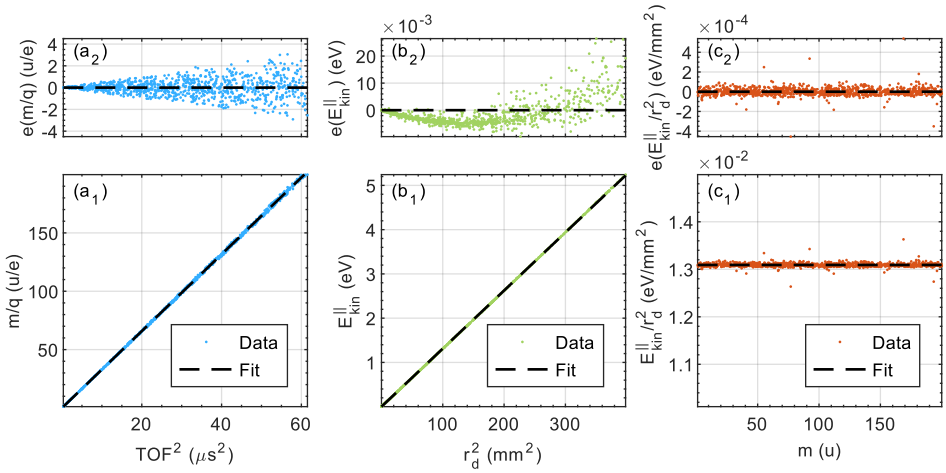

Figure 3.6: Data from a SIMION simulation of the VMI spectrometer shown in Fig. 3.5, where 2000 ions were created with random masses and initial kinetic energies, and flown until they hit the detector plane. (a_1) shows m/q ratio of the ions against the square of their TOF in blue dots. Also shown is the least squares linear fit to Eq. (3.7) in black dashed lines. (a_2) shows the residuals of this fit, $e(m/q)$. (b_1) shows the initial kinetic energy associated with the velocity components parallel with the detector plane $E_{kin}^{||}$ against the square of the radius of the hit on the detector r_d in green dots, and a least-squares linear fit of Eq. (3.8) to the data in the black dashed line. (b_2) shows the residuals between this fit and the data, $e(E_{kin}^{||})$. (c_1 - c_2) shows that the ratio between $E_{kin}^{||}$ and r_d^2 is independent of the mass of the ion.

Detector radius to kinetic energy calibration As shown in Fig. 3.6(b_1), the simulation shows that $E_{kin}^{||}$ is proportional to r_d^2. The figure also shows a fitted curve, which was fitted with function

$$E_{kin}^{||}(r_d) = k_{\mathrm{VMI}} \cdot r_d^2, \tag{3.8}$$

where k_{VMI} is the energy calibration factor. Note that only one calibration factor is needed, as $r_d = 0$ is assumed to imply that $E_{kin}^{||} = 0$. The residuals of the data from this fit, shown in Fig. 3.6(b_2) show systematic deviations, which stem from aberrations in the ion optics. These deviations are, however, very small.

In a real experiment, k_{VMI} can be calculated based on the known energy of a single peak in the r_d distribution. In this thesis, this is often done using the well known energy of alkali ions coming from the Coulomb explosion of alkali dimers.

Fig. 3.6(c_1-c_2) shows that the calibration factor $k = E_{kin}^{||}/r_d^2$ is independent of the mass of the relevant ion, which is especially important for the work in this thesis where the kinetic energies of many different ions are recorded simultaneously.

From the above, we can easily find the calibration factor from x or y detector coordinate to v_x or v_y ion velocities as

$$v_x = \frac{2k_{\mathrm{VMI}}}{m}x, \qquad v_y = \frac{2k_{\mathrm{VMI}}}{m}y, \tag{3.9}$$

where m is the mass of the ion in question.

3.5.2 Optimizing VMI focus

The extractor voltage V_E needs to be fine-tuned to optimize the VMI focus. The unidirectional effusive beam described in Section 3.3.3 leads to a narrow line of signal in the VMI image, as the v_y is near zero for these ions. Thereby, the VMI focus is optimized by fine-tuning V_E, so that the effusive signal line is as narrow as possible. Typically, a width of the centroided ion hits, see Section 4.1, of less than 1 detector pixel is achieved. This is done at the start of each day, as the optimal V_E seems to fluctuate a few tens of Volts ($\Delta V_E/V_E \approx 0.5\%$). This could be because the laser focus ends up in slightly different vertical positions from day to day.

3.5.3 VMI of doped droplet beams

The velocities of ions originating from helium droplets will have two components: The velocity relative to the droplet and the velocity of the droplet itself. As discussed in Section 3.2, all droplets in the beam have approximately the same velocity, which is determined by the expansion conditions and is typically in the range $200\,\mathrm{m\,s^{-1}}$ to $400\,\mathrm{m\,s^{-1}}$. In the geometry of the setup, this velocity vector lies in a plane parallel with the detector. Thereby, what we see on the detector is simply the distribution of ion velocities relative to the droplet, shifted by the droplet speed. Note that while the detector position is proportional to the ion velocity, the calibration factor between the two depends on the ion mass. Thereby, the offset in detector position is different for each ion species. Once the offset has been subtracted from the data however, the energy calibration factor k_{VMI} is the same for all masses of ions.

3.6 Ion detection

The role of the ion detector is to amplify the signal of the ions hitting the detector plane, and converting this signal into light that can be detected by the TPX3Cam. The detection system consists of two microchannel plates (MCPs - El Mul Technologies B050V) and a P47 phosphor screen.

Each of the MCPs is packed with pores going through it, each having a diameter of approximately 10 µm, and spaced by approximately 15 µm in a hexagonal pattern, giving an open area ratio (OAR) of approximately 60%. Each channel is tilted with respect to the surface normal of the plate by approximately 8°. The two plates are stacked in such a way that the tilt of their channels are opposite to each other, which is called a chevron configuration.

A positive potential difference of 1800 V is applied from the front to the back of the MCP stack. When an ion hits inside a channel of the first MCP, electrons are released and are accelerated by the potential difference. Due to the tilt of the channel, the released electrons once again hit the channel wall, which releases even more electrons, and this process continues multiple times. The electron cascade hit the second MCP plate, and the amplification continues. Due to this process being physically confined in the channels of the MCP, the spatial position of the ion hits on the front MCP are reflected by the spatial position of the electrons released from the back MCP.

The electron avalanche from the back MCP hit a P47 phosphor screen that is biased to a voltage 3000 V higher than the MCP stack backside, which further accelerates the electrons. Thereby, the electrons excite the phosphor screen in a local spot, which relaxes by emitting photons in a fluorescent transition. P47 is used specifically because the response and decay of this fluorescent emission is the fastest among all commonly used phosphors. The photons emitted are detected by the TPX3Cam detector.

One thing to note is that the detection efficiency of this setup is geometrically limited by the fact that ions have to hit inside an MCP channel to be detected. This limits the detection efficiency of the system to a maximum of 60%, the OAR. One solution to this problem is a so called funnel-type MCP, where the openings of each MCP channel has an opening like a funnel. In this design, OARs of above 90% can be achieved [37, 47], increasing the maximum ion detection efficiency. Such an MCP was implemented in the setup after the experiments presented in this thesis were performed.

3.7 TPX3Cam

As described in Section 3.6, the ions projected onto the detector by the VMI spectrometer leads to spots of light on the phosphor screen. The phosphor screen is imaged onto the detector chip of the TPX3Cam event-based pixel detector [6, 23, 38, 85].

The detector chip consists of a front layer of silicon, bump bonded to a Timepix3 chip [6, 85]. When photons hit the silicon, electron hole pairs are generated charging the pixels of the Timepix3 chip. Each pixel works as a constant discriminator with a programmable threshold. When the voltage of a pixel crosses this threshold, the time of the crossing (Time of Arrival, TOA) and the Time over Threshold (TOT) is recorded, along with the x and y pixel coordinates. This is referred to as a pixel event [85]. There are 256x256 square pixels on the chip, with side length 55 µm. The TOA is measured relative to a triggering pulse, which in our setup is provided by the laser system. The TOA is thereby measured relative to the laser pulse hitting the center of the VMI spectrometer, with some constant offset due to light propagation and electrical signal propagation. The resolution of the TOA measurement is 1.56 ns and the resolution of the TOT measurement is 25 ns. The Timepix3 chip is read out by a SPIDR chip [115] that collects the pixel events and allows for their transmission to a computer.

On the computer side, the data acquisition is handled by the "pymepix" program [1][7]. This is controlled in a graphical user interface, which is a heavily modified version of the "pymepixviewer" package. The "pymepixviewer" has been extended to enable scanning over stages, like the Newport delay stage described in Section 3.4.3, and the Lake Shore temperature controller described in Section 3.2.

The raw data output saved from the TPX3Cam is a list of pixel events, where the following coordinates are recorded: The laser trigger index, the x and y pixel coordinates, the TOA and the TOT.

[7] See also this reference for an exact specification of the data format.

CHAPTER 4

Analysis Techniques and Programs

This chapter will give a brief overview of some analysis techniques that are used for all of the experiments presented in this thesis.

4.1 Clustering and centroiding

As described in Section 3.7, the TPX3Cam detector records a collection of coordinates for each pixel lighting up. Each ion hit on the MCP leads to a number of pixels lighting up, and thereby we need to analyze the raw TPX3Cam pixel event to retrieve the coordinates of the ion hits. Firstly, all the pixel events are grouped together according to their proximity in the x, y and TOA coordinates which is referred to as *clustering*. Secondly, the center-of-"mass" of each pixel cluster is calculated, using the TOT coordinate as the weighting, which is referred to as *centroiding*.

4.1.1 Clustering

The specific algorithm used for this is the DBSCAN (Density-Based Spatial Clustering of Applications with Noise) algorithm [36]. This algorithm is used because it calculates the number of clusters in each laser shot a priori, which is important

because we do not know this number in advance. Furthermore, it is tolerant of noise in the dataset.

The specific implementation of the algorithm has been written in C++ by Laurits L. Sørensen and Simon Fischer-Nielsen, and the source code is publicly available on their GitHub page[1]. I want to thank these two authors for providing this implementation. Previously, the implementation included in the SciKit-learn Python library was used, however, this code ran too slowly, warranting the change to the custom implementation. In the custom implementation, the time-walk correction of the pixel events is applied before the centroiding, see Section 4.2 for further details.

The result of the clustering is that each pixel event is given an index that identifies which cluster, that is which ion hit, that it is a part of. During a typical experiment, each ion hit lights up an average of $\sim$7 pixels on the TPX3Cam detector.

4.1.2 Centroiding

Each cluster identified by the clustering algorithm is assumed to correspond to one ion hit. Thereby, the center of the ion hit position in x, y and TOA coordinates can be found as a weighted mean using the TOT coordinate as the weight,

$$x = \frac{\sum_{i=1}^{n} x_i \cdot \mathrm{TOT}_i}{\sum_{i=1}^{n} \cdot \mathrm{TOT}_i}, \quad y = \frac{\sum_{i=1}^{n} y_i \cdot \mathrm{TOT}_i}{\sum_{i=1}^{n} \cdot \mathrm{TOT}_i}, \quad \mathrm{TOA} = \frac{\sum_{i=1}^{n} \mathrm{TOA}_i \cdot \mathrm{TOT}_i}{\sum_{i=1}^{n} \cdot \mathrm{TOT}_i}, \tag{4.1}$$

where the sums are over the pixel events in the cluster. The TOT is used as the weight because it represents how strongly the pixel was lit up. This is referred to as finding the centroid of each cluster. In principle, the x and y coordinates are found with better resolution than the pixel resolution of the TPX3Cam, and similarly for the TOA resolution [23].

4.2 Timewalk corrections

The TPX3Cam camera gives Time of Arrival (TOA) of each pixel lighting up, measured with respect to the trigger pulse from the laser. This is used in the experiment to quantify the Time of Flight (TOF) of the ions created by the laser pulses. However, due to the response time of the detection electronics in the

[1] `https://github.com/laulonskov98/pixel_centroiding_DBSCAN`

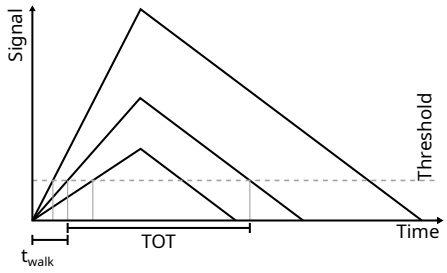

Figure 4.1: Illustration of how the signal (voltage) in a single TPX3Cam pixel evolves in time after it has been hit by light of three different intensities, as represented by the three lines. Also shown is the magnitude of the time-walk t_{walk} and the Time Over Threshold TOT for the middle intensity.

TPX3Cam, the TOA is subject to an effect called *time-walk*, which gives an uncertainty in the TOF. This effect can, however, be corrected for, which is the subject of this section.

The time-walk effect is illustrated in Fig. 4.1. One approximation of the response of a TPX3Cam pixel to the exposure of light is that the signal of the pixel rises during a constant time, and falls off at a constant rate. Thereby, the time delay between when the light hits the pixel and when the signal crosses the detection threshold must become smaller when the signal is larger, and this time delay is referred to as the time-walk t_{walk}. Secondly, the time period for which the signal is over the detection (TOT) must get larger when the signal gets larger. This model does not perfectly capture the response of a TPX3Cam pixel to a light pulse, but it does motivate the fact that there is a correlation between t_{walk} and TOT.

This correlation is shown for an experimental data set in Fig. 4.2(a), where it is clearly seen that the average TOA of the pixel events has a dependence on the events TOT value. To correct for this dependence, the average TOA is calculated for 200 TOT bins along the TOT axis, yielding the red curve shown in Fig. 4.2(a). This curve is shifted on the TOA axis so that the minimum TOA of the correction curve becomes 0. The timewalk correction curve $t_{\text{walk}}(\text{TOT})$ is created as a linear interpolation between these points. For each pixel, the TOA value is corrected by subtracting $t_{\text{walk}}(\text{TOT})$,

$$\text{TOA}_{\text{cor}} = \text{TOA}_{\text{raw}} - t_{\text{walk}}(\text{TOT}). \tag{4.2}$$

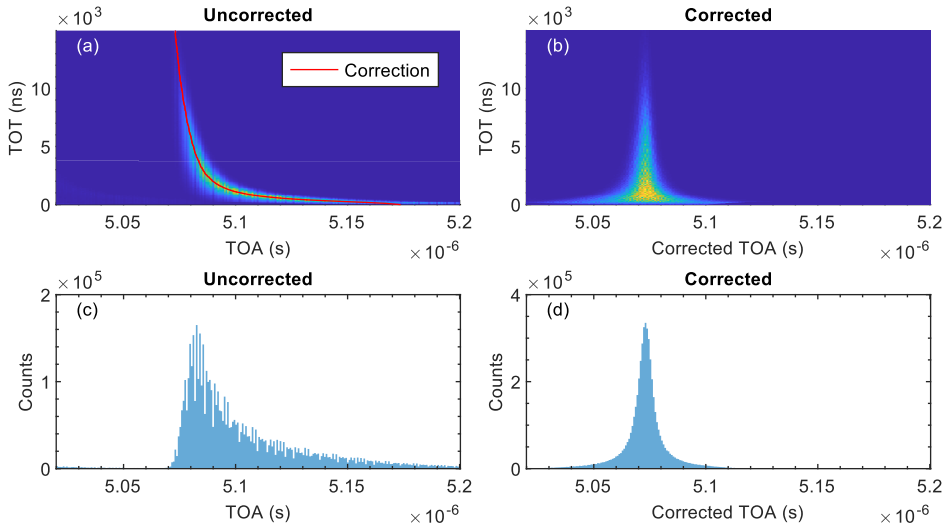

Figure 4.2: Illustration of the time-walk correction for TPX3Cam pixel data applied before clustering and centroiding. (a) 2D histogram of showing the correlation between TOA and TOT. Also shown is the found time-walk correction curve. (b) TOT-TOA 2D histogram of the data, after the time-walk correction has been applied. (c) 1D TOA histogram of the uncorrected data. (d) 1D TOA histogram of the time-walk corrected data. The data in the shown TOA range corresponds to H_2O^+ ions in all panels, which were created by strong field laser ionization in the center of a VMI spectrometer set to velocity-focus.

The result is seen in Fig. 4.2(b), showing that after the correction, there is no correlation between the average TOA and TOT. Comparing Fig. 4.2(c) and (d), we see that the TOA resolution is markedly improved by the time-walk correction, and that the asymmetry of the peak is removed after the correction.

Post-centroiding time-walk correction As described in Section 4.1, the time-walk correction is applied to the pixel data before the clustering and centroiding algorithm turns the pixel data into ion hit data. As such, one would expect that the ion hit data should show no correlation between TOT and TOA. However, looking at Fig. 4.3(a), this is not the case, and the ion hit data shows a very similar TOT dependence as the one described above. The reason for this is so far unknown, however, guided by the clear trend shown in Fig. 4.3(a) a second time-walk correction is applied to the ion hit data, once again improving the TOA

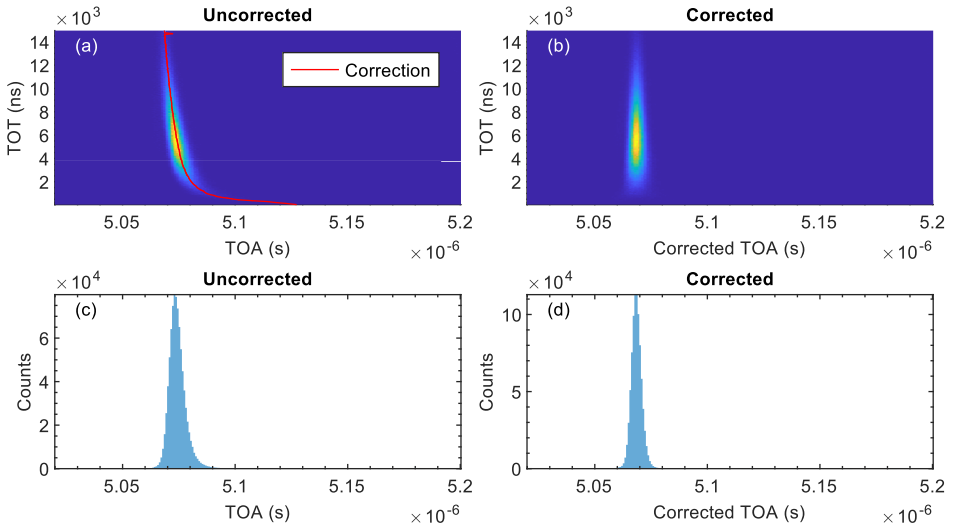

Figure 4.3: Illustration of the time-walk correction clustered and centroided ion hit data. (a) 2D histogram of showing the correlation between TOA and TOT. Also shown is the found time-walk correction curve. (b) TOT-TOA 2D histogram of the data, after the time-walk correction has been applied. (c) 1D TOA histogram of the uncorrected data. (d) 1D TOA histogram of the time-walk corrected data. The data shown is the same as that shown in Fig. 4.2 except that it has been pre-centroiding time-walk corrected, clustered and centroided.

resolution. This provides the final corrected TOA of each detected ion hit, which is the best estimate available for the Time of Flight (TOF) of the ions, and will be referred to as such for the rest of this thesis.

4.3 Image reconstruction

As explained in Fig. 3.6, the VMI spectrometer maps the v_x and v_y components of the initial ion velocities onto x and y positions on the detector screen. Thereby, the v_z component of the initial velocity is lost. This is a problem when we want to measure the kinetic energy of the ions, where the full magnitude of the initial velocity vector is needed. However, when ionizing particles with a linearly polarized laser pulse, a cylindrical symmetry around the laser polarization direction is ensured in the ion velocity distribution. When this axis of symmetry lies in

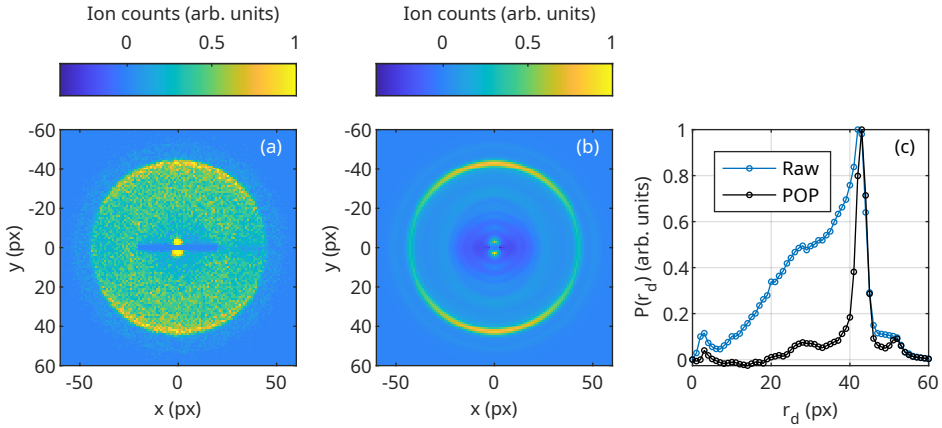

Figure 4.4: (a) VMI image of coincidence filtered data from the Coulomb explosion of K_2 dimers. (b) The result of the POP algorithm shown as an image. (c) Comparison of radial detector coordinate distribution $P(r_d)$ for the data shown in (a) and (b).

the detector plane, the full 3D velocity distribution can be reconstructed from the 2D projection on the detector[2]. Mathematically, this is referred to as an inverse Abel transformation. The numerical methods used to do this in practice are not pure inverse Abel transformations, but are often referred to as "Abel inversions" or "image reconstructions". Reference [116, chap. 3] provides a textbook overview of some of these methods, but many new methods have been implemented since it was written.

4.3.1 Polar onion peeling

Polar Onion Peeling (POP) is a method of reconstructing the full velocity distribution from VMI images. The specific implementation used in this thesis is made by Abi Natan [82], and is based on reference [96]. The method is based on the fact that the projection of the initial velocities onto the detector only smears the velocity distributions towards the middle of the detector, and assumes that no part of the distribution exists outside the detector. The radial bins at the very outside edge

[2]No new information is magically constructed in this process, the cylindrical symmetric velocity distribution only has 2 degrees of freedom, and its projection is recorded in 2 degrees of freedom on the detector.

of the detector are thereby unaffected by the projection. The effect of whatever signal found in these bins can be subtracted from the rest of the image, whereby the next radial bin in the subtracted image is also free from outside influence. This continues iteratively until the center of the detector is reached, like peeling off the layers of an onion.

Fig. 4.4 shows the effect of the POP algorithm. The data in the figure was recorded by doping helium droplets with K_2 dimers and Coulomb exploding these using multiphoton ionization with a femtosecond laser pulse. The data was filtered, keeping those ions identified as originating from the $^{39}K_2$ dimers using the coincidence filter described in Section 8.4.3. Fig. 4.4(a) shows the VMI image, where the effect of the projection is clear. Fig. 4.4(b) shows how this projection is undone by the POP algorithm. Fig. 4.4(c) compares the r_d distribution, where r_d is proportional to initial ion speed. Thereby, the ion speed and kinetic energy distributions can be found.

CHAPTER 5

Solvation Dynamics of Alkali Ions in Helium Droplets

In this chapter, I will present the results of a novel experimental technique that has enabled us to study the solvation dynamics of alkali ions in helium droplets, atom-by-atom and on the femtosecond timescale. To my knowledge it is the first experiment where the solvation dynamics are measured for an isolated ion going from gas phase to solvated phase. As such, this work provides a direct insight into the microscopic origin of solvation, a physical process that is omnipresent in chemistry, biology and our daily lives.

The experimental results for sodium solvation covered in this chapter has been published in reference [2]. The work, especially the data analysis, has however been extended in ways that will be mentioned in the chapter when relevant. Furthermore, unpublished results for the solvation of lithium and potassium ions are presented.

5.1 Background

5.1.1 Macroscopic solvation

Macroscopically, solvation is the concept of a solute being stabilized by a solvent. Often, the solute is dissolved into its constituent parts. For example, when salt is put in water, the NaCl crystals breaks up into Na^+ and Cl^- ions, which are in turn

surrounded by water molecules. The term solvation is also used to describe the process of going from an unsolvated to a solvated state.

The thermodynamics of this process are very well understood, that is, the amount of energy released in the solvation process, how much solute can be solvated in a certain amount of solvent, how this depends on temperature and so on [76, 93]. However, these properties have mostly been studied in the macroscopic steady states, that is before and after the solvation process.

In contrast to this, the work of this chapter focuses on the process of solvation itself, for a microscopic system of a single ion getting solvated in liquid helium in the form of a nanodroplet.

5.1.2 Solvation in helium droplets

In Section 2.5, it was discussed how some dopant species have equilibrium positions inside helium droplets, while others have equilibrium positions on the surface. The inside bound species are stabilized by being immersed in the liquid helium and are thereby solvated. Their attraction to the helium atoms leads to the formation of shells of higher-than-bulk density helium, called solvation shells. The structure of these shells are predicted by DFT calculations [16]. The shells appear to co-rotate with the molecules leading to an increase in the molecules effective moment of inertia and centrifugal distortion parameter, compared to gas phase. This has been explored by different types of rotational spectroscopy [27, 28, 45, 49, 65].

Ion solvation has also been studied in helium droplets. For ions the solvation shells are especially well localized and solid-like, for which reason an ion solvation complex (X^+He_N) is often called a "snowball" [43]. These have been studied by mass spectrometry experiments, where the number of helium atoms N can be measured after the snowballs have been ejected from the droplets. This has been achieved by electron impact ionization of alkali-doped helium droplets, indicating many preferred structures like the closed solvation shells and more [8, 92]. This technique has also been applied to singly [18] and doubly [121] charged Ca ions. The preferred structures are found to be predicted by the evaporation energies[1], defined as $E_{\text{evap}}(N) = E(\text{Ak}^+\text{He}_N) - E(\text{Ak}^+\text{He}_{N-1})$ [43]. The evaporation energies are important to the understanding of solvation because they essentially tell how much an extra helium atom adds to the complex in terms of stability. Similar

[1] Sometimes called the "dissociation energies", but in this thesis, I have chosen the more specific "evaporation energy" term.

studies have also been done using multiphoton ionization of the alkalis [81], with similar results.

One limitation of previous ion solvation studies in helium droplets is the lack of time resolution. Electron impact ionization provides no time resolution, and even if it did, realizing a time-resolved experiment requires both a way to start solvation and a way to measure the state of solvation at a given time.

5.1.3 Previous solvation dynamics studies

To my knowledge, no previous experiments have measured the solvation dynamics of a bare ion introduced into a liquid. In 2015, it was even speculated that such an experiment would be impossible in the textbook entitled "Ions in Solution and Their Solvation" by Y. Markus [76, p. 107]. However, solvation dynamics of solvated molecules after a state change have been studied experimentally with pico- or femto-second time resolution, and this subsection will give a brief overview of some of these studies.

One important aspect of solvation is how the solvent adapts to a change in the solute. Specific solute changes lend themselves well to different measurement techniques. For example, some molecules can be electronically excited to induce a change in their dipole moments. In a dipolar solvent, like water, this will cause the solvent to rearrange, which will again influence the electronic structure of the molecule. If the excited state can decay by fluorescence, then the wavelength of the emitted fluorescence will change as the solvent rearranges. Typically, the fluorescence undergoes a redshift because the excited state is stabilized by the solvent and because the molecule vibrationally relaxes. This solvent rearrangement has been measured with time-resolved ultrafast, ultraviolet fluorescence spectroscopy [54]. The time resolution was achieved in a pump-probe scheme, where a pump laser pulse excites the molecule, and the resulting fluorescence is measured with time-resolution, by sum-frequency-generation with a probe laser pulse [56]. It was found that the solvent dynamics were well described by a bi-exponential decay with lifetimes $\tau_1 = 0.16\,\text{ps}$ and $\tau_2 = 1.2\,\text{ps}$. This tells us that water as a solvent can rearrange on a timescale of picoseconds to accommodate a change in the solute.

Another important aspect of solvation dynamics is how quickly the solvent can cool internal energy, like vibrational excitation, of the solute. This has been measured by transient-absorption spectroscopy for e.g. dipeptides in water [111]. Here, the molecules were excited by a femtosecond 200 nm pump pulse, and probed by a femtosecond IR pulse. By this, the study was able to follow the dissipation

of energy from individual vibrational modes of the molecule. The study found that the combined internal conversion of electronic-to-vibrational energy and the dissipation of this vibrational energy to the solvent happens in less than 2 ps. This is relevant to this thesis, as the experiment in this chapter essentially measures how quickly the bond energy of the alkali-ion-helium complex Ak^+He_N can be dissipated to the helium solvent.

Finally, different solvation dynamics of excited atoms and molecules on rare gas clusters have been studied previously [22]. In one study [77], single barium (Ba) atoms were doped onto argon (Ar) clusters, and the effect that the solvent Ar has on the solute Ba was measured by photoelectron spectroscopy (PES). To measure dynamics, the experiment photoexcited the Ba atom with a pump pulse and later photoionized the excited Ba^* atom with a probe pulse. One component of the change in the PES spectrum was found to be the partial solvation dynamics of the excited Ba* atom on the Ar clusters. This work has also been extended to the solvation dynamics of a rydberg-excited molecule (DABCO) on argon clusters [14], where the dynamics of moving between different solvation sites were measured.

5.1.4 TDDFT studies of ion solvation in helium droplets

Density Functional Theory (DFT) is most commonly used to model the *electron density* in the various orbitals in a molecule. However, it can also be used to model helium droplets by modelling the *helium density* in the droplet. By using specifically formulated functionals, the superfluid characteristics of the helium droplets can be captured in these simulations [17]. As mentioned in Section 2.5, the location of dopants in the droplets have also been studied by DFT [10], where it was found that neutral alkali atoms reside on the surface, weakly bound by $\sim$1 meV, while alkali cations will be solvated in the droplet, like most other closed shell systems.

The time dynamics of different helium droplet systems can also be studied in this way, by extending to Time-Dependent DFT (TDDFT). This has been used to simulate the solvation dynamics of alkali and alkaline earth cations starting from the surface position of their neutral precursors [2, 40, 70].

An example of such a simulation can be seen in Fig. 5.1. The initial configuration at $t = 0$ ps has been found by DFT as the minimum energy configuration of a neutral Na atom on the surface of a droplet containing 2000 helium atoms. This neutral atom is replaced by its corresponding Na^+ ion, and time is evolved by TDDFT. This simulation is crucial to the interpretation of the experiments that will

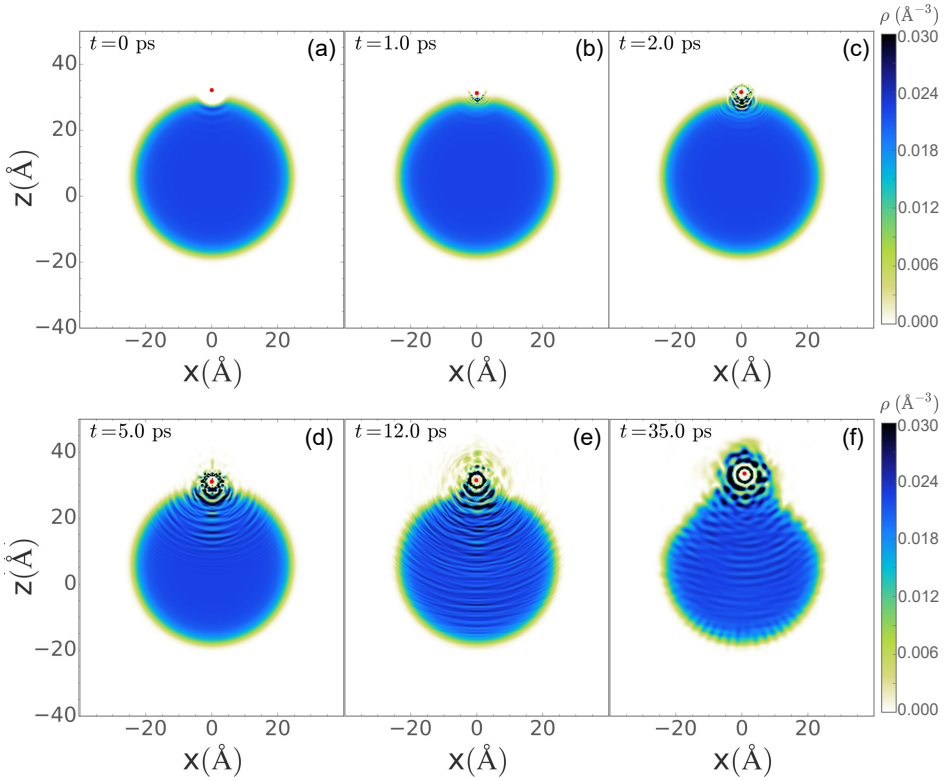

Figure 5.1: Snapshot of a TDDFT simulation of the solvation of a Na^+ ion (red dot) in a helium droplet consisting of 2000 ^{4}He atoms, showing a slice through the helium density for 6 different time steps. The initial $t = 0$ ps is that of the neutral Na atom in equilibrium on the droplet. See supplementary information of [2] for a video of the full time evolution. Simulation done by Martí Pi and Manuel Barranco, figure adapted from [2].

be presented in this chapter, because it gives an intuition of what happens on the droplet surface. We see that the Na^+ ion mostly stays in its starting position for the first tens of ps. In this time, helium rushes towards the Na^+ ion, see Fig. 5.1(a-c), building up in the first solvation shell, see Fig. 5.1(b-d), and later builds up a second solvation shell, see Fig. 5.1(e-f). It is also seen how density waves move through the droplet, hinting that it is able to quickly dissipate energy away from the site of the Na^+He_N complex. The simulation also extends to later times, which is shown in the supplementary information of reference [2], where it is seen that the Na^+ ion will eventually move inside the droplet after several hundred picoseconds.

To quantify the simulated solvation in a way that can be compared to the experiments in this chapter, it is analyzed how quickly the first and second solvation shells build up. The density of helium within the solvation shells can be integrated to find the number of atoms within the shell. From this, it is found that the first 5 helium atoms move within the first solvation shell at a rate of about 1.4 He/ps, while they move within the volume covered by the first and second solvation shell at a rate of 3.1 He/ps.

These simulations have been extended to other alkali ions [40]. This paper only treats the attachment rate in the first solvation shell, where it was found that the helium atoms attach to Li^+ ions at a rate of 1.5 He/ps, Na^+ ions at 0.8 He/ps, and K^+ ions at 0.6 He/ps. The found rate for Na^+ are different from what was found for reference [2]. The authors of reference [40] have told me that this is due to the newer paper utilizing a more accurate simulation, with an improved Na^+–He pair potential and a finer spatial sampling of the helium density.

The final quantity that would be interesting to extract from the TDDFT calculation is the energy in the formed Ak^+He_N complexes, and how quickly this energy is dissipated to the droplet. However, this is not possible, as the DFT approach gives no distinction between the helium that is in the complex and the helium in the bulk droplet.

All in all, the TDDFT calculations are very valuable as they give insight into what happens in the droplet in the solvation experiment, and provide an overall timescale of how quickly the ion solvation happens.

5.1.5 Time dynamics of alkali-exciplex formation on helium droplets

The time dynamics of the formation of alkali-helium exciplexes, that is electronically excited alkali atoms bound to helium atoms, have been studied previously in the case of K^*He_n and Rb^*He_n complexes [33, 103]. While we were not aware

of these previous experiments until after we had finished the first iteration of the solvation experiment, the experimental scheme turns out to be quite similar.

A single alkali (Ak) atom is doped onto an otherwise pure helium droplet, and is electronically excited by a femtosecond laser pulse. The excited Ak atom attracts helium atoms that bind in a complex Ak^*He_N. A second laser pulse ionizes the Ak atom, and thereby creates an Ak^+He_N complex on the droplet. This ionic complex is thought to desorb from the droplet surface, and after this desorption, it is detected using time of flight mass spectrometry.

The formation time of the K^*He_1 exciplex was measured to be $\sim$200 fs, and the formation time of the K^*He_2 exciplex was estimated to be the same [103]. In the case of Rb^*He_1 the formation time was found to be significantly longer, at 8.5 ps. The study of the formation of the Rb^*He_N complexes has even been extended by quantum interference methods, enabling measuring the vibrational structure and relaxation of the Rb^*He_1 bond [80].

5.2 Principle of the experiment

The experiment aims to measure the solvation dynamics of an alkali ion, in terms of how quickly the solvation shells of solvent build up around the ion, see Section 5.1.2. Thereby, the core observable is the number of helium atoms attached to the individual alkali ions measured, and how this number changes as a function of time.

A sketch of the experimental principle is shown in Fig. 5.2. Fig. 5.2(a) shows helium droplets that are double doped with a Na atom, on the surface, and a Xe atom, in the interior, see Section 2.5. The solvation is initialized by selectively ionizing the Na atom with a femtosecond pump laser pulse. The intensity of the pump pulse is sufficiently height that it effectively ionizes Na atoms (Ionization potential (IP): 5.1 eV [60]), and sufficiently low that the ionization of Xe (IP: 12.1 eV [60]) is negligible. The suddenly created Na^+ is not in equilibrium at the surface, and begins its solvation process, see Fig. 5.2(b). According to the TDDFT simulation, this involves by attracting He atoms to build up a Na^+He_N complex, and eventually moving into the droplet. This solvation process is allowed to continue for some time, t, at which the probe pulse ionizes the Xe atom. The Xe^+ ion suddenly creates an electrostatic force on the Na^+ ion which expels it from the droplet along with a number, N, of He atoms that are sufficiently strongly bound to the Na^+ ion at that time, see Fig. 5.2(d). The free Na^+He_N is accelerated

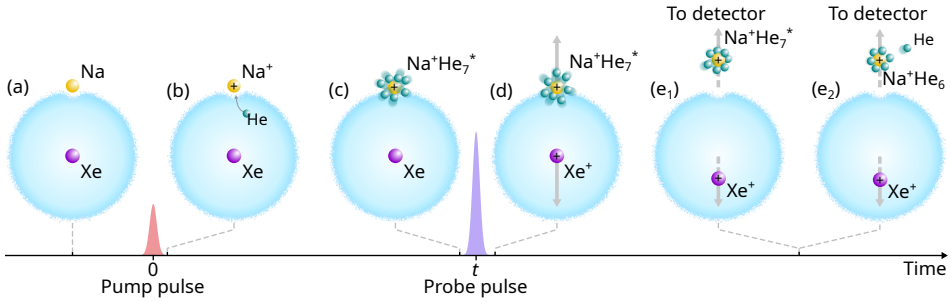

Figure 5.2: Principle of the experiment. (a) The initial double-doped helium nanodroplet. (b) Just after the pump laser pulse, the Na atom has been selectively ionized, initiating the Na^+ solvation. (c) Just before the probe pulse, the Na^+ ion has attached several He atoms. (d) Just after the probe pulse, the Xe atom has been ionized, repelling the Na^+He_N complex from the droplet. (e_1) The intact Na^+He_N complex flies towards the detector. (e_2) The Na^+He_N complex sheds a helium atom, and the resulting Na^+He_n complex flies towards the detector. Adapted from [2], own original work.

towards the detector by the VMI spectrometer, which measures the masses and kinetic energies of the ions created by the laser pulses. Thereby, the number of helium atoms in the solvation complex can be deduced. However, at the time of repulsion, the Na^+He_N complex is probably not completely relaxed. It is possible that it undergoes internal vibrational relaxation by ejecting one or more helium atoms, see Fig. 5.2(e_1-e_2). For this reason, we will denote the detected complex Na^+He_n, and the surface bound complex at time t Na^+He_N, with $n \leq N$. The effect of this post-ejection dissociation will be discussed in the following sections.

5.3 Experimental details

The experimental setup used has already been explained in detail in Chapter 3. This section will go through the setup briefly, to give the experimental details that are relevant for the results.

5.3.1 Droplet creation and doping

The droplets were created using the same subcritical expansion through a 5 µm orifice described in Section 3.2. For this experiment, a stagnation pressure of 50 bar

and a nozzle temperature of 18 K was used, leading to an expected average droplet size of $\langle N \rangle$ =5200 atoms, equivalent to an average radius of 4.05 nm, see Table 2.1.

The droplets were first doped with Xe by passing them though a gas cell, then with Na by passing them though an oven cell, as described in Section 3.3. The Xe doping level is controlled by the opening of a leak valve backed by 0.7 bar of Xe gas, see Section 3.3.1. The Na doping level is controlled by the temperature of the oven cell, with a temperature of 150 °C used for the experiment, see Section 3.3.2. The doping levels were optimized iteratively by optimizing the strength of the kinetic ion channels corresponding to Na^+He_n. Due to the statistical nature of the doping process, it is unavoidable that some droplets are doped with other numbers the dopants, like for instance Na_2 dimers.

5.3.2 Optical setup

The optical setup used was functionally identical to the one shown in Fig. 3.3. The 1 kHz Spitfire Ace laser system was used.

The *pump beam* used had the native wavelength of 800 nm, and was linearly polarized in the detector plane (horizontal polarization). The pulse length was measured to be $\tau_{FWHM} = 65$ fs by autocorrelation, see Section 3.4.8, and the focused beam radius was measured to be $w_0 = 24\,\mu$m by a beam profiler, see Section 3.4.7. The pulse energy was 35 µJ ($P_{\text{avg}} = 35$ mW average beam power at a repetition rate of $f_{\text{rep}} = 1$ kHz). Assuming that the pulse was gaussian both spatially and temporally, and using Eq. (3.6), this gives a peak intensity[2] of $I_0 = 5.8 \times 10^{13}$ W/m^2. This intensity was chosen to maximize the Na ionization yield, while avoiding the ionization of Xe, in accordance with the principle of the experiment. Furthermore, the focused beam radius was set to be larger than that of the probe beam, to ensure that the probe beam only addresses droplets that have been irradiated by the pump beam.

For the *probe beam*, second harmonic generation (SHG) was used to change the wavelength to 400 nm. This wavelength was used to minimize the effect of dissociative ionization of Na_2 dimers in the experiment, an effect that will be discussed further in Section 5.4. The SHG was done in a BBO crystal (0.5 mm thickness, 22.4°), see Section 3.4. The focused beam radius was measured with the same beam profiler as the probe beam to be $w_0 = 16\,\mu$m. The pulse length

[2]The *very* attentive reader might realize that this is different from the value published in [2] by a factor of 4. This stems from an error in the paper, where the beam *diameter*, $2w_0$, was used in place of the *radius*, w_0.

was measured via ion signal cross correlation between the pump and the probe pulse, giving $\tau_{\mathrm{FWHM}} = 90\,\mathrm{fs}$. The pulse energy was $E_p = 35\,\mu\mathrm{J}$ ($P_{\mathrm{avg}} = 35\,\mathrm{mW}$, $f_{\mathrm{rep}} = 1\,\mathrm{kHz}$), coincidentally the same as the pump beam. Using Eq. (3.6), this gives a peak intensity of $9.1 \times 10^{13}\,\mathrm{W/cm^2}$. This was experimentally optimized to maximize the Xe^+ signal, while avoiding the ionization of He, and staying within the ion hit rate limits of the MCP detector.

The two beams from the two arms were overlapped to be collinear using a dichroic mirror that reflects the 400 nm pump beam and transmits the 800 nm probe beam. The collinear beams were focused into the chamber using an achromatic doublet lens with a focal length of 30 cm, placed 30 cm from the center of the VMI spectrometer. Observing the distribution of ions on the detector while setting the VMI spectrometer to spatial focus mode, the focus of the probe beam in the chamber was adjusted using the telescope, see Fig. 3.3. Afterwards, the beam profiler position was adjusted to be at the probe beam focus, and using the beam profiler as reference, the focus of the pump beam was adjusted to be at the same position. The exact temporal overlap between the two pulses was found by optimizing the nonlinear contribution to the H_2O^+ ion signal. This concludes the laser setup procedure.

In total, 40 pump-probe delays were recorded, in the range 0.2 ps to 20 ps. The smallest delay was chosen to avoid overlap between the pump and probe pulse, while the longest was chosen practically where the dynamics of the signals seemed to have stopped. The 40 points were distributed such as to provide a good sampling of both fast and slow signals.

5.3.3 Ion detection

The laser beams are focused in the center of the VMI spectrometer, where they overlap with the helium droplet beam. The *velocities* of the ions are *mapped* onto the *imaging* detector, projecting the full 3D velocity distribution onto a 2D spatial distribution, as described in Section 3.5. The optimized velocity focus voltages used in this experiment were $V_R = 6000\,\mathrm{V}$, $V_E = 3830\,\mathrm{V}$, and $V_G = 0\,\mathrm{V}$.

The ions hit the chevron type MCP detector biased with a front voltage of $V_F = -600\,\mathrm{V}$ and a back voltage of $V_B = 1200\,\mathrm{V}$, see Section 3.6. The resulting electron avalanche hits a phosphor screen biased to $V_{Ph} = 4200\,\mathrm{V}$, which lights up in the hit spot. This light is collected by the TPX3Cam, which after clustering and centroiding records the time-of-flight (TOF) and (x, y) detector coordinates of

each ion hit, as described in Section 4.1. The TOF values are also corrected for time-walk effects, as described in Section 4.2.

After this post-treatment, the resulting data of the experiment is a list of detected ion hits, recording the (x, y) detector coordinates, TOF, laser shot number, and pump-probe delay t for each. In the following sections, it will be described how this data is reduced down to usable experimental results.

5.4 Extracting ion yields

The base observable of this experiment, from which all experimental results are derived, are the time-dependent ion yields of the various helium tagged sodium ions, Na^+He_n for $n \geq 0$. That is, the number of Na^+He_n ions detected per laser shot, as a function of the pump-probe delay.

Firstly, the TOF of each ion event is calibrated to an equivalent mass-over-charge ratio (m/q), as explained in Section 3.5. Thereby, all events can be binned to create a mass-over-charge spectrum, which is shown in Fig. 5.3(a). From this, the ion hits are divided into different ranges of m/q, corresponding to the Na^+He_n with $m/q = (23\,\mathrm{u} + n \cdot 4\,\mathrm{u})/e$, the used ranges are shown in Fig. 5.3(a). Peaks corresponding to Na^+He_n are identified for the range $n = 0 - 25$, as Na^+He_{26} and beyond overlap with the strong Xe^+ and Xe^+He_n signals. For each ion hit in each of the mass ranges, the x and y detector coordinates are calibrated to the projected velocity components v_x and v_y, as detailed in Section 3.5. This is done by fixing the kinetic energy of Na^+ ions from the Coulomb explosion of Na_2 dimers in the triplet ($^3\Sigma_u^+$) state to the well known reported value of $E_{kin} = 1.39\,\mathrm{eV}$[62]. Examples of pump-probe-delay integrated VMI images are shown in Fig. 5.3(b1-b6). To provide time resolution, however, the ion hits of each mass selection is further divided according to pump-probe delay, and in Fig. 5.3(c1-c4) VMI images of Na^+He_3 are shown for some different pump-probe delays as an example. Each of the t-specific VMI images are reconstructed using the MEVIR algorithm [31]. Thereby, the distribution of reconstructed velocity magnitudes (or speed distribution) are calculated as a function of time, an example for Na^+He_3 is shown in Fig. 5.3(d).

If we assume the selected mass ranges exclusively contain the wanted Na^+He_n ion signals, then this analysis of the ion velocities would be unnecessary. However, the intense laser pulses do not discriminate in what species they ionize in the vacuum chamber, which leads to background ion signals that might overlap with the wanted Na^+He_n signals. These background signals can be directly seen in

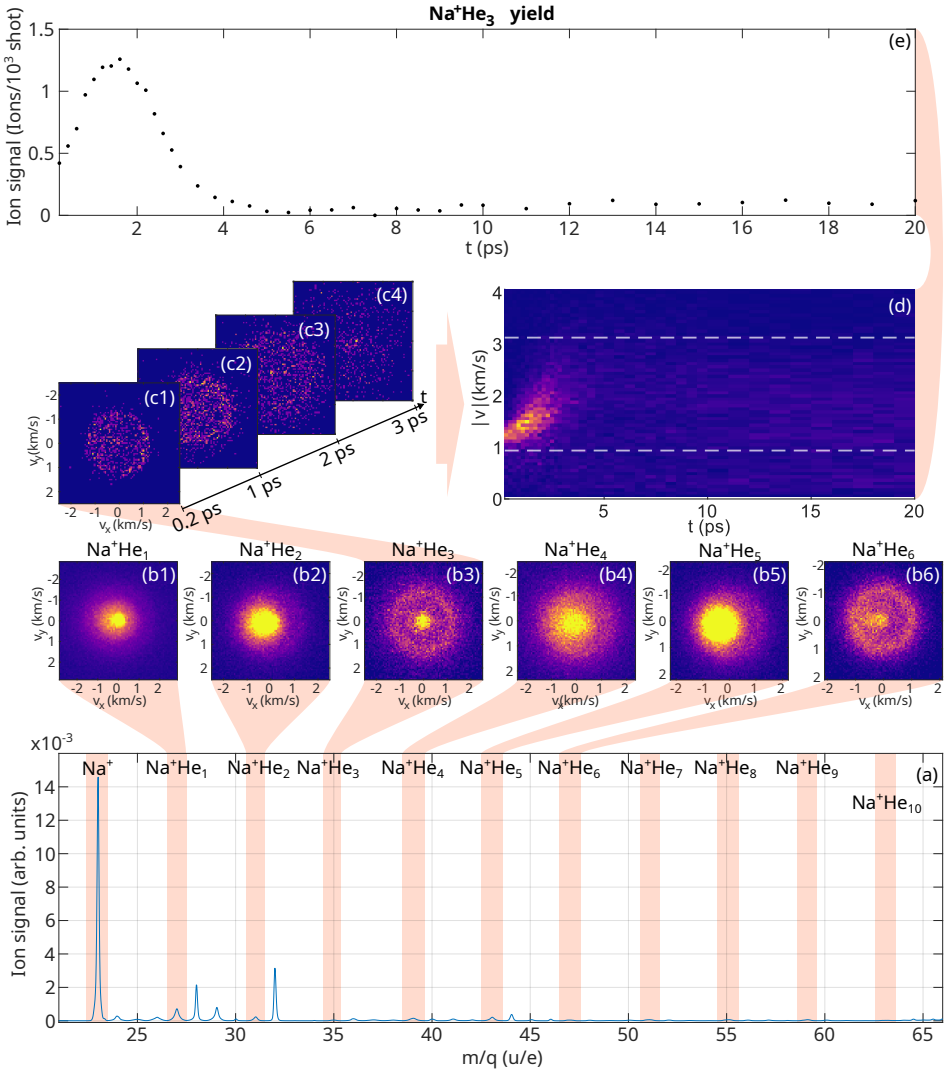

Figure 5.3: Illustration of the data analysis done to extract the time-dependent ion yields. (a) Mass spectrum of the recorded ion hits. (b1-b6) VMI images extracted from specific mass ranges, corresponding to the Na^+He_n complexes, integrated over all pump-probe delays, t. (c1-c4) VMI images of the Na^+He_3 ion hits shown for four specific t. (d) Reconstructed Na^+He_3 radial velocity distribution as a function of t, dashed lines indicating the integration limits used for (e) the Na^+He_3 yield as a function of t. Adapted from [2], own original work.

Fig. 5.3(b1-b6) as the bright and sometimes off-center regions[3]. In order to eliminate background contributions, the time-dependent speed distributions are integrated over a selected range of speeds, as indicated by dashed lines in Fig. 5.3(d). This leads to the time dependent Na^+He_n yield shown in Fig. 5.3(e), for which a constant background signal has been subtracted. Thereby, the Na^+He_n ion hits are selected based on whether they conform to the expected speed channels from the Xe^+ – Na^+He_n repulsion. For further discussion of these channels, see Chapter 6. A range of the resulting Na^+He_n ion yields are shown in Fig. 5.4.

We assume that the background signal present in the non-Na^+He_n ion channels have no time dynamics, and that they can therefore be subtracted as a constant background. To test this assumption, the experiment was repeated with droplets doped only with Na atoms. Thereby, the Xe^+ – Na^+He_n repulsion that leads to the ion yield should not be possible, and the ion yields should be constantly zero. The results of this experiment is shown in Fig. 5.4 as gray circles. Overall, the results show that without Xe in the droplets the ion yields have no time dynamics. However, in Fig. 5.4 (a_1) and (a_2) minor time evolution is seen, with signal rising slightly during the first 5 ps. This is believed to be due to some dynamics in the Na_2 dimers induced by the pump pulse, leading to Na^+ ion that then attaches He atoms. The pump and probe beam wavelengths were specifically selected to minimize this, and shift it to a speed channel that does not overlap with the wanted Xe^+ – Na^+He_n repulsion channels.

In conclusion, by all tested metrics the experiment measures the ion yield of Na^+He_n stemming from the process discussed in Section 5.2.

5.5 Modelling the He attachment rate

The ion yields shown in Fig. 5.4 show a series of peaks, where larger Na^+He_n complexes peak at gradually later pump-probe delays. This reflects the mechanism that it takes longer to attach a higher number of helium atoms to the Na^+ ion. In order to quantify this rate of attachment, we need to compare the experimental data to some model. In this section, I will explain how the rate of attachment of the first five helium atoms is found by fitting to a *Poisson model*.

[3]The images are centered on the Xe^+ – Na^+He_n repulsion channels stemming from the droplets, which move at a speed in the range $200\,\mathrm{m\,s^{-1}}$ to $400\,\mathrm{m\,s^{-1}}$ [113]. Signals coming from the vacuum chamber will thereby be centered between $-200\,\mathrm{m\,s^{-1}}$ to $-400\,\mathrm{m\,s^{-1}}$ in the droplet-centered VMI images.

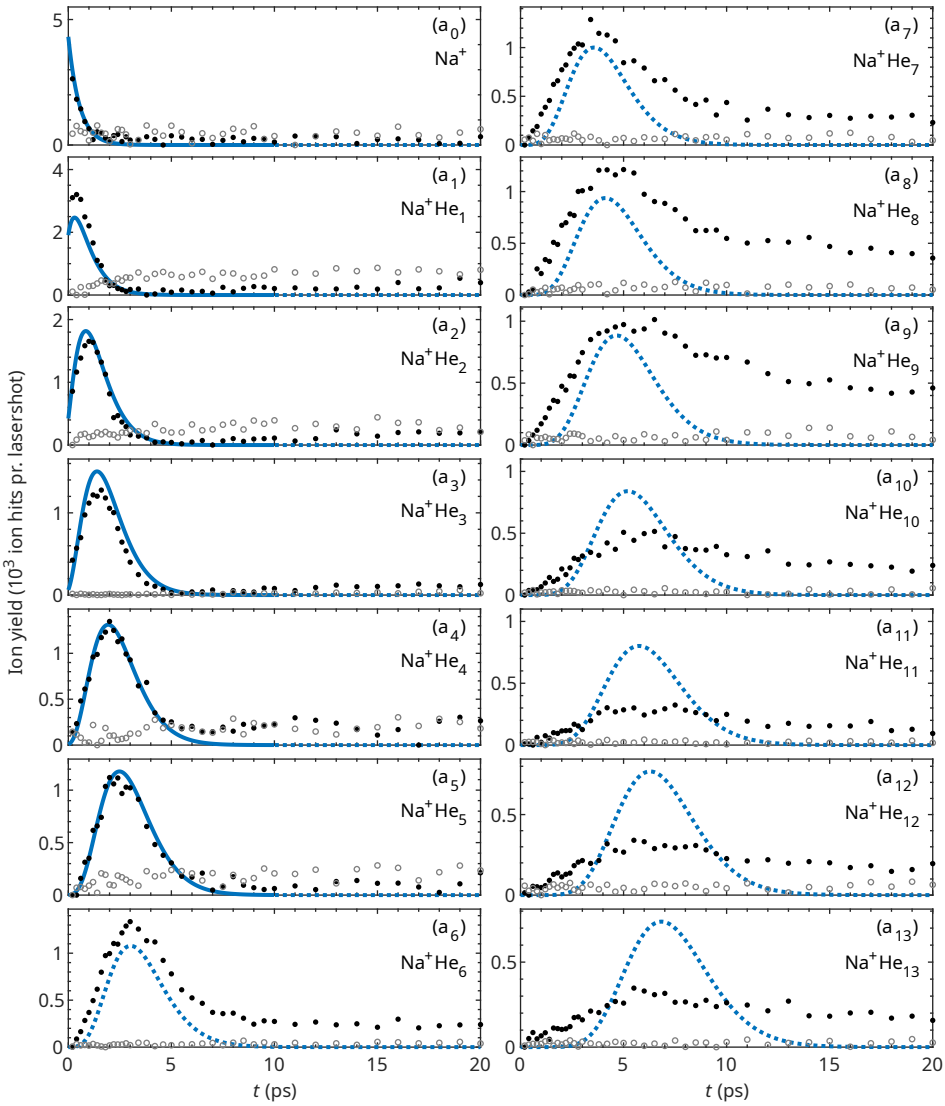

Figure 5.4: Experimental ion yields of Na^+He_n as a function of pump-probe delay, t, for a selected range of n. Black dots: Data identified to be from the Xe^+ – Na^+He_n repulsion, as described in Section 5.2. Gray circles: Data from repeated experiment without Xe doping. Blue lines: Poisson function fit, with solid lines marking the range of data fitted to, dashed lines marking extrapolation beyond the fitting range, see text. Adapted from [2], own original work.

A Poisson distribution describes the total number of events that happen within a time t, when the events are independent and happen at a constant rate in time λ_{He}. The mean of the distribution is then $\lambda_{\mathrm{He}}t$, while the probability mass function describing the probability of having N events during a time t is [19, sec. 1.3.2]

$$P(N) = \frac{(\lambda_{\mathrm{He}}t)^N}{N!}e^{-\lambda_{\mathrm{He}}t}. \tag{5.1}$$

For this model, we will assume that the Poisson distribution describes the number of helium atoms N attached to the Na^+ on the surface of the droplet. This means that the He attachment events need to be independent, that is, the physical process of attaching a He atom to the Na^+ ion should not depend on how many atoms are already attached to the ion. To justify this assumption, we look at how much the binding energy changes when going from a Na^+He_{N-1} complex to a Na^+He_N complex, called the *evaporation energy*, E_{evap}, with the definition

$$E_{evap}(N) = E_{bind}(\mathrm{Na^+He_N}) - E_{bind}(\mathrm{Na^+He_{N-1}}). \tag{5.2}$$

To calculate these values, one needs to calculate the total binding energy of the Na^+He_N complexes, $E_{bind}(\mathrm{Na^+He_N})$. The state-of-the art technique used for this is *Path Integral Monte Carlo (PIMC)* calculations [92]. While reference [92] only provides E_{evap} for Li^+He_N complexes, Tomás González-Lenzana and his group has kindly provided E_{evap} for Na^+ ions and K^+ ions as well [42]. These are shown in Fig. 5.5, where it is seen that E_{evap} is approximately constant for Na^+ for $N = 1-6$. This is interpreted as the first 6 helium atoms not feeling the repulsion of the already attached helium atoms, which makes it plausible that these attach independently to the Na^+ ion. For now, we also assume that the attachment events happen at a constant rate in time, the physical implications of which will be discussed later.

When comparing the Poisson model to the data, it is important to remember that we do not record the Na^+He_N complexes on the droplet surface, but rather the Na^+He_n complexes that reach the detector. In Fig. 5.5 it is seen that E_{evap} falls off strongly for $N > 6$, and thereby, it is more likely that the $Na^+He_{N>6}$ complexes undergo dissociation during the repulsion from the droplet. For example a Na^+He_7 complex could undergo dissociation and be recorded as a Na^+He_6 complex. This has two major implications for the correspondence with the Poisson model: Firstly, we assume that dissociation effects imply that Na^+He_N for $N > 6$ will deviate from the Poisson model. Secondly, as Na^+He_6 is likely to be created from the dissociation of Na^+He_7, but unlikely to dissociate into Na^+He_5, we expect the

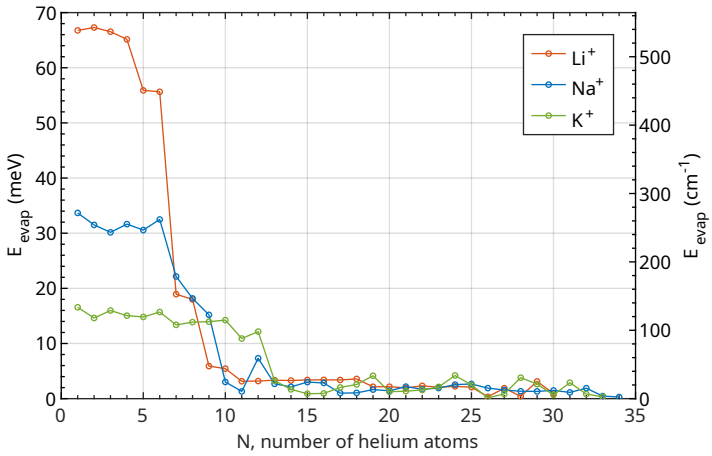

Figure 5.5: Evaporation energy as a function of number of helium atoms, see Eq. (5.2), for Li^+, Na^+ and K^+ ions. Li^+ data from [92], Na^+ and K^+ data from [42].

Na^+He_6 ion yield to be too high compared to the expected Poisson model, and therefore, this ion yield will be excluded from comparison with the model as well. For the range, $n = 0-5$, the peak structures lie in the pump-probe delay interval $t = 0.2$ ps to 10 ps, with the $t = 10$ ps to 20 ps interval covering just noise on an approximately constant signal. For this reason, only the $n = 0-5$ and $t = 0$ ps to 10 ps range is used for comparison with the Poisson model.

We have measured the ion yields as a function of two independent parameters, t and n. Thereby, it should be possible to determine the free parameter in Eq. (5.1), λ_{He} (the attachment rate of helium atoms), by fitting Eq. (5.1) to the data. One adaption is needed, however, as the Na^+He_N complex is not instantaneously repelled from the droplet, but rather has a short time after the probe pulse arrives where it is still in the proximity of helium. During this time, it could potentially attract more helium. We will call this offset the *lift-off time*, t_{lo}. We assume that this lift-off time is independent of both n and t. With this correction, we assume that $n \approx N$, that is, that the measured Na^+He_n correspond well to the Na^+He_N on the surface, this assumption will be discussed later. Thereby, the fitting function becomes

$$P(t,n) = A\frac{(\lambda_{He}(t-t_{lo})^n)}{n!}e^{-\lambda_{He}(t-t_{lo})}, \tag{5.3}$$

with A being the global scaling factor, transforming the time-dependent probability mass function into ion hits per laser shot. With A, λ_{He} and t_{lo} as free parameters, Eq. (5.3) was fitted to the experimental data in the ranges $n = 0-5$ and $t = 0.2\,\mathrm{ps}$ to $10\,\mathrm{ps}$, as a global, two-dimensional, least-squares fit using the standard "fit" method in MATLAB R2022a. The result was $A = 6.7 \cdot 10^{-3}$ ion hits per laser shot, $t_{\mathrm{lo}} = -0.241\,\mathrm{ps}$, and $\lambda_{\mathrm{He}} = 1.8\,\mathrm{He/ps}$ (helium atoms attached per picosecond). The resulting fit is shown as blue lines in Fig. 5.4, with the full lines representing the fitted range, and the dashed lines representing extrapolating Eq. (5.3) beyond the fitted range.

It should be noted that this fitting approach deviates from the analysis presented in reference [2]. In the published paper, the helium attachment rate λ_{He}[4] is found by finding the peak positions of the $\mathrm{Na^+He_{(1-5)}}$ yield curves, and fitting a linear dependence between the peak positions and n. If the Poisson model perfectly describes the data, then the results should be the same, as the peak position of Eq. (5.3) are located at $(t - t_{\mathrm{lo}})/\lambda_{\mathrm{He}}$. The global fit does however take more data than just the peaks into account, and is also sensitive to the relative height of the peaks. For this reason, it is believed to be more accurate than the previous peak-position analysis.

The fitted value of $A = 6.7 \cdot 10^{-3}$ ion hits per laser shot does not give any information about the physical solvation process we are measuring, but might be useful for attempted reproductions of the result. $t_{\mathrm{lo}} = -0.241\,\mathrm{ps}$ tells us that the $\mathrm{Na^+}$ has a few hundred femtoseconds of interaction time after the repulsion process has started, effectively making the data appear as if the solvation process started before the pump-probe overlap. This is consistent with the complexes having to be repelled from the droplets by a finite force from the created $\mathrm{Xe^+}$ ion. This is also apparent in Fig. 5.4, where a significant signal of $\mathrm{Na^+He_{(1-3)}}$ is seen at the earliest recorded time step of 0.2 ps. The helium attachment rate of $\lambda_{\mathrm{He}} = 1.8\,\mathrm{He/ps}$ is the primary result of this analysis. This quantifies the rate of solvation, in the terms of how quickly the solvation shell builds up. The result is, however, limited to describe the attachment of just the first 5 helium atoms.

In the fitted range, the experimental data and model show a good agreement, with well-matching curve shapes. Some peak heights are slightly off. The experimental $\mathrm{Na^+He_1}$ being slightly too high, which can be attributed to the very low amount of binding energy that needs to be dissipated before they are bound. The experimental $\mathrm{Na^+He_3}$ being slightly too low, which could just be an uncertainty

[4]The symbol r is used in the paper.

of the experiment, or it could be attributed to a small amount of dissociation of the $Na^+He_{(1-5)}$ complexes. The experimental Na^+He_n will be too high (low) if the probability of dissociating $Na^+He_{(n+1)}$ is higher (lower) than the probability of dissociating $Na^+He_{(n)}$. This overall agreement suggests that the assumptions used for the model are valid for the first 5 attached helium atoms, most importantly that the attachment events are independent of each other, and that they happen at a constant average rate in time.

Looking beyond the fitted time range for the $Na^+He_{(0-5)}$ yields, the extrapolated Poisson model predicts no ion yield. This corresponds well with the measured ion yields, apart from a slow rise in the yield for some fragments, that correspond well to the rise seen in the yields from the measurement without Xe doping. Thereby, these slow rises are attributed to dissociation effects of the Na_2 dimers.

Finally, looking at the extrapolated Poisson model for Na^+He_n for $n > 5$ in Fig. 5.4 show the following trend: The $n = 6-9$ experimental curves lie above the Poisson curves, while for $n \geq 10$ the experimental curves fall significantly below the Poisson curves. This corresponds well with the progressive decline of $E_{evap}(n)$ for $n = 6-9$ (see Fig. 5.5). This is because $E_{evap}(n) > E_{evap}(n+1)$ should lead to more dissociation of $Na^+He_{(n+1)}$ than of Na^+He_n, thereby accumulating signal in Na^+He_n. Furthermore, the overestimation of signal is more pronounced at later times, which also correspond to signal contribution from dissociation of larger complexes, as these larger complexes are formed later. The $n = 6-9$ curves show a significant tail in the yield at later times, where the Poisson model predicts no yield. This can also be attributed to dissociation of larger complexes. The experimental yields for $n \geq 10$ are generally lower than those predicted, which corresponds well with these complexes having the lowest evaporation energies, i.e. they are depleted due to dissociation. An alternative explanation based on the distribution of droplet sizes in the experiment will be discussed in Chapter 7.

The final thing that is unexplained for the $n \geq 6$ complexes is why the experimental ion yields rise too quickly compared to the predicted Poisson model. So far, this section has not discussed what limits the rate of attachment in the Poisson model picture. In Section 5.6, it will be discussed that the limiting factor is probably the dissipation of vibrational energy from the Na^+He_N complexes into the droplets, with a thermal-like energy transfer being the main mechanism. If this is true, then the early rise of the ion yields of the larger complexes suggests that another energy dissipation mechanism contributes at early times. This could for instance be three-body collisions, in which two helium atoms collide with the Na^+He_N at the same time, leading to a bound $Na^+He_{(N+1)}$ complex, while the last

helium atom is ejected, carrying off the binding energy of the complex as kinetic energy. This is one possible explanation of the early rise of the larger Na^+He_n signals, but we currently have no experimental way to test its correctness.

5.6 Energy dissipation

In the previous section, it was discussed how the potential dissociation of Na^+He_N complexes limits which Na^+He_n signals can be used to quantitatively characterize the helium attachment dynamics. In this section, it will be discussed how the very same dissociation mechanism enables a measurement of how much Na^+He_N binding energy has been dissipated to the droplet at the time of repulsion.

5.6.1 Theoretical basis

In order to calculate the dissipated energy, we must carefully consider how the different components of energy of Na^+He_n evolve over time, from initial ionization to detection. For this, attractive potential energies and binding energies will be negative. Just after ionization, the Na^+ will have some binding energy due to its proximity to the yet unperturbed droplet, $E_{\text{dimple}}(Na^+)$. This energy must be dependent on the droplet size, but was calculated to be $-16.2\,\text{meV}$ ($-130.4\,\text{cm}^{-1}$) for a droplet containing 5000 helium atoms in [2]. As time goes on, the Na^+He_N binding energy is expected to increase. Let $E_{\text{bind}}(Na^+He_N)$ denote the binding energy of the isolated and fully relaxed Na^+He_N complex. The complex is, however, not immediately fully relaxed, and will have some internal energy, $E_{\text{int}}(Na^+He_N)$. At any given time after ionization but before repulsion, the difference between the total energy of the complex and the initial energy of the Na^+ ion must be the amount of energy that has been dissipated into the droplet,

$$E_{\text{disp}}(N) = -E_{\text{bind}}(Na^+He_N) - E_{\text{int}}(Na^+He_N) + E_{\text{dimple}}(Na^+). \qquad (5.4)$$

As the Na^+He_N complex is repelled from the droplet, the repulsion process itself might add energy to the complex, which would be an increase of $E_{\text{int}}(Na^+He_N)$. After this the Na^+He_N is free. If $E_{\text{int}}(Na^+He_N) > E_{\text{evap}}(N)$, then it is energetically possible for the complex to dissociate, thereby turning into a Na^+He_{N-1} complex. This specific channel of dissociation where the most weakly bound He atom is ejected will be called *evaporation*. All that is needed for this is that at least $E_{\text{evap}}(N)$ localizes in the weakest Na^+–He bond, which will happen eventually as the internal energy fluctuates randomly between the different internal degrees of freedom.

We assume three things about this sequential evaporation process, all of which will be argued for below.

1. The evaporated He atoms carry off no translational kinetic energy, which implies that the total energy of the complex must remain constant during evaporation. We assume that his holds for all evaporation events until the complex reaches its final size, n, that is,

$$E_{\text{bind}}(\text{Na}^+\text{He}_\text{N}) + E_{\text{int}}(\text{Na}^+\text{He}_\text{N}) = E_{\text{bind}}(\text{Na}^+\text{He}_n) + E_{\text{int}}(\text{Na}^+\text{He}_n). \tag{5.5}$$

2. The sequential evaporation process continues until the internal energy is too low to evaporate off the next atom. At this point the complex has reached its final size n, which is also what will be detected. That is,

$$0 \leq E_{\text{int}}(\text{Na}^+\text{He}_n) < E_{\text{evap}}(n). \tag{5.6}$$

3. The whole sequential evaporation sequence happens so quickly that it is the mass of the final Na^+He_n complex that we measure by TOF with the VMI spectrometer. That is, the measured Na^+He_n complex is relaxed, and must have an internal energy below $E_{\text{evap}}(n)$, as described above.

By combining Eq. (5.4), Eq. (5.5) and Eq. (5.6), we can calculate an upper and lower limit of E_{disp},

$$-E_{\text{evap}}(n) < E_{\text{disp}}(n) + E_{\text{bind}}(\text{Na}^+\text{He}_n) - E_{\text{dimple}}(\text{Na}^+) \leq 0. \tag{5.7}$$

This equation can be simplified by writing up $E_{\text{bind}}(\text{Na}^+\text{He}_n)$ in terms of the evaporation energy,

$$E_{\text{bind}}(\text{Na}^+\text{He}_n) = \sum_{i=1}^{n} -E_{\text{evap}}(i), \tag{5.8}$$

and the dissipated energy can thereby be written as,

$$-E_{\text{bind}}(\text{Na}^+\text{He}_{n-1}) + E_{\text{dimple}}(\text{Na}^+) \leq E_{\text{disp}}(n) < -E_{\text{bind}}(\text{Na}^+\text{He}_n) + E_{\text{dimple}}(\text{Na}^+). \tag{5.9}$$

Thereby, under the assumptions we have made about the evaporative relaxation of the initially excited $\text{Na}^+\text{He}_\text{N}$ complex, we can quantify the amount of energy that must have been dissipated to the droplet to create each detected Na^+He_n complex. But before this theoretical treatment is applied to the data, we first need to argue for the three assumptions, which will be done below.

1: Evaporated He atoms carry off no energy If the Na^+He_N ion ejected from the droplet surface has a higher internal energy than $E_{evap}(N)$, then it is metastable. That is, the internal energy initially distributed in a way such that no single Na^+-He bond has a higher excitation energy than its binding energy. However, coupling between the excitation modes of the different bonds will randomly redistribute the energy between them. When the weakest bond reaches an excitation energy just above $E_{evap}(N)$, then that bond will break, and the involved He atom will fly off. However, as the bond excitation has only just exceeded the binding energy, there is no excess energy in the bond for the He to gain as translational kinetic energy.

This argument is somewhat supported by the literature, for instance reference [44] experimentally finds that the dissociation products of the metastable $X-CH_3Y$ (X = Cl, Br; Y = Br, I) molecules have very little translational kinetic energy. While this supports the assumption, it is not completely clear how these results translate to the dissociation of our Na^+He_N complexes. As the evaporated He atoms are in a neutral charge state, we are however not able to measure their kinetic energies with the VMI spectrometer.

In order to investigate the assumption for the specific system, molecular dynamics (MD) simulations of the Na^+He_N system were carried out. I was not personally very involved in carrying out these MD simulations, these were rather the contribution of Christian Engelbrecht Petersen and Jeppe Kjædegaard Christensen in reference [2]. For this reason, I will only give a brief account of how these simulations were carried out, with more details given in reference [2]. Essentially, Na^+He_N complexes were created, and the energy was minimized by optimizing the structure. From this minimum energy structure, internal energy is introduced to the complex by assigning random velocities to the Na^+ and He atoms according to a Maxwell-Boltzmann distribution. This is done progressively over 100 fs, whereby no dissociation occurs during the heating of the complex. The internal energy is noted, and then time evolution is simulated in the MD simulation. Thereby, the number of attached helium atoms can be determined as a function of time, and furthermore, the velocity of the detached helium atoms can be recorded. The distribution of kinetic energies of the evaporated He atoms can be seen in Fig. 5.6(c-d), for two different initial complex sizes, and for different amounts of excitation energy given to the relaxed complex, E_{init}. The figure shows that the average kinetic energy per helium atom is less than 5 meV in all cases. For the lowest excitation energy, the larger Na^+He_{15} complex shows an average helium kinetic energy of about 1 meV, while no evaporation was detected for the smaller Na^+He_6 complex.

The MD simulation confirms that a single evaporated helium atom will only

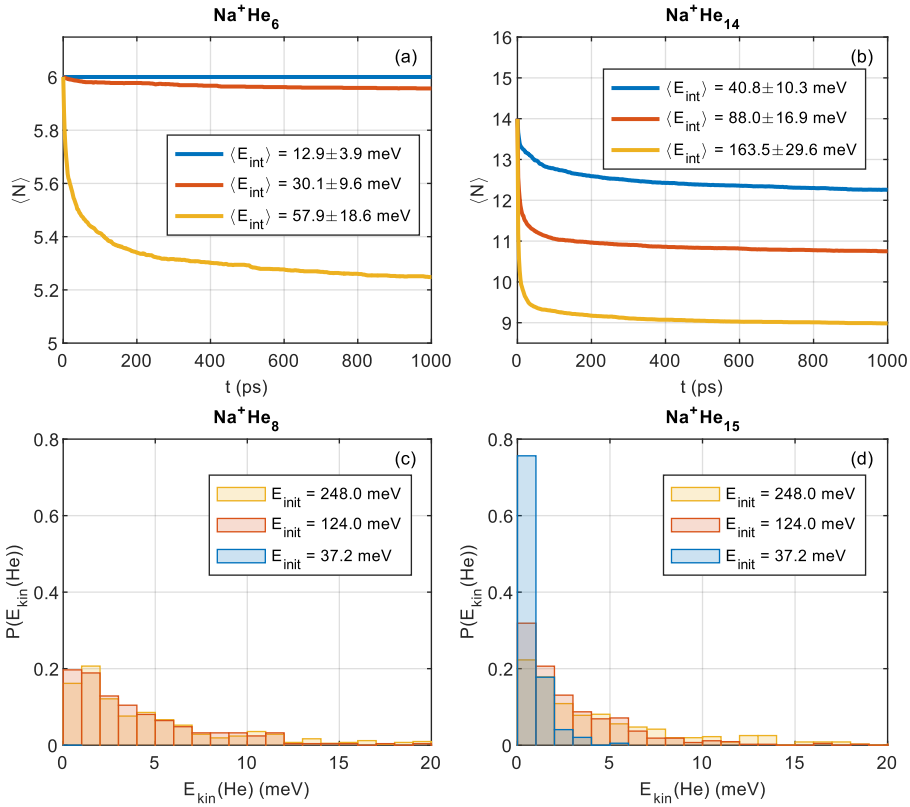

Figure 5.6: Results of the molecular dynamics simulations of the evaporation of He atoms from the Na^+He_N complex. (a) and (b): the average number of helium attached as a function of time after excitation of Na^+He_6 and Na^+He_{14} respectively. The average and standard deviation of the initial internal energy of the complexes are given in the legend. (c) and (d) normalized histograms of the kinetic energy of evaporated helium atoms from the two different initial complexes Na^+He_8 and Na^+He_{15}. The excitation energy given to the complex is given in the legend.

carry off a small fraction of the internal energy of the complex with it. The assumption that the helium atoms carry *no* kinetic energy is not perfect however, and the influence on this on the results of this section will be discussed later.

2: He evaporates until the remaining internal energy is too low to do so In Fig. 5.6(a), the average number of helium atom attached to the Na^+ ion is shown as a function of time after exciting the initial Na^+He_6 complex, more specifically, this average has been taken over 975 repetitions of the MD simulation. This is seen for a range of different initial internal energies. Here it is shown that for an initial internal energy of (12.9 ± 3.9) meV no helium evaporates off. This is in good correspondence with an energy of $E_{\text{evap}}(6) = 32.5$ meV needed to evaporate the least bound He atom. The ensemble distribution of internal energies just overlaps with $E_{\text{evap}}(6)$ for (30.1 ± 9.6) meV, which gives a small amount of He evaporation seen as the average number of helium atoms reaching ≈ 5.95. Most of the internal energy distribution is sufficient to evaporate a helium atom for the (57.9 ± 18.6) meV run, and the Fig. 5.6(a) shows that most complexes evaporate off a helium atom. This is consistent with the assumption that the complexes will evaporate off helium atoms if enough internal energy is present to do so.

The same argument can be made for the Na^+He_{14} run shown in Fig. 5.6(b), where the average was taken over 425 runs of the simulation. The correspondence between the number of helium atoms evaporated and the evaporation energies is less good, with the simulation generally showing less evaporation than expected. This can probably be ascribed to the MD simulation being a simpler physical model than the PIMC calculation used to calculate E_{evap}, which should especially matter in the case for larger Na^+He_N complexes where the He-He interaction plays a more important role.

3: Timescale of the evaporation process From the MD simulation, we find that the vast majority of the evaporation happens within the first 1 ns. Like described above, the average number of helium atoms attached to the Na^+ ion is calculated as a function of the time after excitation of the complexes. Any He atoms within a radius of 10 Å from the Na^+ ion were defined as being attached. The results are shown in Fig. 5.6(a-b), where it is evident that the vast majority of the evaporation happens within the first 1 ns, for a range of different initial complex sizes and internal energies. Furthermore, the kinetic energy of the helium atoms were recorded at the first time step after detachment.

The experiment identifies the different Na^+He_n complexes by their time-of-flight (TOF) from the VMI spectrometer to the detector. If the evaporation process takes too much time, then it would influence the TOF measurement. The worst case scenario must be when the complex undergoes the largest relative mass change at the latest possible time. As an example, I will here treat mass change 43 u to 23 u, corresponding to Na^+He_5 evaporating off all of its helium atoms. In the physical process, this evaporation will happen gradually, however, as a worst case example, I will treat the mass change as all happening at a certain time. To quantify the effect, a simulation of the VMI spectrometer as described in Section 3.5 was made in SIMION 8.0.4, with a resolution of 10 grid-units per millimeter. 5000 ions were created, with positions sampled from a uniform cylindrical distribution centered in the middle between the repeller and extractor plates of the VMI spectrometer, with the distribution having a length of 1 mm along the laser propagation direction, and a radius of 40 µm. The ions were given random directions, and their kinetic energies were set to be (1.65 ± 0.10) eV. In the simulation, the mass of the ions was switched from the initial 43 u to 23 u at the time t_{diss}. The mean TOF of the ions was found, and compared with ions that have mass 23 u for the entire simulation. The result is shown in Fig. 5.7. In the experimental data, the width of the TOF gate that signifies Na^+ ions is 74.5 ns. Based on the SIMION results, the dissociation time of a complex would need to be at least 100 ns in order to shift its measured mass outside this gate, which is two orders of magnitude slower than what is found in the MD simulations.

In conclusion, the evaporation will always result in the measurement of the final complex size Na^+He_n. Based on the above assumptions, we thereby measure relaxed Na^+He_n complexes.

5.6.2 Data analysis

Based on the above assumptions, every measured Na^+He_n complex corresponds to a range of energy that must have been dissipated to the droplet and ejected He atoms, quantified by Eq. (5.9). Thereby, the distribution of Na^+He_n complexes must correspond to a distribution of dissipated energies. If the probability of measuring Na^+He_n is $P(n)$ then the probability of E_{disp} being in the range described by Eq. (5.9) must also be $P(n)$.

Thus, we need to estimate $P(n)$ from the experimental data. Based on the experimental principle, see Section 5.2, the amount of Na^+ ions should stay constant for different pump-probe delays, t, while the distribution of the number of helium

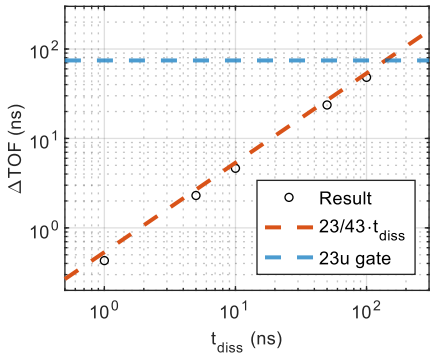

Figure 5.7: SIMION simulation of how much the TOF of an ion that changes mass from 43 u to 23 u at the time t_{diss} differs from an ion with mass 23 u. The simulation results are shown in black circles, which follow the linear trend shown in red dashes at $23/43 t_{\mathrm{diss}}$ reasonably well. Also shown in blue dashes is the 74.5 ns TOF gate width used to identify ions with $m/q = 23\,\mathrm{u\,e^{-1}}$.

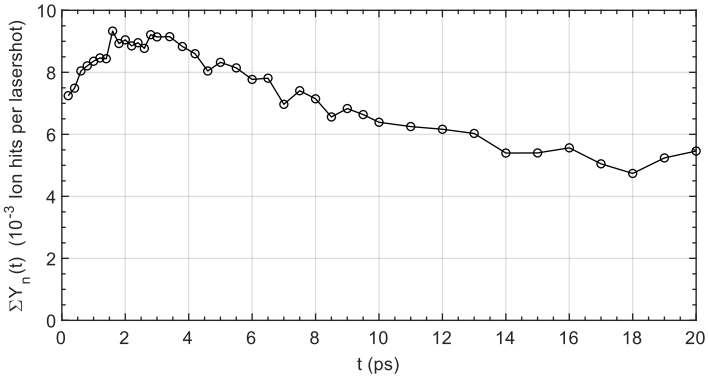

Figure 5.8: Sum of the ion yields of all detected Na^+He_n, $\sum_{n=0}^{25} Y_n(t)$.

atoms attached changes. Assuming that we measure all Na^+He_n complexes with equal efficiency, the t dependent probability of measuring Na^+He_n can be calculated from the ion yields of the complexes, $Y_n(t)$, as

$$P_t(n) = \frac{Y_n(t)}{\sum_{n=0}^{n_{\max}} Y_n(t)}, \tag{5.10}$$

with $n_{\max} = 25$ due to the previously discussed overlap of the Na^+He_{26} complexes and isotopes of Xe^+ ions. This calculation only holds as long as we measure the ion yields of all created Na^+He_n. To test this hypothesis $\sum_{n=0}^{n_{\max}} Y_n(t)$ is plotted in Fig. 5.8, which should ideally be constant. Here a slight rise is seen at early times, below 2 ps. The shape of this rise matches the shape of the fall of the Na^+ ion yield, $Y_0(t)$, seen in Fig. 5.4(a_0). Thereby, the rise in Fig. 5.8 could be explained by an underestimation of $Y_0(t)$. I believe this is caused by selecting a too narrow range of velocities that we integrate the ion signal over. The choice of the narrow range is made because the Na^+ ion images are highly contaminated by ions coming from the Na_2 dimers. Furthermore, the shape of the rise also matches the shape of the rise of the signals measured without Xe doping in Fig. 5.4(a_1-a_2), which as previously discussed can be ascribed to dissociative ionization of Na_2 dimers rather than to the solvation process of Na^+. In conclusion, the early rise of $\sum_{n=0}^{n_{\max}} Y_n(t)$ indicates that the experiment has some minor deviations from the ideal process discussed in Section 5.2. For $t > 4$ ps, $\sum_{n=0}^{n_{\max}} Y_n(t)$ gradually decreases. This can be ascribed to the signal ending up in complexes larger than those we can measure in the experiment, $Na^+He_{n>25}$, which will be further discussed below.

The resulting $P_t(n)$ can be seen for selected times in Fig. 5.9. Like in Fig. 5.4, Fig. 5.9 clearly shows a progression where the distribution of n shifts over time. The fit shown in the figure is exactly the same as the one shown in Fig. 5.4, only normalized to match $P_t(n)$. The effects discussed in Section 5.4 are also visible in this representation of the data, the good fit of the $n = 0-5$ signals to the Poisson model, the overestimation of the $n = 6-10$ signals and the underestimation of the $n = 11-25$ signals. We see a smooth distribution of the $n = 11-25$ signals, and assuming that the $n > 25$ signals follow this trend, only a negligible population should be found in $n > 25$ for $t \leq 5$ ps, matching the earlier conclusion based on Fig. 5.8. Thereby, we believe that we measure all Na^+He_n for $t \leq 5$ ps, and thereby, that we measure the correct $P_t(n)$ distributions for these times.

From $P_t(n)$ and Eq. (5.9), we can now find upper and lower limits of the average

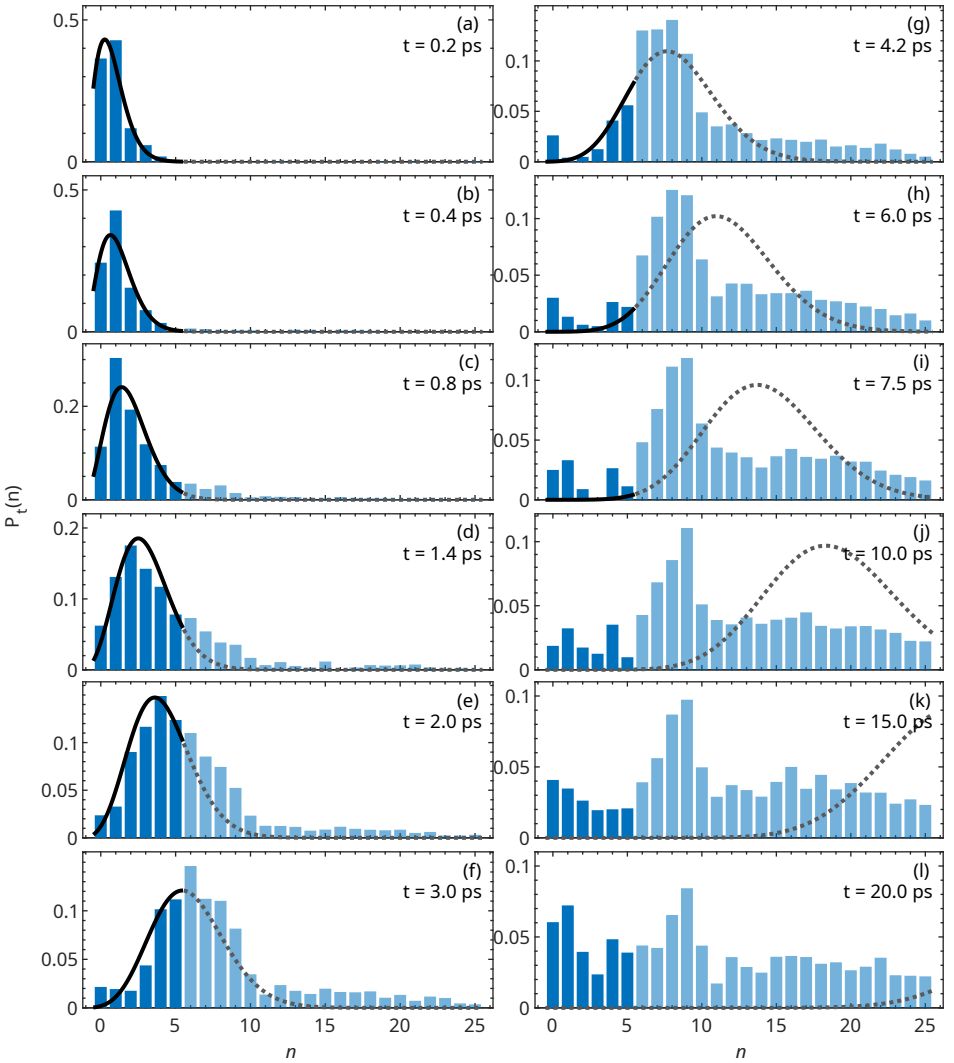

Figure 5.9: Distribution of detected Na^+He_n complexes for the full measured range of $n = 0 - 25$ and select pump-probe delays t. Dark blue bars signify the n fitting range. Also shown is the Poisson model fit, see Eq. (5.3), with the black full line representing the range of data fitted to and the gray dashed line representing the extrapolation of the model beyond this range. Equivalent to Fig. 5.4, except that the distributions have been normalized.

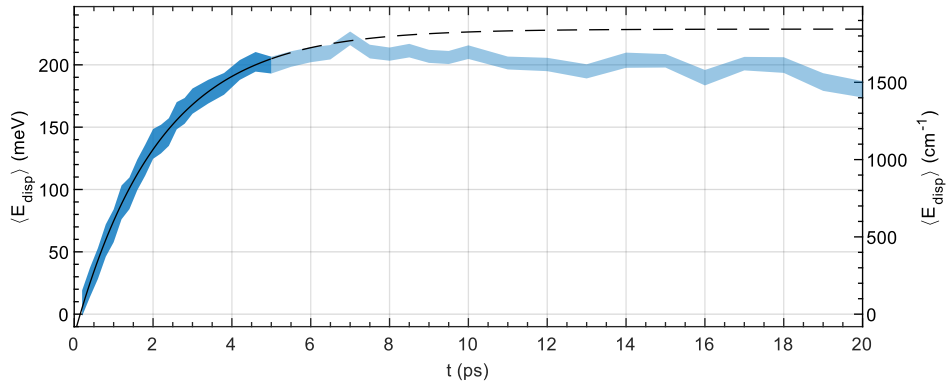

Figure 5.10: Upper and lower bounds for the mean dissipated energy from Na^+He_N complex to the droplet, as a function of t. The dark blue region, $t < 5\,\mathrm{ps}$, is the t range where E_{disp} is expected to be well estimated, see text. The solid black line is an exponential fit using Eq. (5.12), while the dashed black line is the extrapolation of this fit beyond the fitting range.

dissipated energy as a function of t, $\langle E_{\mathrm{disp}} \rangle (t)$, as

$$\begin{aligned} \langle E^{\mathrm{min}}_{\mathrm{disp}} \rangle (t) &= \sum_{n=1}^{n_{\mathrm{max}}} E_{\mathrm{bind}}(n-1) P_t(n) - E_{\mathrm{dimple}}(\mathrm{Na}^+), \\ \langle E^{\mathrm{max}}_{\mathrm{disp}} \rangle (t) &= \sum_{n=1}^{n_{\mathrm{max}}} E_{\mathrm{bind}}(n) P_t(n) - E_{\mathrm{dimple}}(\mathrm{Na}^+), \end{aligned} \tag{5.11}$$

where the $i = 0$ case is omitted from the sums, as they correspond to zero dissipated energy. These limits are plotted in Fig. 5.10, both for the first 5 ps, where the found $P_t(n)$ are trusted, and for the rest of the measurement up to 20 ps. We see that the range that $\langle E_{\mathrm{disp}} \rangle (t)$ lies in is small compared to its magnitude. Initially, we see that the range $\langle E_{\mathrm{disp}} \rangle (t)$ overlaps with 0 meV, which aligns well with our understanding of the experiment. It is also seen that the rate of energy dissipation is initially fast, but lowers significantly as time goes on. It seems that the dissipated energy will reach an asymptotic value, but this value is not quite within the measured range of $t < 5\,\mathrm{ps}$. The experimental conditions could be further optimized so that $P_t(n)$ could be measured for a broader time range, this would require measuring complexes larger than Na^+He_{25}, and thereby require changing the Xe^+ counter ion to another species.

In reference [2], the total difference between the energy of the Na^+ in vacuum and fully solvated in a 5000 atom helium droplet was calculated to be 403.6 meV (3255 cm^{-1}). The difference between this and $E_{\text{dimple}}(Na^+)$, 387.4 meV, must then be the expected upper limit of how much energy can be dissipated to the droplet. In the measurement, however, we only measure that the evaporated energy goes to approximately half of this value, or about 200 meV. This is also reflected in the $P_t(n)$ distributions shown in Fig. 5.9, in which a significant population in $n \leq 10$ is seen even for t approaching the limit of 5 ps, and even for the latest time steps recorded, which keeps the average E_{disp} low. Even if all population was somehow found in $n = 25$, the average would only be $-E_{\text{bind}}(25) - E_{\text{dimple}}(Na^+) = 267.8$ meV. The question of why we do not measure a larger dissipated energy is thereby largely a question of why we measure population in the smaller complexes at later times. One explanation could be that the complex gains internal energy as it is repelled from the droplet, and that this is a stronger effect for larger complexes.

The shape of $E_{\text{disp}}(t)$ seems to be exponential. Newton's law of cooling states that "The rate of heat loss of a body is directly proportional to the difference in the temperature of the body and its environment" [117], which implicitly defines the differential equation describing the change of the energy in the body and the environment as one that has solutions of the exponential form. It is not given that a single ion complex in contact with a superfluid should obey this macroscopic physical law. However, motivated by the law, we write up a model to describe $E_{\text{disp}}(t)$ as,

$$E_{\text{disp}}(t) = E_{\text{disp}}(\infty) \cdot \left(1 - \exp\left(-\frac{(t - \Delta t_{\text{disp}})}{\tau_{\text{disp}}}\right)\right) \tag{5.12}$$

Where $E_{\text{disp}}(\infty)$ is the asymptotic dissipated energy, τ_{disp} is the dissipation timescale, Δt_{disp} is a time-shift comparable to t_{lo} discussed above. We fit this model to the middle of the range $\langle E_{\text{disp}} \rangle$ at each t, in the range $0 < t < 5$ ps. The resulting fit is shown as a black line in Fig. 5.10, where a very good correspondence between data and model is seen. This suggests that Newton's law of cooling applies well to the system. Furthermore, the fit gives $\tau_{\text{disp}} = 2.14$ ps, which will later be compared to τ_{disp} for the solvation of other alkalis.

5.7 Lithium and potassium results

In this section, I will present results on the solvation of lithium and potassium ions. The details of the experiment and analysis are largely the same as what has been

presented for the solvation of sodium ions, and will only be presented briefly. The results shown in this section have not yet been published at the time of writing.

The principle of the experiment is the same as what was described in Section 5.2, only the alkali atom was changed.

5.7.1 Potassium - Experimental details

Firstly, I need to give full credit to Jeppe Kjædegaard Christensen. While the development of the solvation experiment started before he joined our research group, he and I have collaborated strongly on the newest iteration of the experiment, using xenon as the counter ion. Especially for this potassium experiment, Jeppe has independently rebuilt the optical setup and done the actual data acquisition, following the experimental procedure we developed together.

Droplets with an average number of helium atoms $\langle N_{\mathrm{He}} \rangle = 5200$ were created by subcritical expansion of 50 bar helium at a temperature of 18 K through a 5 µm-diameter orifice, as in the Na experiment. The droplets were first doped with Xe atoms in a gas cell, and thereafter doped with K atoms in an oven cell, as detailed in Section 3.3. The oven was loaded with potassium metal and heated to 75 °C. The doping levels were iteratively optimized by optimizing the strength of the t dependent K^+He_n ion signals.

The optical setup used differs from the one used in the sodium solvation experiment, as the 5 kHz Coherent Astrella HE USP laser system had been installed at the time of the experiment. At this time, the optical system was completely rebuilt, but is functionally identical to the one described in Section 5.3, and the final pulse parameters will be given here.

The *pump pulse* used had central wavelength $\lambda = 800\,\mathrm{nm}$, was linearly polarized in the detector plane (horizontal polarization), had a pulse energy of $E_p = 6\,\mu\mathrm{J}$ ($P_{\mathrm{avg}} = 30\,\mathrm{mW}$ average beam power at a repetition rate of $f_{\mathrm{rep}} = 5\,\mathrm{kHz}$). The pulse length was measured to be $\tau_{\mathrm{FWHM}} = 41\,\mathrm{fs}$ by autocorrelation, and the focused beam spot was measured on the beam profiler (FemtoEasy Beampro LP6.3 UV) to have a focused beam radius of $w_0 = 44\,\mu\mathrm{m}$, which gives a peak intensity of $I_0 = 4.5 \times 10^{12}\,\mathrm{W/cm^2}$. This intensity was found by optimizing the ion yield of K^+ ions, while keeping the ion yield of Xe^+ ions to a minimum.

The *probe pulse* had a central wavelength of $\lambda = 400\,\mathrm{nm}$, created by second harmonic generation (SHG) in a BBO crystal (0.5 mm thickness, 22.4°), and was linearly polarized in the detector plane. The pulse energy was $E_p = 26\,\mu\mathrm{J}$, ($P_{\mathrm{avg}} = 130\,\mathrm{mW}$, $f_{\mathrm{rep}} = 5\,\mathrm{kHz}$). The pulse length was measured to be $\tau_{\mathrm{FWHM}} = 51\,\mathrm{fs}$, as the

ion signal cross correlation between the pump and probe beams was measured to have a FWHM of 65 fs. The focused beam radius was measured to be $w_0 = 16\,\mu\text{m}$ on the beam profiler, leading to a peak intensity of $I_0 = 1.2 \times 10^{14}\,\text{W/cm}^2$.

The ion detection is identical to the one described in Section 5.3, the VMI voltages used were $V_R = 6000\,\text{V}$, $V_E = 3793\,\text{V}$ and $V_G = 0\,\text{V}$, where V_E was optimized for the best velocity focus of K^+ ions originating from the effusive beam. The MCP and phosphor voltages were set to $V_F = -600\,\text{V}$, $V_B = 1200\,\text{V}$ and $V_{ph} = 4200\,\text{V}$.

5.7.2 Potassium - Results

Using the TPX3Cam, K^+He_n ions were observed up to $n = 21$, as K^+He_{22} ions have $m/q = 127\,\text{u e}^{-1}$, and overlap strongly with the ion signal of the Xe^+ isotopes. The data treatment is largely identical to the one described in Section 5.4 and especially Fig. 5.3, and will not be described in further detail here. This leads to the ion yields, $Y_n(t)$, represented by back dots in Fig. 5.11.

Poisson attachment model To compare the data to the Poisson model of helium attachment described in Section 5.4, Eq. (5.3) was fitted to the found $Y_n(t)$. As shown in Fig. 5.5, $E_{\text{evap}}(N)$ has a sharp drop-off after $n = 12$, and we therefore exclude $Y_n(t)$ for $n \geq 12$ from the fit. Furthermore, in Fig. 5.11(a_0) it is shown that the measurement without xenon doping has a significant t dependence. This suggests that the wanted $Y_0(t)$ is significantly polluted from signal that does not come from the $Xe^+ - K^+$ repulsion, but might rather come from some dissociative ionization channels of the $K_2{}^+$ dimer. For this reason, $n = 0$ is also excluded from the fit, which is shown as green solid lines in Fig. 5.11. The fitted helium attachment rate, λ_{He}, is $1.7\,\text{He/ps}$. Overall, the peak positions of the data and fit correspond well in the range $n = 1 - 11$, but the exact shape and height of the peaks deviate more than they did for the Na^+ solvation measurement. This will be discussed further in Section 5.7.5.

Dissipated energy From the measured $Y_n(t)$, the distribution of detected K^+He_n ions, $P_t(n)$ was determined, like what was done for Na^+. The sum of the ion yields shown in Fig. 5.16 is quite constant at early times, in correspondence with the experimental principle, while they fall off slowly at longer times, which is interpreted as being due to undetected $n > 21$ complexes. The n-distribution of the K^+He_n signal at selected times is shown in Fig. 5.12. Here, it is clear that K^+He_{12} is overrepresented due to the corresponding dropoff of $E_{\text{evap}}(n)$ from

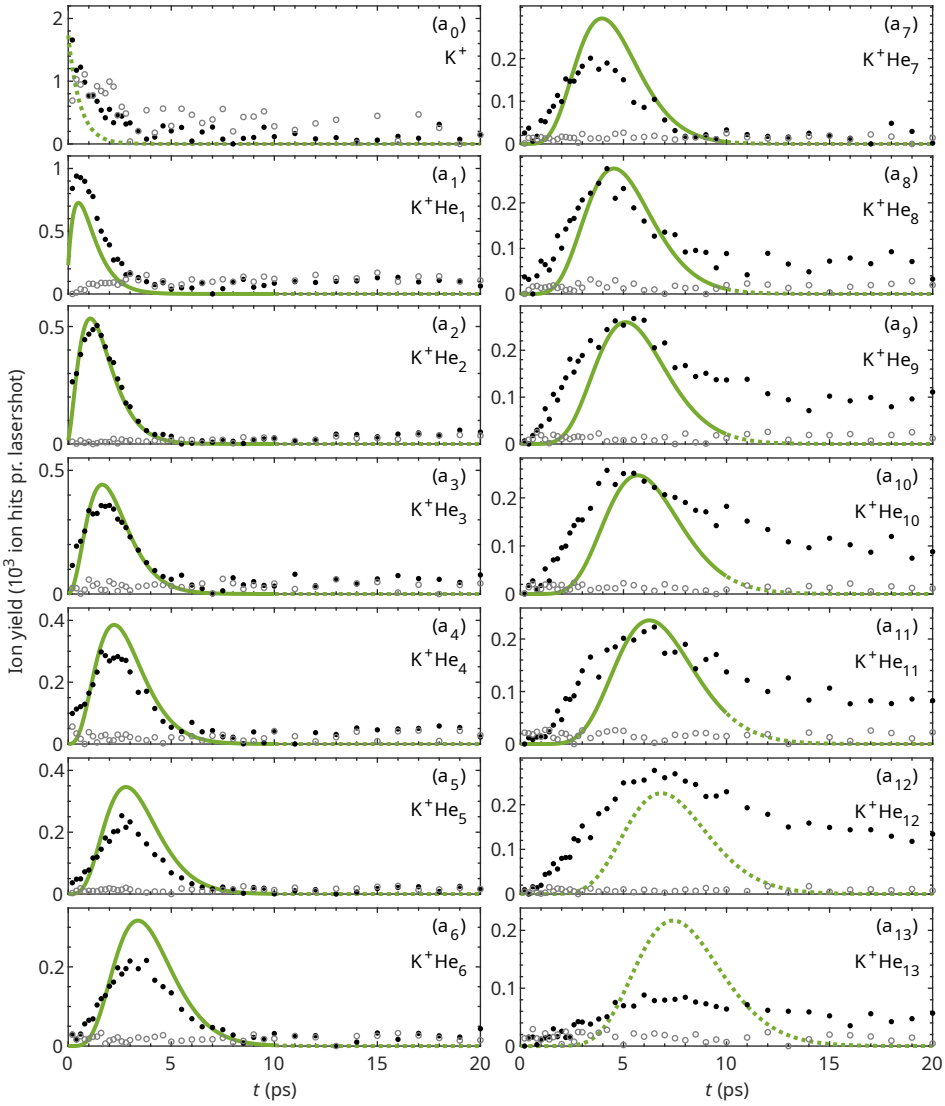

Figure 5.11: Experimental ion yields $Y_n(t)$ of K^+He_n as a function of pump-probe delay, t, for a selected range of n. Black dots represent the ion yields identified as coming from the $Xe^+ - K^+He_n$ repulsion, while gray circles represent a repetition of the experiment without Xe doping. The solid green lines are a Poisson fit to the data, Eq. (5.3), with dashed green lines representing extrapolating this fit beyond the fitted range.

$n = 12$ to $n = 13$. The lacking correspondence between the Poisson model and the data is also clearly seen, especially at later times, which will be discussed in Section 5.7.5. Finally, a significant portion of the distribution seems to fall out of the recorded $n = 0 - 21$ range already at about $t \geq 4\,\text{ps}$. In this range of times, the upper and lower bounds of $\langle E_{\text{disp}} \rangle (t)$ can be determined using Eq. (5.11), with the result shown in Fig. 5.13. $E_{\text{dimple}}(\text{K}^+) = 11.7\,\text{meV}$ was found based on the values published in reference [40][5]. While the overall shape of $\langle E_{\text{disp}} \rangle (t)$ looks similar to that for Na^+ solvation, it deviates strongly from the exponential model written in Eq. (5.12) in the trusted time-range, which makes extracting a reasonable τ_{disp} by fitting impossible.

One major error in the determination in $\langle E_{\text{disp}} \rangle (t)$ is the previously discussed contamination in the $n = 0$ ion yield, $Y_0(t)$, which will artificially lower $\langle E_{\text{disp}} \rangle (t)$. The effect is most prominent in the first few ps, where the overestimation of $Y_0(t)$ is worst, see Fig. 5.11(a_0). This corresponds well with the slight upwards kink of $\langle E_{\text{disp}} \rangle (t)$ during the first few ps, seen in Fig. 5.13. This is one possible explanation of the deviation of $\langle E_{\text{disp}} \rangle (t)$ from the expected exponential shape, but without a repeat of the experiment which eliminates the contamination, we cannot know for sure. The found $\langle E_{\text{disp}} \rangle (t)$ will be compared to the results for Na^+ and Li^+ solvation in Section 5.7.5.

5.7.3 Lithium - Experimental details

The experiment on lithium ion solvation is conducted in the same way as the sodium and potassium experiments, and the experimental details are virtually identical to the ones described in Section 5.3 and Section 5.7.1. Therefore, only the final experimentally critical parameters will be given in this section.

The droplet beam had an average droplet size of $\langle N \rangle = 5200$ atoms (18 K nozzle, 5 µm orifice, 50 bar backing pressure). The droplets were doped with Xe atoms and Li atoms (400 °C oven temperature), experimentally optimized for doping with just one Xe atom and one Li atom in each droplet. The laser system used was the $f_{\text{rep}} = 1\,\text{kHz}$ Spitfire Ace, see Section 3.4. The pump pulse used was polarized in the detector plane, had a central wavelength of $\lambda = 400\,\text{nm}$, and a peak intensity of $I_0 = 2.6 \times 10^{13}\,\text{W/cm}^2$ ($\tau_{\text{FWHM}} = 100\,\text{fs}$, $w_0 = 24\,\mu\text{m}$, $P_{\text{avg}} = 25\,\text{mW}$). The probe pulse was polarized in the detector plane, had a central wavelength of $\lambda = 800\,\text{nm}$, and a peak intensity of $I_0 = 1.2 \times 10^{14}\,\text{W/cm}^2$ ($\tau_{\text{FWHM}} = 63\,\text{fs}$,

[5] Using the notation of the reference $E_{\text{dimple}}(\text{K}^+) = S_{\text{K}^+} + E_{\text{sink}}(K^+)$, where S_{K^+} and $E_{\text{sink}}(K^+)$ are given in the paper.

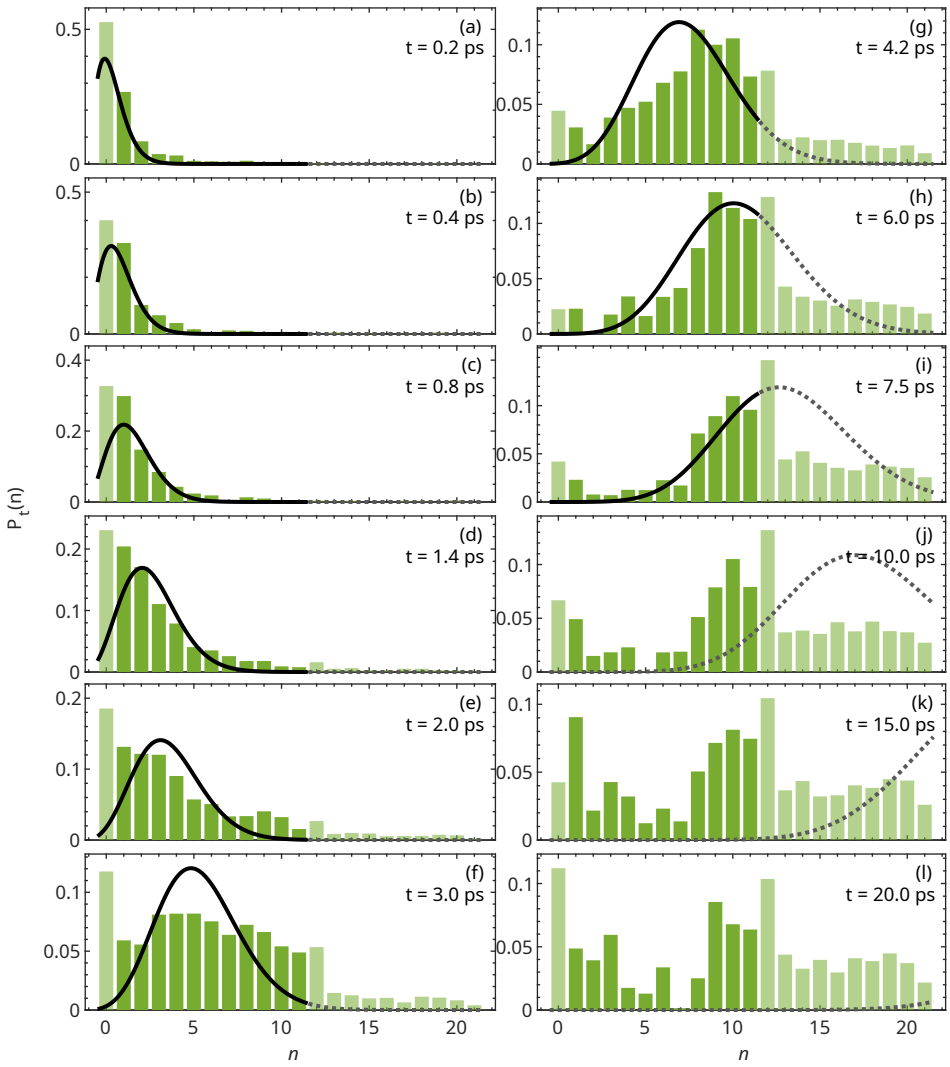

Figure 5.12: Distribution of detected K^+He_n complexes, $P_t(n)$, for the full measurement range of $n = 0-21$, and select pump-probe delays, t. Dark green bars signify the range used for the Poisson attachment model fit. Full black lines show the fitted curve, see Eq. (5.3),while the dashed gray lines show an extrapolation of the fitting function beyond the fitted range.

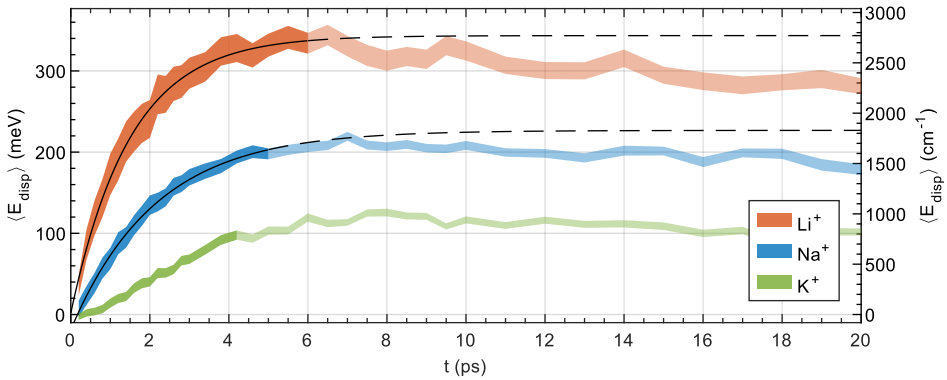

Figure 5.13: Upper and lower bounds of $E_{\mathrm{disp}}(t)$, for Li^+, Na^+ and K^+ solvated in helium droplets. The dark-colored regions represent the range of t where E_{disp} is expected to be well estimated. The black solid lines are exponential fits to this region, see Eq. (5.12), while the black dashed lines are extrapolations of the fitting function beyond this range.

$w_0 = 21\,\mu\mathrm{m}$, $P_{\mathrm{avg}} = 25\,\mathrm{mW}$). The pump-probe delay was varied between $t = 0.2\,\mathrm{ps}$, to avoid the temporal overlap of the pump and probe pulse, and $t = 20\,\mathrm{ps}$. The VMI spectrometer was operated with the voltages $V_R = 6000\,\mathrm{V}$, $V_E = 3833\,\mathrm{V}$ and $V_G = 0\,\mathrm{V}$. The chevron type MCP and phosphor screen was used with the voltages $V_F = -600\,\mathrm{V}$, $V_B = 1200\,\mathrm{V}$ and $V_{ph} = 4200\,\mathrm{V}$. The resulting spots of light on the phosphor screen from ion hits were recorded with the Tpx3CAM, and after the standard post-processing of time-walk correction, clustering, centroiding, second time-walk correction and TOF-to-m/q calibration, the resulting data was a list of ion hits, with the m/q, v_x, v_y, laser shot number and t recorded for each ion hit.

5.7.4 Lithium - Results

The data was analyzed exactly as for the sodium- and potassium-solvation experiments, dividing the data into different n, number of helium attached, to $^7Li^+$, the most prevalent isotope[6]. The Li^+He_n complexes can be recorded in the range $n = 0 - 29$, as Li^+He_{30} with $m/q = 127\,\mathrm{u\,e^{-1}}$ overlaps in the m/q spectrum with the Xe^+ isotopes. As with the sodium and potassium experiments, the distributions of velocity magnitudes were found for each t step by MEVIR image reconstruction [31], and the background ion signal was minimized by only integrating over

[6]The abundance of ^{7}Li is 92.4%, while that of ^{6}Li is 7.6% [29]

an appropriate range of this speed distribution. The resulting ion yields $Y_n(t)$ for $n = 0-13$ are shown in Fig. 5.14. Unlike the sodium and potassium experiments, the lithium experiment was not repeated without xenon doping, which should ideally be done when the experiment is repeated.

A Poisson model fit, see Eq. (5.3), was once again applied to the found $Y_n(t)$. As is shown in Fig. 5.5, however, $E_{\text{evap}}(N)$ drops off sharply for Li^+ already for $n > 3$, and for this reason, the fit is restricted to the range $n = 0-3$. This is a narrow range, but the effect of dissociation can be seen clearly for $n \geq 4$ in Fig. 5.14, where $Y_n(t)$ are smeared out and have different peak heights, compared to the Poisson model shown. The helium attachment rate obtained from the fit was $\lambda_{\text{He}} = 1.8$ helium atoms pr. ps.

The n-distribution at selected times is shown in Fig. 5.15. In the figure, a drastic pileup in the range $n = 4-6$ is seen, especially in $n = 6$. This corresponds to a steep dropoff in $E_{\text{evap}}(N)$, see Fig. 5.5. Thereby, the main features of the distribution are well explained by the same dissociation mechanisms as have been discussed for the sodium and potassium solvation experiments.

Finally, from $P_t(n)$ and $E_{\text{evap}}(n)$ the range of $E_{\text{disp}}(t)$ is found, see Fig. 5.13. $E_{\text{dimple}} = 15.6\,\text{meV}$ was once again estimated from the values in reference [40]. From the data presented in Fig. 5.15, it is estimated that all the Li^+He_n complexes fall within the measured range of $n = 0-29$ for the time range $t = 0.2\,\text{ps}$ to $6\,\text{ps}$. For this range, the $\langle E_{\text{disp}} \rangle$ follow an exponential shape very well, which is seen by the great quality of the fit shown in Fig. 5.13. From this fit, the dissipation timescale of $\tau_{\text{disp}} = 1.50\,\text{ps}$ is found. $\langle E_{\text{disp}} \rangle$ reaches about 320 meV at its maximum, about half of the 619 meV total solvation energy predicted in reference [40].

5.7.5 Comparison of Na^+, K^+ and Li^+ results

When comparing the sodium, potassium and lithium solvation experiments, it is clear that the experiments all measure the initial solvation dynamics of alkali ions on the surfaces of helium droplets. By comparing the results of the three different ions, we can learn more about the solvation process in general.

Firstly, the attachment rate of helium within the Poisson model is very similar for the three alkali ions, see Table 5.1. Within the uncertainty of the experiment, it is believed that these values are identical. This might be unexpected, due to the different pair potentials and evaporation energies of the alkali ions. Lithium, for instance, has a stronger pair potential than sodium and potassium, and could therefore be thought to couple more strongly to the droplet. However, the same

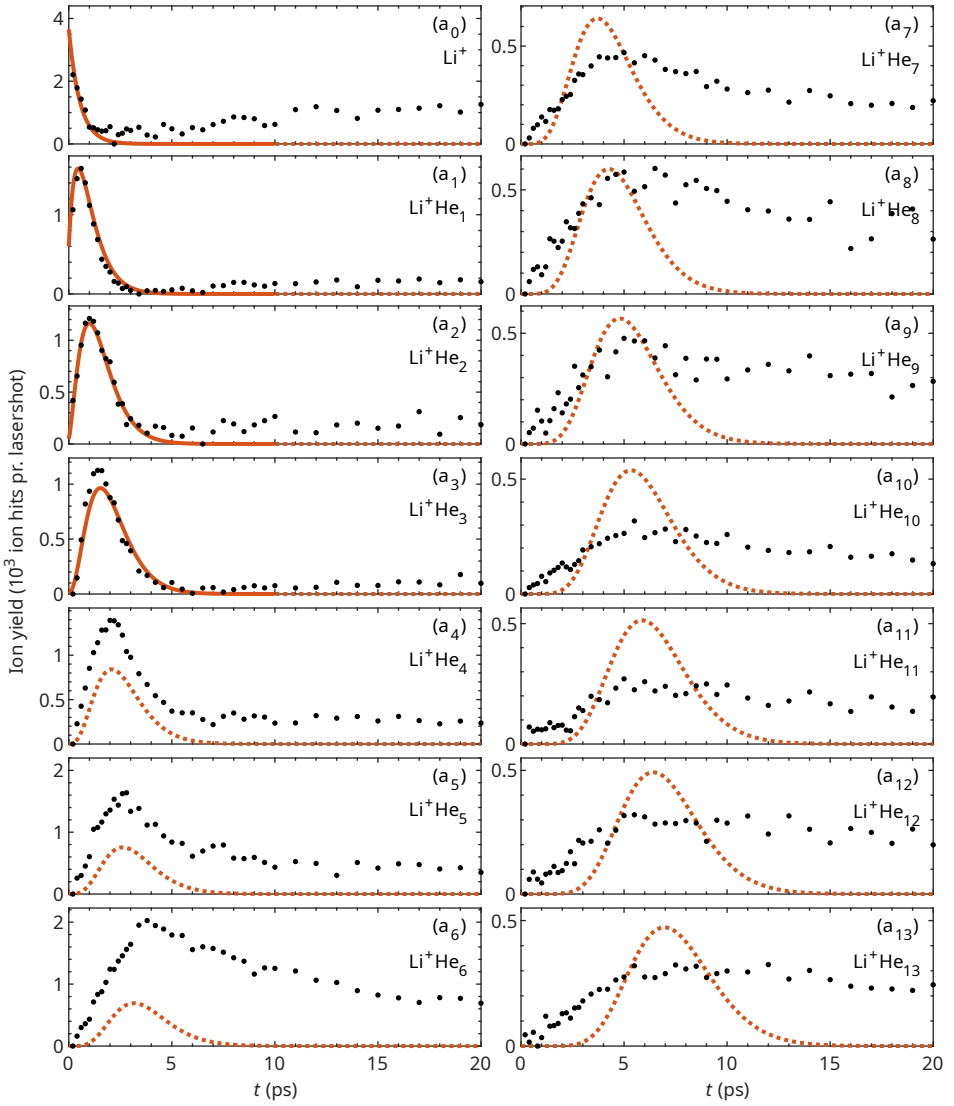

Figure 5.14: Experimental ion yields $Y_n(t)$ of Li^+He_n as a function of pump-probe delay, t, for a selected range of n. Black dots represent the ion yields identifies as coming from the Xe^+ – Li^+He_n repulsion, while gray circles represent a repetition of the experiment without Xe doping. The solid red lines are a Poisson fit to the data, Eq. (5.3), with dashed red lines representing extrapolating this fit beyond the fitted range.

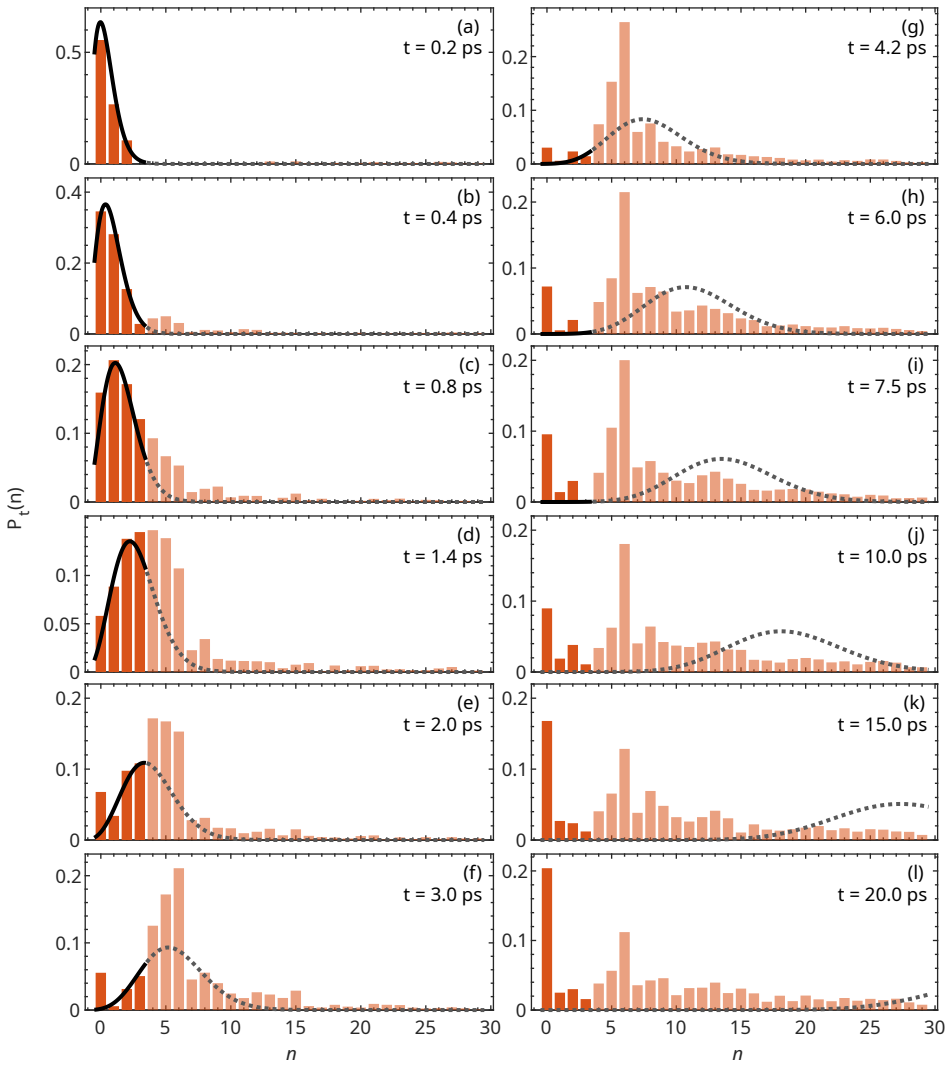

Figure 5.15: Distribution of detected Li^+He_n complexes, $P_t(n)$, for the full measurement range of $n = 0-29$, and select pump-probe delays, t. Dark red bars signify the range used for the Poisson attachment model fit. Full black lines show the fitted curve, see Eq. (5.3),while the dashed gray lines show an extrapolation of the fitting function beyond the fitted range.

Alkali	λ_{He} (He/ps)	τ_{disp} (ps)
Na^+	1.8	2.14
K^+	1.7	N/A
Li^+	1.8	1.50

Table 5.1: Comparison of the key results of the three solvation experiments, that is solvation of Na^+, K^+ and Li^+ ions, the helium attachment rate, λ_{He}, and the dissipation timescale τ_{disp}. In all experiments, droplets with an average size of $\langle N_{\mathrm{He}} \rangle = 5200$ atoms were used.

stronger pair potential also means that it needs to dissipate more energy to the droplet to create the Li^+–He bonds. One explanation of why all the helium attachment rates are essentially the same could be that these two effects, the stronger coupling and the higher bond energy, cancel out.

Secondly, while the shape of $\langle E_{\mathrm{disp}} \rangle (t)$ is very similar between the three alkalis, the dissipation time scales, collected in Table 5.1, do differ slightly. The Li^+ experiment finds a slightly faster energy dissipation than the Na^+ experiment. While the K^+ experiment does not correspond well to the model, Fig. 5.13 suggests that $\langle E_{\mathrm{disp}} \rangle (t)$ for the K^+ experiment is slightly slower than that of the Na^+ experiment. This follows the trend of the Ak^+–He pair potential, and thereby the coupling between the Ak^+ ion and the droplet, getting weaker the heavier the alkali.

Thirdly, the $P_t(n)$ distributions of measured helium complex sizes for the different alkalis, shown in Fig. 5.9, Fig. 5.12 and Fig. 5.15, clearly reflect the energetic structure of the Ak^+He_n complexes. For the lithium experiment, the very sharp dropoff of E_{evap} shown in Fig. 5.5 corresponds to the pileup in the $n = 4-6$ range, especially in $n = 6$, seen in Fig. 5.15. For Na^+ the sharpest E_{evap} dropoffs occur from $n = 6$ and $n = 9$, and correspondingly, $n = 6$ and $n = 9$ show a pileup in Fig. 5.9. Finally, E_{evap} is much flatter for K^+ ions than for the other alkalis used, with the only significant dropoff being from $n = 12$. $n = 12$ also corresponds to a clear edge in $P_t(n)$ for K^+, as shown in Fig. 5.12. One major difference between the Li^+ and Na^+ results and the K^+ results is that for Li^+ and Na^+, $P_t(n)$ corresponds well with a Poisson distribution up to the first E_{evap} dropoff, while the correspondence is less good for K^+. This can be explained by the fact that the absolute E_{evap} is smaller for K^+ than for Li^+ and Na^+, leading to a higher likelihood of dissociation following the ejection of the Ak^+He_N complexes from the droplet surface. In conclusion, the features of $P_t(n)$ are well explained by a baseline Poisson distribution modified by dissociation effects with features corresponding

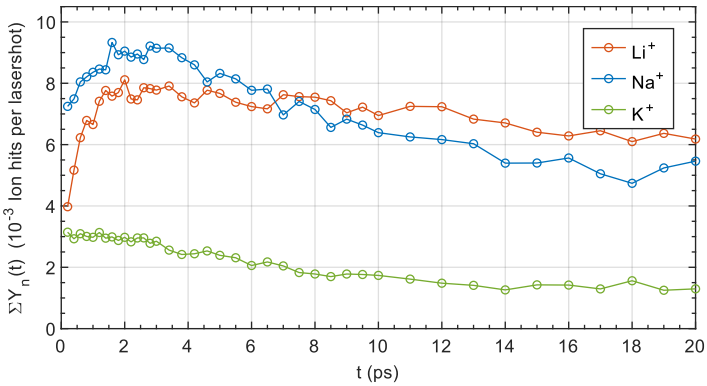

Figure 5.16: Sum of all detected ion yields, $Y_n(t)$, for the three solvation experiments: Na^+, K^+ and Li^+.

to the features of $E_{\text{evap}}(N)$.

5.8 Discussion

5.8.1 Validity of models

Poisson model The Poisson model for the ion yields fit the experimental data well for Na^+ and Li^+, and less well for K^+. The disagreement of the K^+ data can however be explained by a comparatively stronger effect of post-ejection dissociation, due to the lower evaporation energy of K^+, as discussed above. Within this limitation, this points to the attachment of the first few helium atoms truly following a Poisson-like process for all three ions, and gives validity to the found helium attachment rates.

Energy dissipation The exponential model fits the Li^+ and Na^+ energy dissipation results very well, and the deviation of the K^+ can be explained by an overestimation of the $n = 0$ signal, as discussed above. However, the final dissipated energy is significantly lower than expected. When comparing with the solvation energies given in reference [40], the measured energies are about half of what was expected. However, to measure the full solvation energy, we should also measure an n distribution that is dominated by very large complexes. This is not the case, rather, the n distributions seem to reach a final distribution. This distribution is probably the result of having a mostly fully relaxed solvation complex on the

droplet surface being repelled by the Xe^+ ion. The most loosely bound helium atoms are thereby probably kicked off by repulsion-induced dissociation. In other words, this experiment is not very sensitive to the most loosely bound helium atoms. It seems that the experiment is able to measure the dissipated energy for the first steps of the ion solvation process.

5.8.2 Comparison with TDDFT

Comparing the experimental results to the TDDFT calculations are complicated by the fact that the TDDFT calculation do not include the probe process of the experiment. Instead, we quantify the number of helium atoms that are within the first and second solvation shells by integrating over the appropriate volumes of helium density found by the TDDFT calculation. As discussed in Section 5.1.4, for sodium ions, this build-up rate of helium atoms in the first solvation in the TDDFT simulation was found to be 1.6 He/ps, while the build-up rate of helium atoms in the first and second solvation shell was found to be 3.1 He/ps. The experimentally found rate of 1.8 He/ps for sodium is between these two values, which indicates that the probe process of the experiment addresses all of the first solvation shell and some of the second solvation shell.

For comparison with the lithium and potassium results, the TDDFT simulation helium build-up rates in the first solvation shell have been reported in reference [40]. These rates are 1.5 He/ps for Li^+, 0.8 He/ps for Na^+, and 0.6 He/ps K^+. For Li^+ and K^+ these rates are lower than the experimentally found helium attachment rates, once again consistent with the interpretation that the probe process addresses all of the first solvation shell and some of the second solvation shell.

5.9 Conclusion

A novel experimental technique for measuring the solvation dynamics of single alkali ions introduced into a liquid has been realized. The technique measures how the distribution of the number of attached helium atoms, $P_t(n)$, changes as a function of the time after the alkali ion was introduced to the droplet.

The ion yields of the Ak^+He_n complex $Y_n(t)$ has been shown to follow a Poisson model with a constant rate helium attachment events, λ_{He}, for the range of n where the dissociation of probability of Ak^+He_n complexes is minimized. Fitting the experimental results to this model yields an estimate of λ_{He}, which is found to be 1.8 He/ps for Na^+ solvation, 1.7 He/ps for K^+ solvation and 1.8 He/ps for K^+

solvation. The deviations from this model are well predicted by the n dependence of the ab-initio calculated evaporation energies $E_{\mathrm{evap}}(n)$.

Based on a series of assumptions justified by molecular dynamics simulations of the system, the binding energy from the $\mathrm{Ak}^{+}\mathrm{He}_n$ complexes dissipated into the droplets can be estimated from the distribution of complex sizes $P_t(n)$, the mean of which is $\langle E_{\mathrm{disp}} \rangle (t)$. The shape of $\langle E_{\mathrm{disp}} \rangle (t)$ is exponential, as would be expected of the time evolution of the energy during the transfer of heat from one macroscopic body to another. The mean dissipation time, τ_{disp} has been found to be 2.14 ps for Na^{+} solvation and 1.50 ps for Li^{+} solvation, while the K^{+} solvation was too contaminated by background signal to accurately determine τ_{disp}.

CHAPTER 6

Measuring Co-Dopant Distances

In this chapter, I will explore how to measure the distance between surface bound (alkali) and inside bound (closed shell systems) dopants in helium droplets. This will be done using laser-induced Coulomb Explosion Imaging (CEI) however, in some ways complicated by the presence of the helium droplet. The principle of the method will be illustrated by experiments on droplets co-doped with a potassium (K) atom and a xenon (Xe) atom. These results are important because they provide information about the size of the helium droplets and the position of the inside dopant (Xe). Furthermore, they enable the study of droplet size dependent effects in time dynamic measurement, like the solvation measurements, as will be discussed in Chapter 7. The work covered in this chapter has not yet been published at the time of writing.

6.1 Principle of the experiment

The principle of the experiment is sketched in Fig. 6.1. Helium droplets are doped with a potassium (K) atom and a xenon (Xe) atom, with the K atom bound on the surface and the Xe atom inside the droplet, see Section 2.5. The dopants are ionized by an intense femtosecond laser pulse, which is able to ionize K (ionization potential (IP) of 4.34 eV [60]) and Xe (IP of 12.13 eV [60]) atoms, but not He atoms (IP of 24.59 eV), by non-resonant multi-photon ionization. After this, both ions suddenly feel a strong electrostatic repulsion, and the K^+ ion is thereby repelled

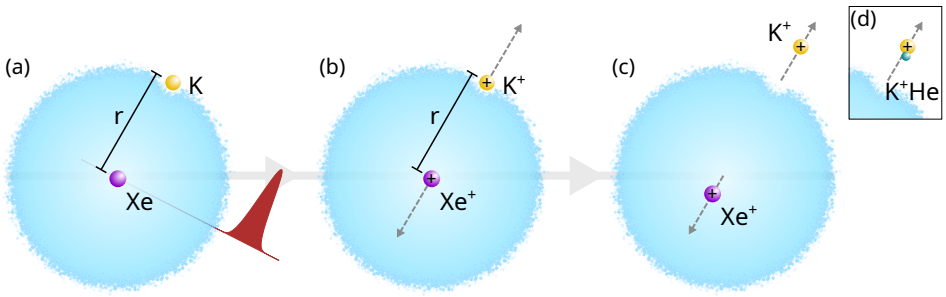

Figure 6.1: Principle of the experiment. (a) A helium droplet co-doped with an alkali (potassium) and a closed shell system (xenon), separated by a distance r. (b) Both dopants are simultaneously ionized by a femtosecond laser pulse. (c) The resulting repulsion repels the alkali ion from the droplet, leading to a certain kinetic energy of the alkali ion, which is measured. (d) One or more helium atoms could attach to the alkali ion on the way from the droplet.

from the droplet surface. The closer the ions initially are, the more kinetic energy the K^+ ions will get, and by measuring this kinetic energy, E_{kin,K^+}, we should be able to reconstruct the initial distance, r, between them. In fact by measuring the kinetic energy *distribution*, $P(E_{\mathrm{kin},K^+})$, we should be able to find the full Xe–K distance *distribution*, $P(r)$. Although the exact location of the Xe atom inside is not well characterized, it is expected that changing the droplet size will shift $P(r)$.

This is an example of *Coulomb Explosion Imaging* (CEI), the general experimental technique of determining the structure of a system by multiply ionizing the system, measuring the kinetic energies and emission directions of the resulting ions, and deducing the original structure based on this measurement [106, 116, 119]. It is paramount that the system in question does not have time to rearrange during the ionization process. For this reason, the systems are often ionized by femtosecond laser pulses, ensuring that the ionization happens within tens of femtoseconds. The method of deducing the structure of the original system differs according to the complexity of the system. Polyatomic molecules can be either partially or totally Coulomb exploded, and the momentum of all resulting ions can be measured in the molecular frame [75]. If more than a few ions are created, however, determining the structure of the molecules based on the measured momenta becomes very complicated and in many cases impossible. The work in this chapter, and in this thesis in general, is however only concerned with measuring the structure

of atomic and molecular dimers. More specifically, we are interested in finding the distance between the two components, discarding any potential orientation. In this case, only the pair potential of the two created ions is needed. While a simple Coulomb potential is not sufficient for all dimers at equilibrium distance [102], the Coulomb approximation becomes better at larger distances[1], and we assume that it is sufficient for the large separation, multiple nm, between the alkali ion and the counter ion in this experiment.

The presence of the helium droplet is of course the foundation of the experiment, but it also complicates the CEI technique. The droplet seems to trap the Xe^+ ion, and we thereby have to deduce the total kinetic energy released only from the K^+ kinetic energy. Furthermore, Chapter 5 clearly shows that alkali ions will attach helium atoms on the surface of droplets, which spreads the signal over multiple ion mass channels, K^+He_n. The techniques and tricks for circumventing these challenges will be discussed in the following sections.

The droplets provide a very interesting parameter to vary, namely the *average droplet size*, which is controlled by the temperature of the droplet creation nozzle. As explained in Section 2.4, the average number of atoms, $\langle N \rangle$, in, or equivalently the average hard-sphere radius, $\langle R_D \rangle$, of, the droplets is only approximately known for each nozzle temperature. For this reason, this chapter will keep the results in terms of nozzle temperature, and later compared to expected droplet sizes.

6.2 Experimental details

The technical details of the experimental setup have already been explained in Chapter 3. This section will give a brief explanation of the experimental details of this specific experiment, with a specific focus on documenting all the experimental parameters used.

Droplet doping

The droplets were created by expanding cold, high pressure, high purity (99.9999%) helium gas through a 5 µm round orifice. The stagnation pressure of helium was kept at 50 bar. The average size of the created droplets was controlled by controlling the temperature of the nozzle. A nozzle temperature in the range 14 K to 22 K was

[1] Consider the multipole expansion of an arbitrary pair potential, at large distances the monopole term is dominant [46].

used for this specific experiment, corresponding to a range of sizes from 13000 to 1200 atoms, or hard-sphere droplet radii in the range 5.22 nm to 2.36 nm (See also Table 2.1).

The droplets pass though a skimmer into the doping chamber, where they pass through two doping cells. The *first* cell the droplets reach is the gas cell, a tube connected by a gas line to a leak valve, behind which the sample is put. For this experiment, the gas dopant used was pure Xenon (99.99%, Messer CANGas brand), regulated to 0.7 bar behind the leak valve, with the doping pressure in the gas cell controlled by controlling the opening of the leak valve. The *second* doping cell is an oven that is kept at a specific temperature, thereby regulating the vapor pressure of the pure potassium (K) metal. For the presented experiment, an oven temperature of 70 °C was used. The doping pressures were not measured in the experiment, but appropriate leak valve opening and oven temperature was found by optimizing the $Xe^+ - K^+$ Coulomb explosion signal, as explained later. Due to the Poissonian pickup statistics described in Section 2.5, the droplets will contain several different combinations of K and Xe dopants, with the most probable hopefully being one K and one Xe. However, as will be evident in Section 6.3, K_2 doped droplets will inevitably also contribute significantly to the signal.

Laser setup and ionization

The doped droplets fly into the "target" vacuum chamber, where they enter the VMI spectrometer. In the middle of the VMI spectrometer the droplet beam is crossed by the laser beam. For this experiment, the 5 kHz laser system (Coherent Astrella He USP) described in Section 3.4 was used. The experimental scheme, see Section 6.1, only requires a single laser pulse, and as such, the optical setup only included the necessary parts: A half-wave plate and a thin-film polarizer for power control, a BBO crystal for second harmonic generation, a second half-wave plate for polarization control, a lens to focus the beam into the vacuum chamber. In practice, however, this was realized simply by using only the "pump" arm (The one without delay stage) of the optical setup shown in Section 3.4. A BBO crystal (0.5 mm thickness, 22.4°) was used for second harmonic generation (SHG), in order to generate 400 nm light pulses. The reason for using this rather than 800 nm pulses, is that the 800 nm pulses dissociatively ionize the K_2 dimers, leading to K^+ kinetic energy channels that overlap with the wanted $Xe^+ - K^+$ kinetic energy channels, similar to what was discussed in Section 5.3.

The 400 nm pulse had a measured pulse energy of $E_p = 26.0\,\mu J$ ($P_{avg} = 130\,mW$

average power at a repetition rate of $f_{rep} = 5\,\text{kHz}$), a measured focused beam radius of $w_0 = 15.5\,\mu\text{m}$, and an estimated FWHM pulse length of $\tau_p = 51\,\text{fs}$[2]. This gives a peak intensity, I_{peak} of $1.7 \times 10^{14}\,\text{W/cm}^2$, see Eq. (3.6) in Chapter 3.

Ion detection

As the doped droplets cross the laser beam, the dopants are ionized, see Section 6.1. This leads to the creation of ions, for which we need to measure the kinetic energies. As described in Section 3.5, the Velocity Map Imaging (VMI) spectrometer projects the 3D velocity distribution onto the 2D detector. The electrode voltages were set to VMI focus (specifically $V_\text{E} = 6000\,\text{V}$, $V_\text{R} = 3810\,\text{V}$, and $V_\text{G} = 0\,\text{V}$). The detector was the chevron-type MCP (Voltages used: $V_\text{F} = -600\,\text{V}$, $V_\text{B} = 1200\,\text{V}$, and $V_\text{phos} = 4200\,\text{V}$). The TPX3Cam was used to record the ion events based on the spots of light on the phosphor screen, as described in Section 3.5.

After clustering and centroiding, see Section 4.1, the data of the experiment to be further analyzed is a list of ion detection events, recording the laser shot number, time of flight (TOF), and x and y detector coordinate of each event. The recorded TOFs are converted into mass-over-charge (m/q) ratios, and the events corresponding to the m/q of K^+ and K^+He_n accumulated into 2D histograms of x and y detector coordinates, resulting in VMI images, which are further analyzed as explained below.

6.3 Bare alkali ions

In this section, we will treat and interpret the measurement of the K–Xe distance, based on the kinetic energy distribution of K^+ ions.

6.3.1 Kinetic energy distributions from VMI images

As explained in the previous sections, we want to find the kinetic energy distribution, $P(E_\text{kin})$, of K^+ ions originating from the Coulomb explosion of K^+ and Xe^+ from the droplets. This is done by recording Velocity Map Imaging (VMI) images, see Section 3.5 in Chapter 3 for further details on the VMI technique. VMI images of K^+ ions for a range of different droplet temperatures are shown in Fig. 6.2. The

[2]Based on the cross correlation between the 800 nm probe arm and the 400 nm pump arm on the H_2O^+ ion signal (τ^{CC}_FWHM =65 fs), and the probe pulse length of $\tau_{probe} = 41\,\text{fs}$ measured by autocorrelation.

calibration from (x,y) to (v_x,v_y) was done by restricting the kinetic energy of the K^+ ion Coulomb explosion channel of $^3\Sigma_u^+$ state K_2 dimers to the value 1.25 eV reported in reference [62].

Here multiple channels are seen: Firstly, the outer ring in the images does not change size with the different droplet sizes, and is identified as the Coulomb explosion channel of K_2 dimers that were initially in the triplet ($^3\Sigma_u^+$) state. This is also corroborated by the angular and radial covariance of the ion counts found in the region of this channel, which is not shown here, but indicates that two K^+ ions axially recoil. For an introduction to this covariance, see Section 8.4.2 in Chapter 8. Secondly, in the center of the image, a low energy channel is seen. This is interpreted as K^+ coming from dissociative ionization of the K_2 dimers, or from desorption following ionization of droplet bound K monomers. Thirdly, a channel is seen between these two rings, which changes radius slightly with different droplet sizes. This is interpreted as K^+ ions being repelled from the droplet by their companion Xe^+ ions, as described in Section 6.1, and is the channel of interest in the experiment. Finally, a black bar is seen in each image, which is a mask imposed on the images to block out the very intense line of signal coming from the ionization of *effusive* K atoms from the doping chamber. The origin of this channel is further explained in Section 3.3.

As explained in Chapter 3.5, the VMI images are 2D projections of the initial ion velocities. Due to the ionization mechanism, the 3D velocity distribution must be cylindrical symmetric around the laser polarization axis. As the symmetry axis is experimentally set to lie in the detector plane, the two free dimensions of the initial velocity distributions can be recovered from the two free dimensions of the VMI image. For this work, the Polar Onion Peeling (POP) reconstruction technique was used, see Section 4.3.

The needed result of the image reconstruction is the detector radius distribution of the ion counts, which we will call $P(r_d)$, r_d being the detector radius in units of pixels. This intermediate result is not shown here, as it is immediately transformed into the kinetic energy distribution. As explained in Section 3.5 in Chapter 3, the relation between the detector radius and the kinetic energy is given as:

$$E_{\text{kin}} = k_{\text{VMI}} \cdot r_d^2, \tag{6.1}$$

where the calibration factor k was obtained by fitting to the Coulomb explosion channel of K_2 dimers in the triplet ($^3\Sigma_u^+$) state, as mentioned before. When doing a coordinate transformation, like $y = y(x)$, the probability density functions of the

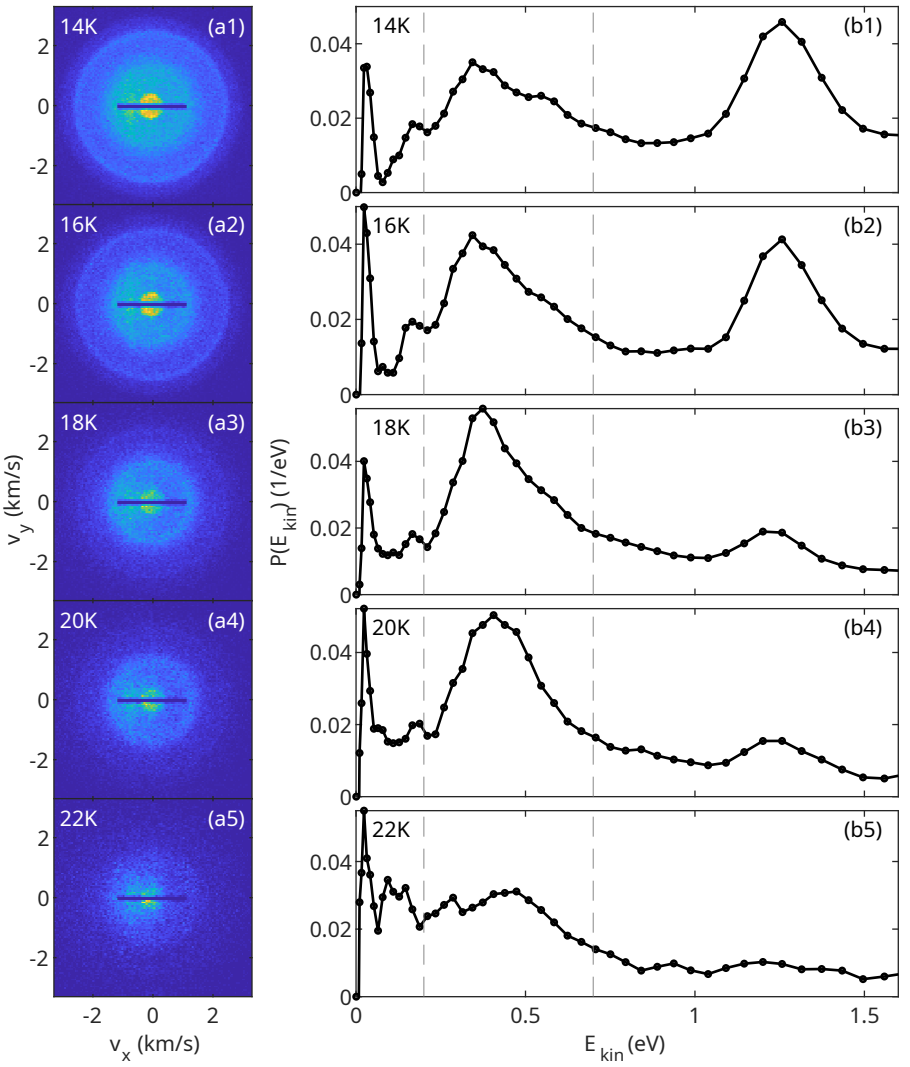

Figure 6.2: (a1)-(a5) VMI images of K^+ for several droplet sizes, expressed as droplet nozzle temperatures. (b1)-(b5) Corresponding E_{kin} distributions extracted from Abel inversions of the data.

two variables are related by [52],

$$P(y) = \left|\frac{dx}{dy}\right| P(x(y)), \tag{6.2}$$

see Section A.2. So to find $P(E_{\text{kin}})$ from $P(r_d)$, we need

$$r_d = \sqrt{\frac{E_{\text{kin}}}{k_{\text{VMI}}}}, \qquad \text{and} \qquad \frac{dr_d}{dE_{\text{kin}}} = \frac{1}{2k_{\text{VMI}}\sqrt{E_{\text{kin}}/k_{\text{VMI}}}}. \tag{6.3}$$

Thereby, the kinetic energy distribution function must be

$$P(E_{\text{kin}}) = \frac{1}{2k_{\text{VMI}}\sqrt{E_{\text{kin}}/k_{\text{VMI}}}} P\left(r_d(E_{\text{kin}})\right). \tag{6.4}$$

Thereby, the kinetic energy distributions in Fig. 6.2 were found.

The kinetic energy distributions $P(E_{\text{kin}})$ show the same three major features that were described for the VMI images: The K_2 triplet ($^3\Sigma_u^+$) Coulomb explosion channel located at 1.25 eV, the inner dissociative ionization or monomer channel located at below 0.1 eV, and finally the channel of interest, shifting with droplet size, but confined between 0.2 eV and 0.7 eV. In the next section, this distribution of kinetic energies will be converted to the distributions of distances between the K and Xe atoms, $P(r)$.

6.3.2 Converting energy distributions to distance distributions

To convert $P(E_{\text{kin}})$ to $P(r)$, we must first describe the physical process that gives the K^+ ions their kinetic energies.

In the Coulomb explosion process, the ions initially have no kinetic energy, E_{kin}, but they do have electrostatic potential energy from their internal repulsion, E_{pot}. At long times after the laser pulse, the ions have moved far enough apart that their electrostatic potential energy approaches zero, while they must now have some finite kinetic energy. Thereby the two energies can be equated, as

$$E_{\text{pot}}(t = 0) = E_{\text{kin}}(t \to \infty). \tag{6.5}$$

To calculate the initial potential energy, we consider the K^+ and Xe^+ to be point charges interacting according to the Coulomb potential. Thereby, the potential

energy must be given as

$$E_{\text{pot}} = \frac{1}{4\pi\varepsilon_0}\frac{q_1 q_2}{r}, \tag{6.6}$$

where ε_0 is the *vacuum permittivity*[3], q_1 and q_2 are the charges of the two ions, and r is the distance between them [46]. In this case, both of the ions have the charge $+e$. Note that this potential energy does not include the attractive interaction between the K^+ ion and the polarizable helium droplet, the effect of which will be discussed later.

The final kinetic energy must be the sum of the kinetic energies of the K^+ and Xe^+ ions,

$$E_{kin,tot} = E_{\text{kin},K^+} + E_{kin,Xe^+}, \tag{6.7}$$

however, we only measure the kinetic energy of K^+ in the experiment. As explained in section Section 6.3.1, the Xe^+ atoms do not seem to leave the droplets unhindered, and we do not detect them in coincidence with the K^+ ions. We can, however, estimate the ratio of the kinetic energy of the two ions. Suppose that both are free to repel, like they would be in the gas phase. Initially, the total momentum in their center-of-mass frame would be zero, and this must be conserved as they repel, leaving equal and opposite momentum for each. Thereby,

$$E_{kin,tot} = \frac{p_{K^+}^2}{2m_{K^+}} + \frac{p_{Xe^+}^2}{2m_{Xe^+}}, \qquad p_{K^+} + p_{Xe^+} = 0, \tag{6.8}$$

$$= \frac{(m_{Xe^+} + m_{K^+})p_{K^+}^2}{2m_{Xe^+}m_{K^+}} \tag{6.9}$$

$$\implies E_{kin,tot} = \frac{m_{Xe^+} + m_{K^+}}{m_{Xe^+}} E_{\text{kin},K^+}, \tag{6.10}$$

where p_{K^+} and p_{Xe^+} are the 1D momenta along the recoil axis, and m_{K^+} and m_{Xe^+} are the masses of the ions. m_{K^+} is set to 39 u, as we selectively detect the $^{39}K^+$ ions. We do, however, not know which Xe^+ isotope partook in any specific Coulomb explosion event, so the average atomic mass of naturally occurring Xe isotopes of 131.293 u [29] was used for m_{Xe^+}. In the physical system, the Xe^+ is

[3] Perhaps counterintuitively, the presence of the dielectric helium does not affect the interaction between the two charges because the alkali ion is always outside the surface of the droplet, see [46, Example 4.5].

probably not totally free, but rather somewhat trapped within the droplet, which in the above equation would correspond to a different effective mass. If the Xe^+ is totally stationary, this would correspond to an infinite effective mass, and thereby, according to Eq. (6.10), $E_{\mathrm{kin},K^+} = E_{kin,tot}$, the K^+ ion would take the total energy. It is uncertain what the effective mass of the Xe^+ ions should be set as, but it must lie between the two extremes of the bare ion mass and infinite mass. While this seems like a broad range, it corresponds to the K^+ ion getting between 76% and 100% of the total kinetic energy. In the following sections, results using both of these extremes will be shown where relevant. To mitigate the uncertainty of not knowing the effective Xe^+ mass, an improved experiment should use the lightest alkali with the heaviest counter ion available, as this combination would give the maximum energy to the measured alkali ion.

We now have the required equations to deduce the separation between the two ions, r. Combining equations 6.5, 6.6 and 6.10, we get

$$\frac{1}{4\pi\varepsilon_0}\frac{e^2}{r} = \frac{m_{Xe^+} + m_{K^+}}{m_{Xe^+}} E_{\mathrm{kin},K^+}, \tag{6.11}$$

$$\implies r = \frac{m_{Xe^+}}{m_{Xe^+} + m_{K^+}} \frac{e^2}{4\pi\varepsilon_0} \frac{1}{E_{kin,K^+}}. \tag{6.12}$$

Once again, we will use Eq. (6.2), now to transform $P(E_{\mathrm{kin}})$ into $P(r)$. Thereby, we need to find the inverse function of $r(E_{\mathrm{kin},K^+})$ and the derivative of the inverse function:

$$E_{\mathrm{kin},K^+}(r) = \frac{m_{Xe^+}}{m_{Xe^+} + m_{K^+}} \frac{e^2}{4\pi\varepsilon_0} \frac{1}{r}, \tag{6.13}$$

$$\frac{dE_{\mathrm{kin},K^+}}{dr} = -\frac{m_{Xe^+}}{m_{Xe^+} + m_{K^+}} \frac{e^2}{4\pi\varepsilon_0} \frac{1}{r^2}. \tag{6.14}$$

And finally, we arrive at the expression for the probability distribution of the distance between K and Xe,

$$P(r) = \frac{m_{Xe^+}}{m_{Xe^+} + m_{K^+}} \frac{e^2}{4\pi\varepsilon_0} \frac{1}{r^2} P\left(E_{\mathrm{kin},K^+}(r)\right). \tag{6.15}$$

In Fig. 6.3, the r distributions calculated by applying Eq. (6.15) to the E_{kin,K^+} distributions in Fig. 6.2 are shown. The $Xe^+ - K^+$ energy channel, seen between the dashed lines in Fig. 6.2(b1-b5), are unfortunately not as clear in the $P(r)$ distribution

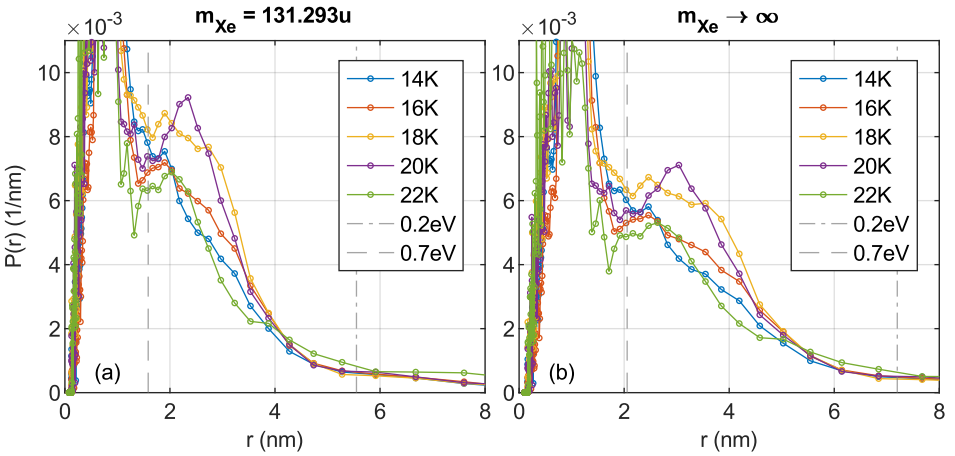

Figure 6.3: Distribution of Xe–K distances, r, for 5 different droplet sizes, represented by nozzle temperatures used to create them. (a) $P(r)$ based on free recoil of the Xe^+ and K^+. (b) $P(r)$ based on an infinite effective Xe^+ mass, see text for further details. Also marked with dashed and dash-dotted lines are the limits of the energy channel of interest, corresponding to the similar marking in Fig. 6.2.

seen in Fig. 6.3. This is believed to be due to the Jacobian transformation, Eq. (6.15), transforming the constant background signal into a $1/r^2$ shape, which drowns out the $Xe^+ - K^+$ channel. It is also clear that the uncertainty in the assignment of the effective mass of the Xe^+ ion does make a significant difference for the results. The 20 K data peaks at slightly larger r than the 22 K peak, as expected, see Section 2.4 in Chapter 2. Overall, the most probable r is approximately 2 nm or 3 nm, depending on the choice of effective Xe^+ mass. This is at least in the same order of magnitude as the expected droplet radii of 3.40 nm and 2.84 nm at 20 K and 22 K respectively, see Table 2.1. For lower nozzle temperatures (larger droplet sizes), the distributions shift towards higher r as expected, however, the magnitude of the shift is less than expected. And finally, the distributions are too contaminated by background to extract quantitative results about the widths of the distributions.

Overall, while the obtained result is comparable to the expected droplet radii R_D, the r distributions shown in Fig. 6.3 are disappointingly contaminated by background signal, and smaller r are apparently overrepresented in the results. This analysis does, however, not take all the possible signal into account. Namely, it is clear from Chapter 5 that the K^+ can bind He atoms, forming K^+He_n clusters. In

the next section, we will explore the signal from these clusters, and thereby attempt to reconstruct more accurate Xe – K distance distributions.

6.4 Helium-tagged alkali ions

As indicated in Fig. 6.1 panel (d), and analogous to the effects discussed in Chapter 5, the K^+ ion can bind one or more helium atom while being ejected by the droplet surface. This is due to the $K^+ - Xe^+$ repulsion being a relatively gentle Coulomb explosion, when comparing to the Coulomb explosion of the K_2 dimer, from which K^+He_n ions are not observed. Intuitively, the probability of attaching a He atom, like shown in Fig. 6.1 (d), must depend on how violently the K^+ is ejected from the droplet, and thereby on r. We would expect that the r distribution extracted from K^+ is suppressed for high r, and what is missing from the K^+ signal should be found in K^+He_n channels instead.

Experimentally, extracting the E_{kin} distribution for the different K^+He_n is a straightforward extension of the results presented so far. The same data analysis is simply repeated, selecting the ToF mass spectrum peaks at the masses[4]

$$m_{K^+He_n} = 39\,\text{u} + n \cdot 4\,\text{u}. \tag{6.16}$$

The data in these peaks are binned into VMI images, reconstructed using POP image inversion, see Section 4.3, and calibrated to retrieve the kinetic energy distributions. Like discussed in Section 3.5, for the energy calibration relation, $E_{\text{kin}} = k_{\text{VMI}} r_d^2$, where E_{kin} is the kinetic energy of an ion, r is the radial detector coordinate, the calibration factor k_{VMI} is independent of the mass of the ion in question.

The resulting E_{kin} distributions are shown in Fig. 6.4. Two important trends are seen:

Firstly, for the smaller the droplet (higher nozzle temperatures) the larger K^+He_n complexes are suppressed. For the 22 K droplets, barely any $Xe^+ - K^+He_n$ Coulomb explosion channels are seen for $n > 0$, while for 20 K barely any channel is seen for $n > 3$. Meanwhile, for the larger droplets, 14 K and 16 K, the channel is observed all the way up to $n = 11$, where it starts strongly overlapping with another energy channel. This channel, which is also seen in the $n = 9$ and $n = 10$ E_{kin} distributions, is interpreted as coming from doubly ionized Xe^{2+} ions and

[4]Here using the ^{39}K isotope, which is the most prevalent.

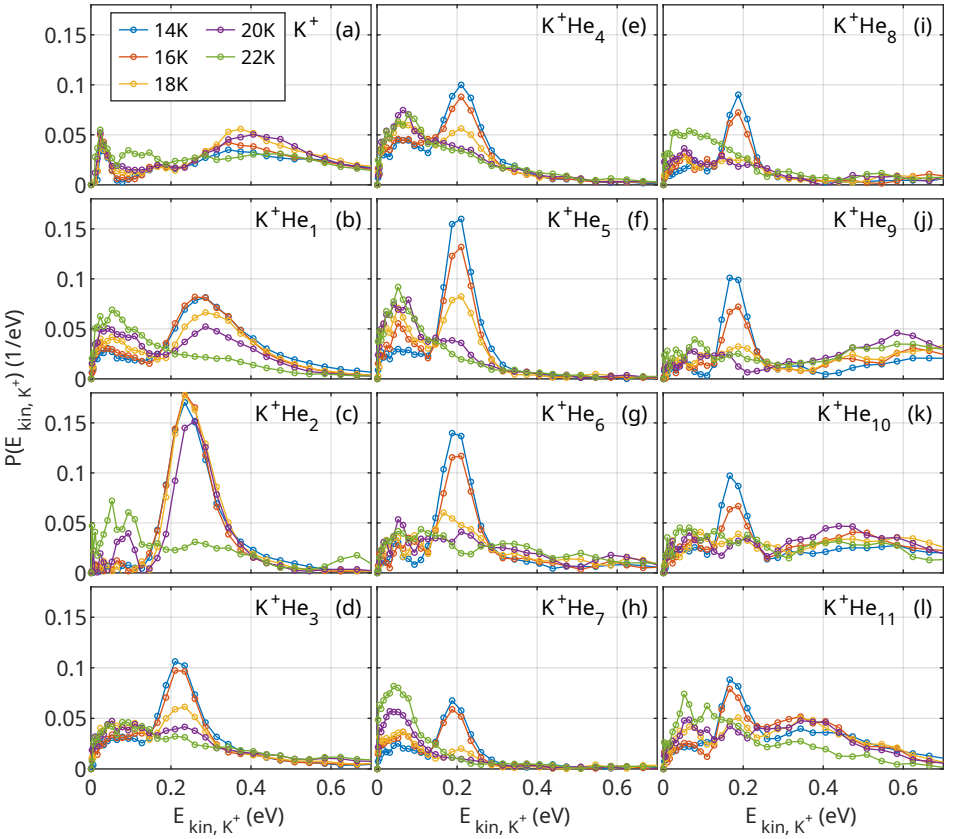

Figure 6.4: Kinetic energy distribution of detected K^+He_n clusters, shown for 5 different droplet sizes. The span of the E_{kin,K^+} axis has been limited to focus on the $Xe^+ - K^+He_n$ Coulomb explosion channel.

their helium attachments $Xe^{2+}He_n$, originating from the Coulomb explosion of Xe_2 dimers in the droplets. This is corroborated by these channels disappearing when the Xe doping is turned off, but still being present when the K doping is turned off.

Secondly, as the K^+He_n complexes get larger, their E_{kin} distributions generally shift towards lower energies. This shift is most drastic for $n \leq 3$, but it persists for the larger complexes as well. The primary reason for this shift is interpreted as lower kinetic energies are correlated with the K^+ ion leaving the droplet in a less violent process, thereby giving it a higher probability of attaching He atoms. Another reason for the shifts is that if Xe^+ behaves like a free particle, then E_{kin} of K^+He_n depends on n due to momentum conservation, see Eq. (6.10).

While the distribution of the different K^+He_n complexes are interesting in the sense that they provide insight into the mechanism by which the K^+ ions are ejected from the droplet surface, the main focus of this work is to find the initial Xe–K distance, r. In order to achieve this, we have to take into account all the possible channels that the K^+ ends up in, that is, all the different K^+He_n complexes. The E_{kin} distributions are density distributions, so that integrating them over a range of E_{kin} will give the number of ion counts detected per laser shot in that range. Thereby, the different distribution functions can in principle be summed together to find the distribution of K^+He_n kinetic energies across all complexes, and this is what we need to do in the case of $m_{Xe} \to \infty$. In the free recoil case, however, the momentum sharing correction factor in Eq. (6.10) makes the analysis more complicated. In this case, each $P(E_{kin,K^+He_n})$ distribution must be transformed to find the equivalent $P(r)$ distribution, and these distributions must then be summed. However, the Jacobian density function transformation also shifts the position of the points that the density function is sampled in. The different distributions must therefore be resampled to be on the same points on the r axis, so that they can be summed together. This resampling is done by a cubic spline, and the resampled $P(r)$ distributions for each K^+He_n can be summed. Only K^+He_n up to $n = 9$ were included in the sum to avoid the previously discussed Xe^{2+} channel.

The resulting distributions of K–Xe distances, $P(r)$, are shown in Fig. 6.5. Results for both effective masses of Xe^+ are shown, showing that this unknown parameter has a large influence on the final distribution. Comparing to Fig. 6.3, the signal-to-noise ratio is much better, and the trend of lower nozzle temperatures leading to larger r is clear. However, the peaks still lie on a large background, once again corresponding to the Jacobian transform of an approximately flat background in the E_{kin} distributions.

For comparison, the distribution of expected droplet sizes is also shown in

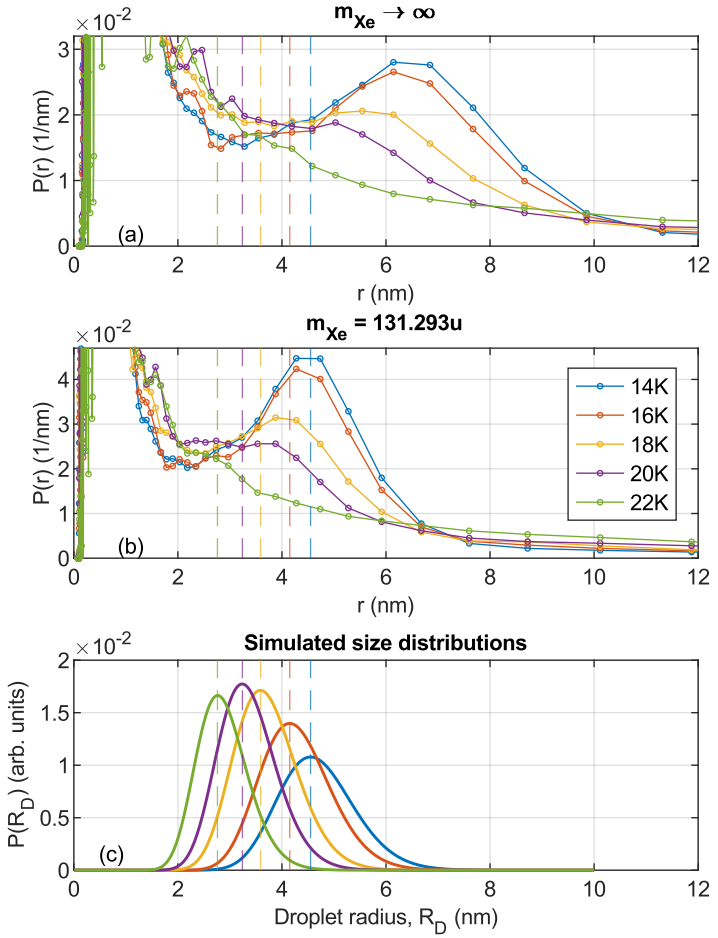

Figure 6.5: Xe – K distance (r) distribution obtained with contributions from the K^+He_n signals for $n = 0-9$, see text. The distributions for two effective masses of Xe^+ are shown, (a) $m_{Xe} \to \infty$, corresponding to Xe^+ being totally bound in the droplet, and (b) $m_{Xe} = 131.293$ u, corresponding to free recoil. Also shown (c) is he expected droplet radius (R_D) distribution of the droplets which are doped with two dopants, based on the experimental conditions (5 µm orifice, 50 bar stagnation pressure, nozzle temperature as given in the figure, doping pressure set to give the highest probability of double doping for 18 K droplets), see Section 2.4 in Chapter 2 for more information.

Fig. 6.5(c). This is the modelled distribution of radii for the droplets that are doped with two dopants, as explained in Section 2.4. The free parameter in the model, equivalent to the pressure in the doping cell, has been set to optimize the probability of having two dopants for droplets with an average size of 5200 atoms, equivalent to a 18 K nozzle temperature. If the Xe atoms are located exactly in the center of each droplet, then we would expect that r, the Xe – K distance, is equivalent to R_D, the droplet radius.

The correspondence between the experimental results and the droplet radius distribution will be discussed in the following section.

6.5 Discussion

Recoil scheme - Effective mass of Xe In Fig. 6.5, it is clear that the free recoil scheme shown in panel (b) corresponds much better to the droplet radius distribution in panel (c), when comparing to the bound Xe^+ recoil seen in panel (a). The bound Xe^+ recoil results are all significantly larger than the expected droplet radius distributions, while the free recoil results are comparable to the radius distributions. Assuming no major systematic errors, this would mean that the Xe^+ is free to move inside the droplet during the Coulomb explosion.

Given that the droplet is superfluid, this might not be a big surprise. However, based on the momentum sharing assumption, we can calculate the final speed of the Xe^+ ion as

$$v_{Xe^+} = \frac{\sqrt{2m_{K^+}E_{\mathrm{kin},K^+}}}{m_{Xe}}. \tag{6.17}$$

Assuming K^+ ends up with $E_{\mathrm{kin},K^+} = 0.5\,\mathrm{eV}$, see Fig. 6.4(a), gives $v_{Xe^+} = 467.2\,\mathrm{m\,s^{-1}}$. This is an order of magnitude higher than the Landau velocity of superfluid helium, see Section 2.2, whereby it should not behave as a superfluid.

While the completely free recoil scheme is not theoretically justified, we might guess that the motion Xe^+ ion is only partially restricted. This at least fits with the experimental results.

Effect of K^+-droplet attraction In the analysis resulting in Eq. (6.15), we neglected the attractive potential between the K^+ ion and the helium droplet V_D, primarily because it is not accurately known for all the droplet sizes used in the experiment. Note that this potential is simply the negative of what is called E_{dimple}

in Chapter 5. And even if $V_D(R_D)$ was accurately known, we would need to know how R_D corresponds to r to apply this correction properly, which is not possible.

In reference [2], the attraction a Na^+ ion feels when it sits on the surface of a droplet was calculated for two droplet sizes, called $E_{sim}(t=0)$ in the methods section of the paper. This gave $-115.4\,\mathrm{cm}^{-1}$ ($-14.3\,\mathrm{meV}$) for a 2000 atom droplet, and $-130.4\,\mathrm{cm}^{-1}$ ($-16.2\,\mathrm{meV}$) for a 5000 atom droplet. Thereby, V_D only seems to depend weakly on the droplet size. Furthermore, the value of E_{dimple} was derived in Section 5.7.2 based on the values published in reference [40] giving $V_D = -E_{\mathrm{dimple}}(K^+) = -11.7\,\mathrm{meV}$. We add this potential term to the derivation starting from Eq. (6.6), whereby the potential energy becomes

$$E_{\mathrm{pot}} = \frac{1}{4\pi\varepsilon_0}\frac{q_1 q_2}{r} - V_D. \tag{6.18}$$

Redoing the derivation until Eq. (6.14) gives

$$r = \frac{e^2}{4\pi\varepsilon_0}\left(\frac{m_{Xe^+}+m_{K^+}}{m_{Xe^+}}E_{\mathrm{kin},K^+} + V_D\right)^{-1}, \tag{6.19}$$

$$E_{\mathrm{kin},K^+} = \frac{m_{Xe^+}}{m_{Xe^+}+m_{K^+}}\left(\frac{1}{4\pi\varepsilon_0}\frac{e^2}{r} - V_D\right), \tag{6.20}$$

$$\frac{dE_{\mathrm{kin},K^+}}{dr} = -\frac{m_{Xe^+}}{m_{Xe^+}+m_{K^+}}\left(\frac{1}{4\pi\varepsilon_0}\frac{e^2}{r^2}\right). \tag{6.21}$$

The result of applying this analysis to the free-recoil case can be seen in Fig. 6.6. Comparing with Fig. 6.5(b), the V_D correction slightly shifts the experimental r distributions towards lower r values. This moves them closer to the expected peak positions of the droplet radius distributions, but the effect is not large enough to explain the full deviation, especially not for the smaller droplet sizes, 22 K to 18 K.

Shift of peak positions We will now compare the measured Xe–K distance distributions in Fig. 6.5(b) and Fig. 6.6 with the expected droplet radii. Not much at all is seen for the smallest droplet size (22 K). For the slightly larger droplets, 20 K and 18 K, we see that the measured r distribution is shifted towards lower r compared with the droplet radii. Meanwhile, the largest droplet sizes, 16 K and 18 K, are much closer to the simulated droplet sizes.

These results are obtained by summing the r distributions of the K^+He_n signals for $n = 0-9$. Looking at Fig. 6.4 for the 16 K and 18 K measurements, we do

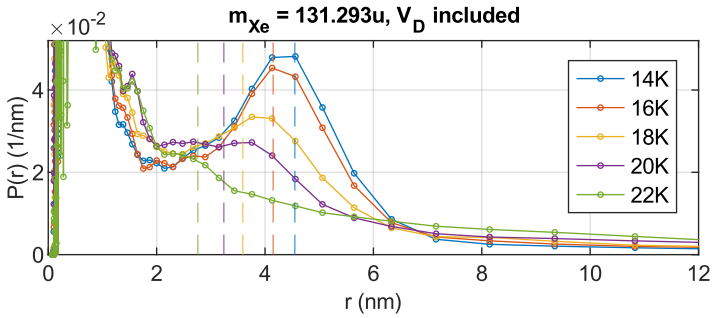

Figure 6.6: Xe – K distance (r) distribution obtained with contributions from the K^+He_n signals for $n = 0-9$, assuming free recoil, see text. The attraction to the droplet, V_D, has been taken into account by estimating this to be a constant value (-11.7 meV) regardless of droplet size. Shown in dashed lines are the expected peak positions of the radius distributions of droplets containing exactly 2 dopants, see Fig. 6.5(c).

however see the $K^+ - Xe^+$ Coulomb explosion channel for $n > 9$. This means that the summed distribution is lacking some signal that should ideally be included, if it didn't overlap with the previously discussed Xe^{2+} energy channels. We expect that the lack of this signal shifts the r distribution for 16 K and 18 K towards lower r.

With this effect accounted for, it seems plausible that the true r distributions are systematically shifted towards lower r. This systematic shift could come from a slight miscalibration of the VMI spectrometer, a deviation in the droplet creation scheme like a slightly different stagnation pressure or orifice opening than expected. Alternatively, it could be due to unaccounted effects in the physical system like discussed below.

Alkali surface position So far, the Xe – K distance, r, has been compared with the droplet radius, R_D. However, as discussed in Chapter 2, the alkalis do not sit on the droplet like a hard sphere, but rather float over a dimple, see Fig. 6.7. This is replicated by static DFT calculations, identical to the one used to find the initial geometry of a Na atom on a droplet as described in Chapter 5. Specifically, the case of a K atom in equilibrium on a 2000 atom helium droplet has been reported [40, Fig. 1]. The droplet radii, R_D, discussed in this chapter are the hard-sphere droplet radii, which assume that the helium in the droplet has an isotropic density profile. Thus, it would be interesting to know how far away from the hard-sphere radius the K atom is located, this distance could be called d_K. Luckily, reference [40] tells us

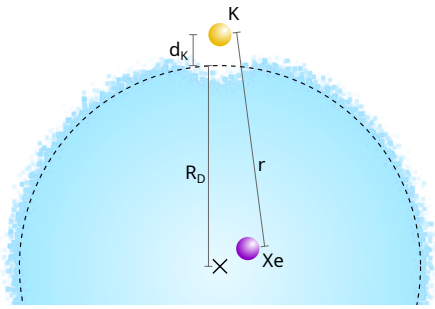

Figure 6.7: Illustration of the co-doped helium droplet, showing the K – Xe distance r. The dashed circle represents the hard sphere radius, R_D, of the droplet, see Chapter 2, relative to the droplet center marked by an "x". d_K distance from the hard sphere radius to the center of the K atom.

that the 2000 atom droplet used has a hard-sphere radius of 28.0 Å. Using this, and by careful measurements of Figure 1 in the paper, we find that the center of the K atom sits $d_K = 0.44$ nm outside the hard-sphere radius of the droplet.

The distance d_K could depend somewhat on the droplet size, but we currently only know the value for 2000 atom droplets. However, the dimple structure that the alkali sits in is a rather local effect, and therefore, we believe that d_K does not have a strong dependence on droplet size.

Accounting for d_K in the results would mean that the expected r values need to be 0.44 nm larger than R_D. In Fig. 6.6, this improves the correspondence between experiment and model for the 20 K and 18 K droplets. For the 16 K and 14 K droplet, however, the correction makes it out so the experimental droplet sizes are significantly smaller than expected. This is, however, well in line with the expected underestimation of the larger droplet sizes due to loss of K^+He_n signal for $n > 9$, as discussed above. All in all, taking d_K into account only seems to improve the correspondence between the experiment and the model.

Width of the distribution Due to the background signal present in the experimental results, it is difficult to accurately access the width of the experimental distributions. However, on visual comparison of the free recoil experimental distributions in Fig. 6.5(b) and the expected droplet size distributions in Fig. 6.5(c) shows that the experimental distributions are only slightly wider than the expected ones.

This is very surprising because this suggests that the Xe atom is confined to the center of the droplet. If the Xe was free to roam in the droplet exterior, the Xe – K distance would change based on the exact location of the Xe at the time of probing, see Fig. 6.7. Thereby, the result suggests that Xe does not roam more than a couple of angstroms away from the center of the droplet. This is in opposition to the previous understanding of inside-bound neutral dopants as relatively free roamers [73].

Correctness of the model Like discussed in Section 2.4, the model droplet radius distributions used are the best guess we have, but by no means a certain standard. They are based on the interpolation of results at 40 bar and 60 bar stagnation pressure, to compare with our experimental conditions at 50 bar. Furthermore, although the model results were obtained on a helium droplet instrument similar to ours, it is not identical. It is, for instance, well known that there is a somewhat large uncertainty in the size and shape of the nominally 5 µm orifice used for expanding the helium gas[5]. To improve the experiment, an independent measurement of the droplet size distribution for our specific setup would improve the certainty of the comparison significantly. Within these uncertainties it is almost surprising how well the experimental results fit with the expected values. This suggests that the goodness of the correspondence could be a coincidence, and the experiment needs to be repeated using a different experimental setup to verify.

6.5.1 Perspective

As discussed above, if various potential systematic errors are assumed not to affect the experiment, the experiment indicates that the xenon atom is stuck in the center of the droplet. This is in contradiction with the previous understanding of neutral dopants roaming around the droplet interior in a somewhat flat potential landscape [73]. To properly test this disagreement, the experiment could be repeated on size selected helium droplets. From discussions with members of Prof. Paul Scheiers group, I know that a setup exists that charges helium droplets, selects out a specific size of these charges droplets and finally neutralize the droplets again. If the experiment was repeated by doping these size selected droplets, the distribution r would directly reflect the distribution of positions of the Xe atom.

[5] According to unpublished electron microscope measurements done by Lorenz Kranabetter.

From the found experimental results, it is clear that r is several nanometers. This in contradiction with an experimental paper finds that the rotational spectrum of droplets co-doped with HCN molecules and various alkali atoms matches that of a closely bound HCN – Ak complex [32]. While the Ak atoms might be more attracted to the HCN molecules than they are to the Xe atom, this is also in contradiction with what was found in this chapter. This distance determination experiment could be repeated with HCN as the inside bound dopant, to test the conclusion of reference [32] more directly. However, handling the very toxic HCN would require changes to the experimental procedure. Note that DFT simulation studies have previously found that Xe and Rb do not form complexes, but stay on the surface and in the center respectively [91], in agreement with the results presented in this chapter.

One thing to note is that the experiment in this chapter is not sensitive to small distances r. If a closely bound Xe – K complex was formed on the surface of the droplet, the kinetic energy that the K^+ would get from the Coulomb explosion of this complex would likely overlap with the kinetic energy of K^+ ions created from the Coulomb explosion of K_2 dimers. Thereby, the conclusion taken from this chapter should not necessarily be that no closely bound Xe – K dimers are formed, but rather than there are also many droplets co-doped with Xe and K where they aren't formed, and the Xe is rather free to be somewhere inside the droplet.

6.6 Conclusion

In this chapter, the measurement of the Xe – K distance, r, in co-doped helium droplets have been discussed. The results are presented for a range of droplet sizes corresponding to helium nozzle temperatures in the 14 K to 22 K range. It has been concluded that the experiment does not work well when only taking K^+ ions into account. However, when taking the helium tagged ions, K^+He_n, into account, the resulting r distributions correspond well with the expected droplet radius distributions. Accounting for the attraction the K^+ ion feels from the polarizable droplet and the exact location of the K above the droplet surface further enhances this correspondence. In the end, the results fit with well with the expected values, although the size of the largest droplets (16 K and 14 K) are believed to be underestimated in the experiment, due to lost signal of larger K^+He_n complexes.

CHAPTER 7

Droplet Size Dependence of Alkali Ion Solvation

In Chapter 5, the solvation dynamics of alkali ions (Na^+, Li^+, and K^+) on the surface of helium droplets were studied by ejecting the ions at a given time after ionization using the repulsion of a xenon ion. In Chapter 6, it was found that the kinetic energy that an alkali ion gets from this repulsion can be used to calculate the initial distance between the alkali ion and the xenon ion. Furthermore, it was found that this distance could be indicative of the radius of the droplet.

In this chapter, these two techniques will be combined to resolve the solvation results presented in Chapter 5 in terms of the Xe – Ak distance, r.

7.1 Experimental details

The datasets that will be analyzed and presented in this chapter are the same as those which were presented in Chapter 5. As such, the details of the experiments for the three different alkalis can be found in Section 5.3, Section 5.7.1, and Section 5.7.3. The data obtained is a list of ion hits, recording the x and y detector coordinates and Time-of-Flight (TOF) as a function pump-probe delay t.

7.2 Resolving ion yields according to *r*

The TOF of each ion hit was calibrated to a mass-over-charge (m/q) ratios and those ion hits that corresponded to the different possible Ak^+He_n complexes were collected based on their mass, following $m(Ak^+He_n) = m(Ak^+) + n \cdot 4\,u$. For each t, the ion image of each Ak^+He_n was inverted using the MEVIR algorithm [31], yielding the time dependent detector radius distribution for each complex $P(r_D;t,n)$. These $P(r_D;t,n)$ were transformed into kinetic energy distributions $P(E_{kin};t,n)$, using the calibration factor obtained from constraining the Coulomb explosion channel of the Ak_2 dimers in the triplet state to those kinetic energies reported in reference [62]. As detailed in Section 6.4, the $P(E_{kin};t,n)$ can be transformed into the distribution of Xe – Ak distances $P(r;t,n)$, simply treating each t step as its own set of $P(r;n)$ distributions. Here, the "free-recoil" model was used, because it gave the best correspondence between the expected and measured $P(r;n)$ in Chapter 6. Like in Section 6.4, each $P(r;t,n)$ was resampled to lie in the same r points across different n, using a cubic spline interpolation. Note that the $P(r;t,n)$, $P(E_{kin};t,n)$ and $P(r_D;t,n)$ are all *density distributions*, rather than probability distributions, integrating them over a range of r, E_{kin} or r_D respectively will give the number of ion counts found in that range.

The resulting $P(r;t,n)$ distributions of Na^+ are shown for a select range of n in Fig. 7.1. The time dynamics of the signal are clearly dependent on r. For larger r, for instance 5 nm, the signal appears at earlier t than for smaller r, for instance 1 nm, across all Na^+He_n complexes. According to the TDDFT simulation shown in Section 5.1.4, the Na^+ ion will stay in the same position on the droplet surface during the 20 ps measured in the experiments. Thereby, for a given single droplet, r, the distance between the Xe atom and the building Ak^+He_N complex, should remain constant as time progresses. This means that the shifting r distribution should be interpreted as a consequence of the solvation dynamics shifting the signal between different Na^+He_n complexes. In other words, the measured r depend only on the configuration of the initial co-doped droplet, not on the dynamics induced by the pump pulse. The analysis presented in Chapter 5 can thereby be repeated for any specific r, to yield the r dependence of the solvation dynamics.

Another interpretation of this data has to be addressed, which is that the Na^+ ion is moving inside the droplet, thereby lowering the Xe – Na distance r[1]. However, this does not explain why the time dynamics are markedly different for different

[1] A fun fact: This is what the solvation experiment was initially designed to measure.

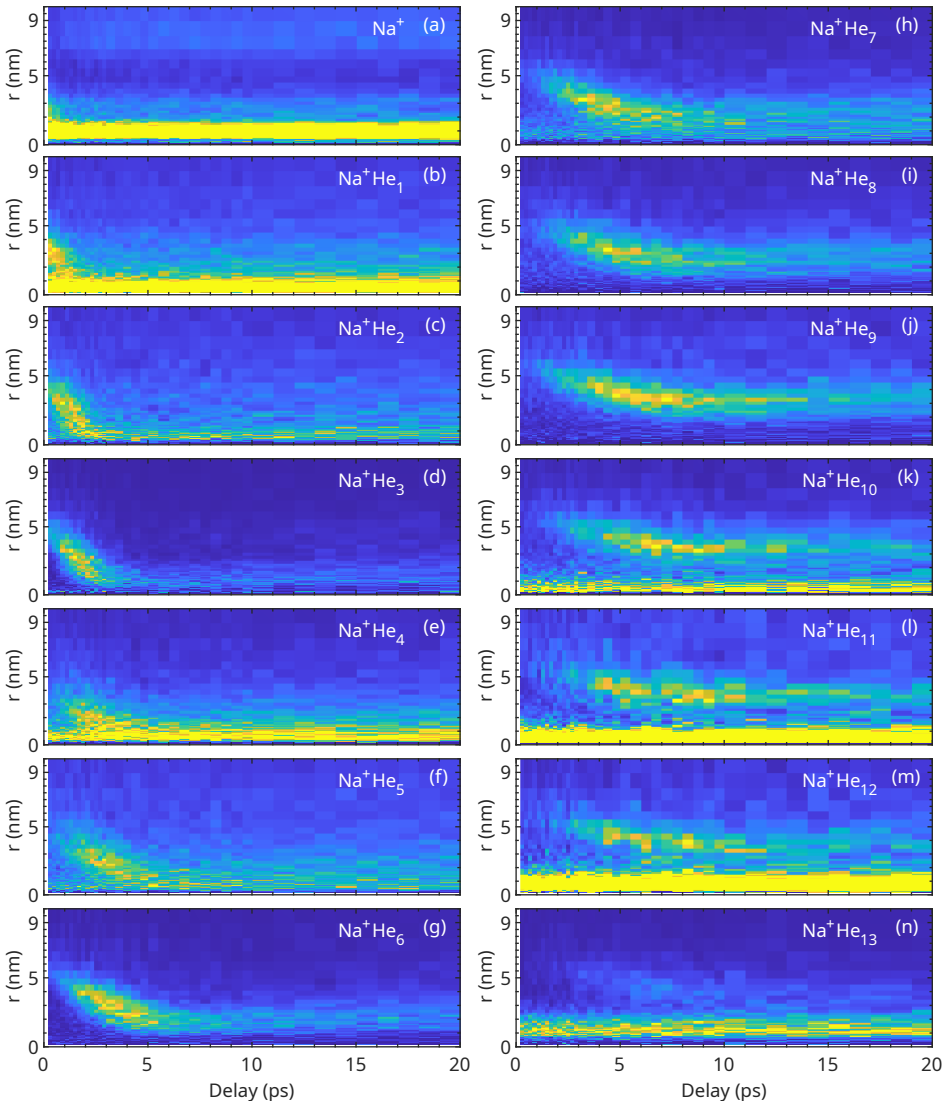

Figure 7.1: The Xe – Na distance (r) distribution $P(r;n,t)$, as a function of pump-probe delay (t) and Na^+He_n complex size, see text. The colormaps are each on an arbitrary scale.

Na^+He_n complexes. Furthermore, it is incompatible with the TDDFT simulations as discussed above. Looking for example in Na^+He_3, see Fig. 7.1(d), the most probable r shifts from $\sim$5 nm to $\sim$1 nm in about 2.5 ps, which corresponds to an average speed of $\sim 1.6\,\mathrm{km\,s^{-1}}$. No force is present in the droplet to suddenly accelerate the ion to such a speed. For these reasons, this interpretation is discarded, and the stationary-ion interpretation presented above is used instead.

To quantify the solvation dynamics, the Poisson model analysis from Section 5.5 will be repeated for different ranges of r. In order to overcome statistical fluctuations, the data shown in Fig. 7.1 must be integrated over small ranges of r. This gives the ion yield in the specific r range as a function of t, and is repeated for each Na^+He_n. These are background subtracted by subtracting the minimum point from each trace. The resulting yield curves are shown in Fig. 7.2 for three different r ranges as examples.

7.3 Poisson model of helium attachment rate

For each r range, the Poisson model fit to Eq. (5.3) was made, once again as a global fit to the ion yields of $n \leq 5$ like described in Section 5.5. The result is shown in Fig. 7.2 as full blue lines.

From Fig. 7.2, it is seen that the time dynamics of the three different r ranges differ. Noticeably, larger r seem to show both a more negative lift-off time t_{lo} and a faster attachment rate λ_{He} of helium. The exact λ_{He} and t_{lo}, will be discussed later, in comparison with results for Li^+ and K^+. Furthermore, the deviation from the Poisson model seems very dependent on r. The smaller $r = 1$ nm to 2 nm range shows a significant portion of signal at the latest times in the $n = 3-6$ range, which is only present to a minor degree in the $r = 2.75$ nm to 3.5 nm range, and totally absent in the $r = 5$ nm to 6 nm range. This points to the approximately steady state distribution of n reached at the latest t being a result of vibrational excitation during the Xe^+ – Na^+He_N repulsion leading to dissociation. In this effect, the larger r should lead to a more accurate representation of the complexes present at the surface. However, a competing effect is also seen, namely that t_{lo} becomes more and more negative for larger r. This corresponds to the complexes having more interaction time with the droplet after the probe pulse, which corresponds well with the weaker repulsion of the larger Xe^+ – Na^+He_N distance. As seen for the $r = 5$ nm to 6 nm range, this makes the peaking structure of the smaller Na^+He_n complexes harder to resolve. In this effect, the larger r are less representative of

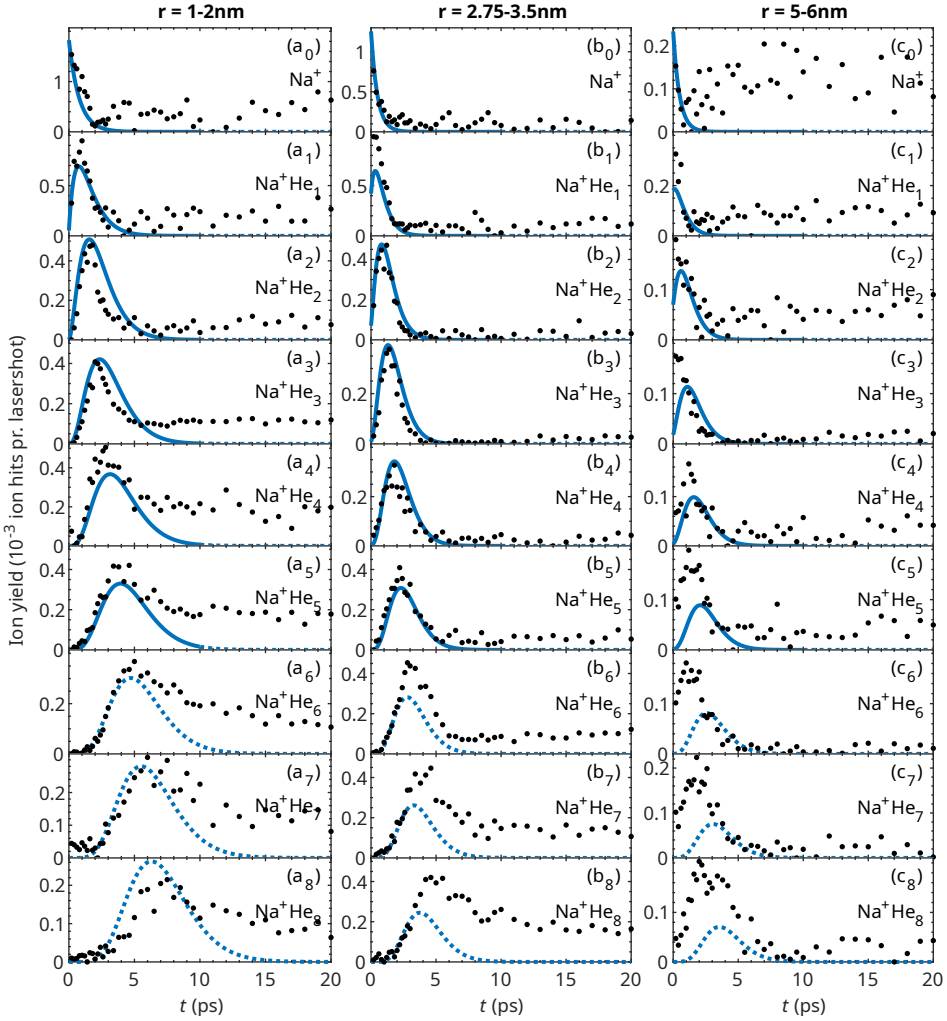

Figure 7.2: Experimental ion yields of Na^+He_n for specific ranges of the Xe – Na distance r are shown in black points. Poisson model fits using Eq. (5.3) are shown in full blue lines, while the extrapolation of these beyond the fitting range are shown in dashed blue lines.

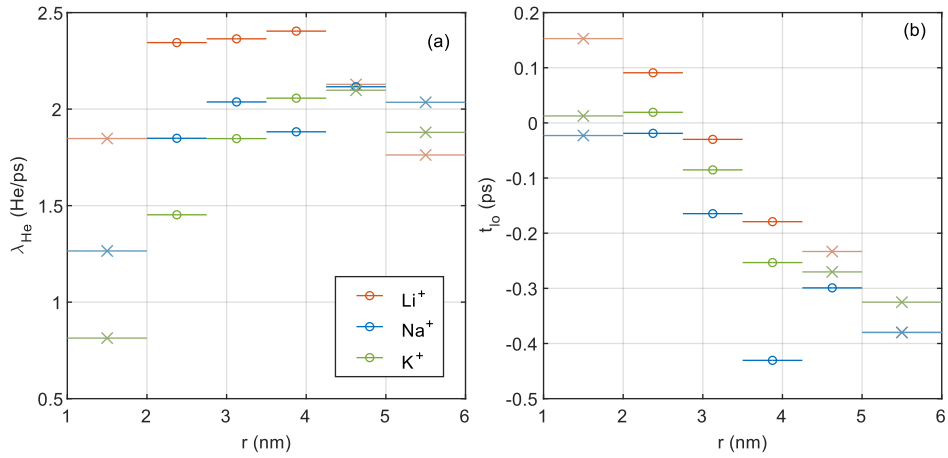

Figure 7.3: Comparison of the fitted λ_{He} and t_{lo} for different ranges of r, shown for the three different alkali solvation experiments. The r ranges that has been integrated over is represented by the horizontal bars. Circles mark trustworthy results, while crosses mark results where known problems have a large influence on the quality of the fit.

the solvation state on the droplet surface at the time of the probe pulse. All in all, it seems that the middle range $r = 2.75\,\text{nm}$ to $3.5\,\text{nm}$ is most representative of the actual solvation dynamics.

Comparing with the similar Fig. 5.4, which shows the same results essentially integrated over all r, the r resolved yields naturally have more noise. This affects the Poisson fits, however systematic deviations are also seen. For the $r = 1\,\text{nm}$ to $2\,\text{nm}$ range, it seems that the smaller complexes, $n = 1-3$ have narrower peaks compared to the Poisson model, while the $n = 4-5$ fit the Poisson model better. This could be due to dissociation effects, as the smaller r leads to a stronger force on the ejected Na^+He_n, and thereby more potential dissociation. This could lead to the $n = 4-5$ yields being smeared out towards larger times, like what was seen for the $n = 6-9$ yields in Fig. 5.4. On the other hand, the fit to the $r = 2.75\,\text{nm}$ to $3.5\,\text{nm}$ range looks good for the whole fitted range of $n = 0-5$. The fit to the $r = 5\,\text{nm}$ to $6\,\text{nm}$ range is not good, but this could be ascribed to a larger amount of noise. The lack of dissociation effects for this range might make it possible to improve the fit by including higher n, but using different n ranges for the fits would complicate comparison between the different r ranges.

The helium attachment rate λ_{He} and lift-off time t_{lo} extracted from the fits

are seen in Fig. 7.3. In addition to the r ranges shown in Fig. 7.2, fits have been made for r =2 nm to 2.75 nm, 2.75 nm to 3.5 nm, 3.5 nm to 4.25 nm and 4.25 nm to 5 nm. These generally resemble the $r = 2.75$ nm to 3.5 nm range in quality of fit, and will be referred to as the "trusted ranges". For these trusted ranges, the helium attachment rate λ_{He} have the same values within the uncertainty, however a slight rise in λ_{He} as r gets larger could be suggested. The lift-off times t_{lo} show a clear dependence on r, with larger r corresponding to more negative t_{lo}. This corresponds to a larger r leading to a longer time for the ejected complex to interact with the droplet after the probe pulse. This is expected, as larger r lead to a softer ejection, due to the weaker Xe^+ – Na^+He_N repulsion.

One very important note about these r resolved yield curves is that the linear rise at early t for larger fragments is absent, as shown in Fig. 7.2. This is true up to the $n = 8$ shown in the figure, and also for larger fragments, at least up to $n = 12$. The $r = 2.75$ nm to 3.5 nm range remarkably follows the rise of the Poisson fit curve, even beyond the fitted range. This suggests that the linear rise is not an effect of some physical process that deviates from the Poisson model, like the many-body collisions discussed in Chapter 5, but rather an effect of integrating over a distribution of droplet sizes. The biggest shift between the different r ranges seems to be the t_{lo}, and integrating over a range of these could lead to the more linear rise seen in Fig. 5.4. This is analogous to the smearing of the dopant number (k) distribution when integrating over the droplet size distribution, discussed in Section 2.5 see Fig. 2.2(a).

7.4 Results for Li^+ and K^+

The analysis was repeated for the Li^+ and K^+ solvation experiments from Chapter 5. The ion yields and fits for some selected r ranges are shown in Fig. 7.4 for Li^+ solvation, and in Fig. 7.5 for K^+ solvation. For the K^+ solvation, the fitted range of n had to be restricted to $n = 1-9$, to avoid noisy yield curves. For Li^+ solvation, the fitting range of $n = 0-3$ was used like in Chapter 5. Overall, the correspondence between experimental data and fitted model follow the trends of the Na^+ case, with the middle ranges r =2 nm to 2.75 nm, 2.75 nm to 3.5 nm, and 3.5 nm to 4.25 nm giving the best fits for both the Li^+ and K^+ data.

Below, the fitted parameters t_{lo} and λ_{He} will be compared for the different alkalis and the different r ranges.

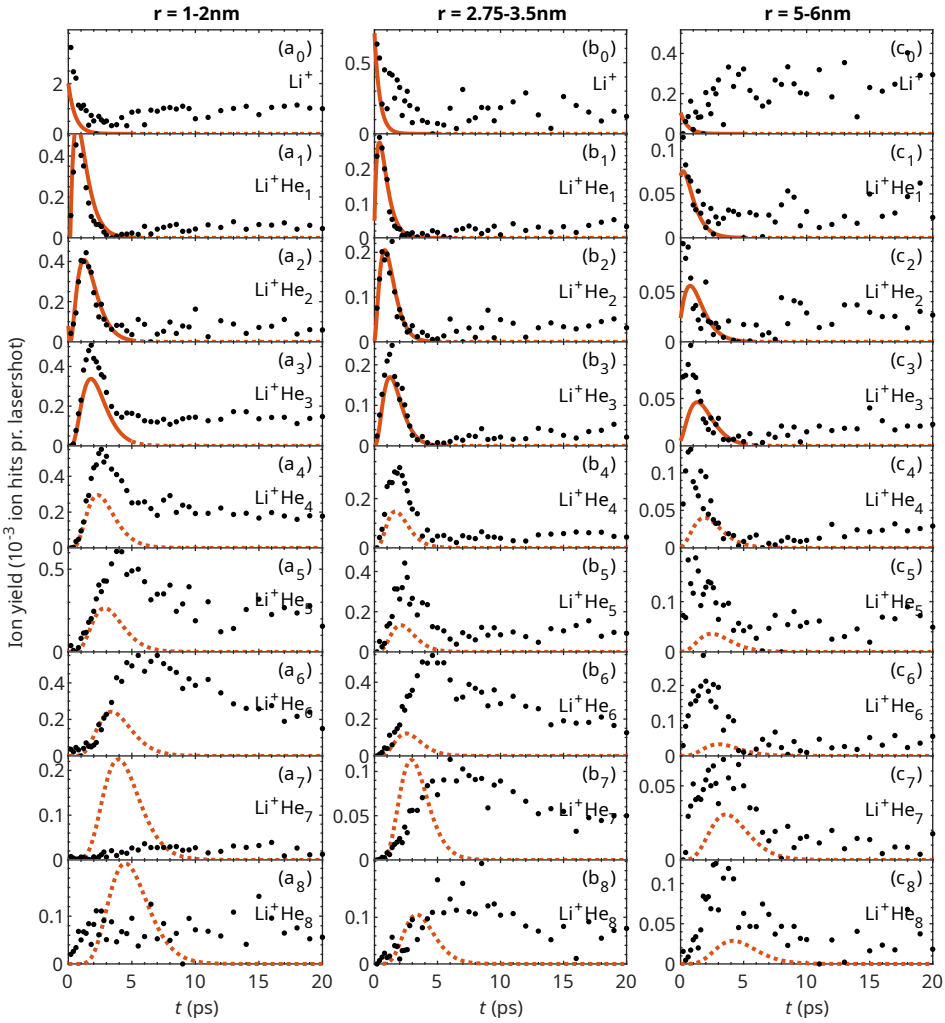

Figure 7.4: Experimental ion yields of Li^+He_n for specific ranges of the Xe−Li distance r are shown in black points. Poisson model fits using Eq. (5.3) are shown in full red lines, while the extrapolation of these beyond the fitting range are shown in dashed red lines.

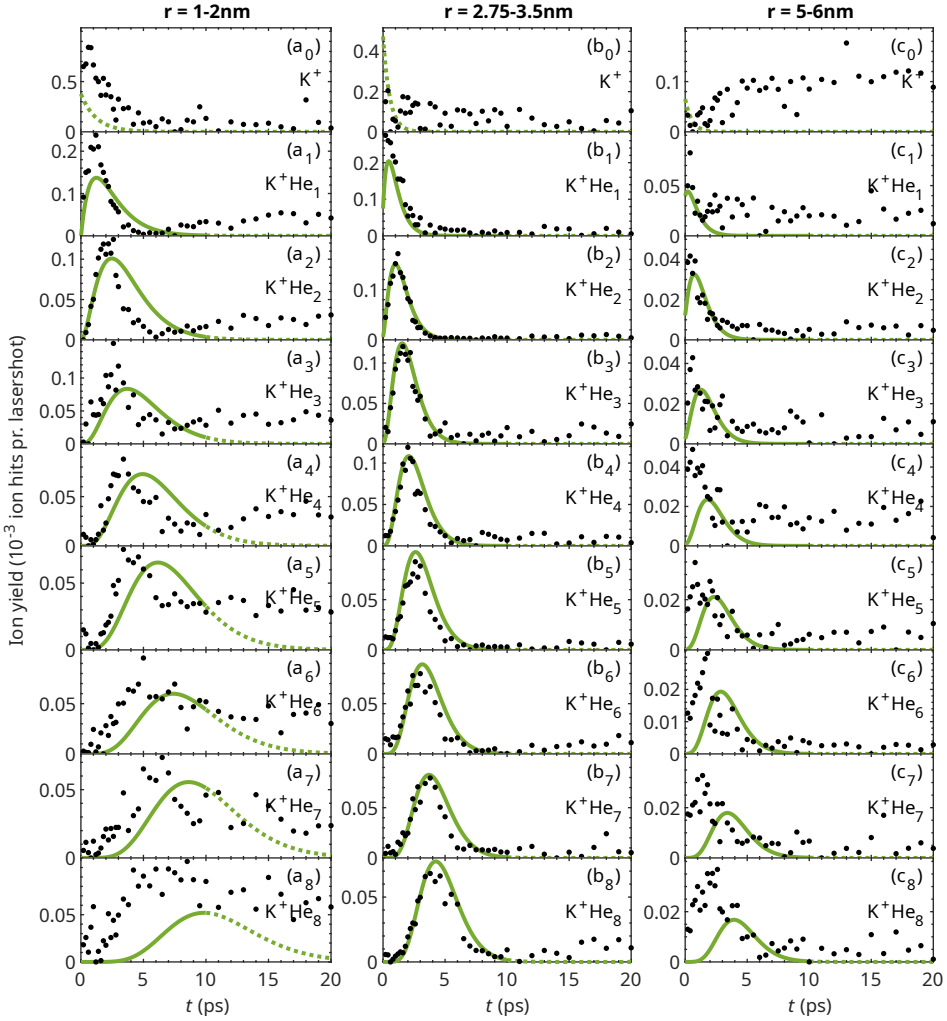

Figure 7.5: Experimental ion yields of K^+He_n for specific ranges of the Xe – K distance r are shown in black points. Poisson model fits using Eq. (5.3) are shown in full green lines, while the extrapolation of these beyond the fitting range are shown in dashed green lines.

7.4.1 Liftoff time, t_{lo}

The t_{lo} found for the Li^+ and K^+ data shown in Fig. 7.3(b) both show the same downwards trend as the Na^+ case, completely within the physical interpretation. When comparing them directly, the Li^+ experiment shows the least negative t_{lo}, corresponding to the lighter species being ejected faster from the droplet. In the $r = 2$ nm to 2.75 nm case t_{lo} even turns positive, which would correspond to the complexes being ejected from the droplet *before* the probe pulse. This is obviously not physically possible, and this result is rather interpreted as the repulsion process adding so much internal energy to the complex that it dissociates. In a sense, the complex needs to dissipate this extra energy before a given complex can be measured, which gives the positive t_{lo}.

From the masses of the three alkalis, we would expect t_{lo} to be least negative for the Li^+ experiment, moderately negative for the Na^+ experiment, and most negative for the K^+ experiment. This is however not the case, and as shown in Fig. 7.3(b), the Na^+ experiment gives more negative t_{lo} than the K^+ experiment. The much weaker binding energy of the K^+He_n complexes when compared to the Na^+He_n complexes could be the cause, see Fig. 5.5. This could lead to enhanced dissociation of the K^+He_n complexes, and thereby, shift the measured t_{lo} towards less negative values.

7.4.2 Helium attachment rate, λ_{He}

Comparing the found λ_{He} in Fig. 7.3(a), we see a somewhat different picture for the three alkali ions. For Li^+, the three trusted r ranges λ_{He} are consistent, maybe with a slight upwards trend in r, like what was found for the Na^+ experiment. This suggests that the helium attachment is a local process that is not very dependent on droplet size. On the other hand, the λ_{He} found for K^+ show a strong dependence on r. It would be strange if the helium attachment only depended on the droplet size for K^+ ions, and not the other two tested ions. This r dependence is rather interpreted as a result of repulsion induced dissociation of the K^+He_N complexes, leading to the later detection of larger n for smaller r. This is consistent with the above discussed shift of t_{lo} for the K^+ data. The reason why this effect is much stronger for the K^+ experiment than the other two alkalis could be that the binding energy of the K^+He_N complexes is comparatively lower, and because larger n have to be included in the Poisson fit.

Comparing λ_{He} for the three different alkalis directly, it is seen that they are

more distinct than what was found in Chapter 5, with λ_{He} clearly being larger for Li^+ solvation than Na^+ and K^+ solvation. Within the uncertainty of the dissociation effect discussed above, it is hard to tell if λ_{He} for Na^+ is also larger than for K^+, but it is not impossible. This is consistent with the progressively weaker $Ak^+ - He$ pair potentials of the heavier alkalis, however, the solvation dynamics are more complex than just depending on the pair potentials. This result suggests that the Li^+He_N complex is able to get rid of its internal energy slightly faster than the other alkali, an effect that will be investigated further in the next section.

7.5 Energy dissipation

In this section, we will determine the dissipated energy for different ranges of r, following the analysis in Section 5.6. The ion yields for a specific r range were transformed into time dependent n distributions $P_t(n)$ using Eq. (5.10), and from these, the upper and lower bounds of the mean dissipated energy $\langle E_{disp} \rangle (t)$ were calculated using Eq. (5.11). The results are shown for all analyzed r ranges and for all three alkali in Fig. 7.6. Additionally, exponential fits to the middle of each $\langle E_{disp} \rangle (t)$ band were made using Eq. (5.12) as the fitting function. Here, the fitted time-ranges are chosen for each r range based on two criteria: The first is having approximately no population in the largest measured Ak^+He_n complex, which indicates that we measure the full $P_t(n)$ distribution. The second is having a limited amount of background signal in the lower n complexes, a signal which rises over time as it comes from dissociative ionization of Ak_2 dimers as discussed in Chapter 5.

Fig. 7.6 shows that the exponential model fits most of the fitted r ranges well. This once again shows that the microscopic cooling of the solvation complexes follow the macroscopic Newton's law, as was the case in Chapter 5.

The exceptions are the results for K^+ in all ranges except the two largest r, showing poor exponential fits like what was found for K^+ in Chapter 5. One explanation for these deviations could be the lower binding energy of the K^+He_N complexes, compared with Na^+He_N and Li^+He_N, leading to a larger effect of repulsion induced dissociation, like discussed above. This would lead to the complexes needing to dissipate more energy to the droplet to overcome the repulsion induced energy, effectively stagnating the energy dissipation curve, so that there is a delay in when the energy dissipation curve starts rising. This is not included in the fitted model, which might result in the bad fit quality. An alternative reason could be the

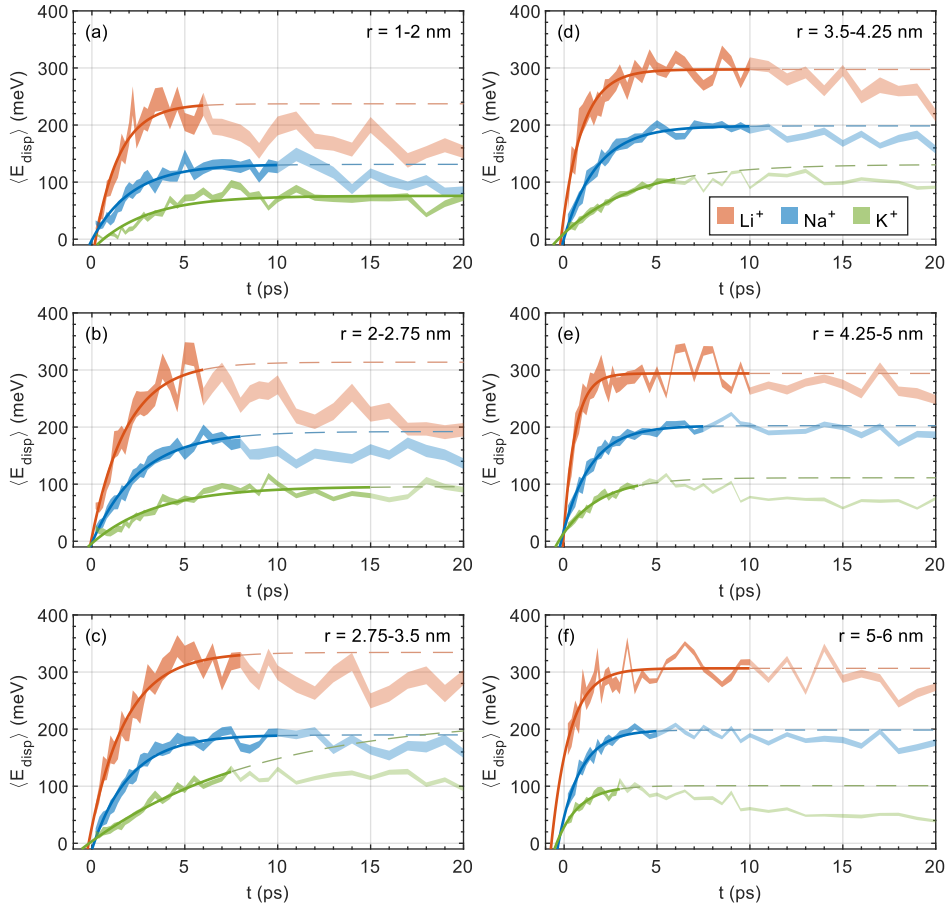

Figure 7.6: Upper and lower bound of $\langle E_{\mathrm{Disp}} \rangle$ for Li^+, Na^+ and K^+ solvation, shown in colored bands for 6 different ranges of r. Also shown are exponential fits to the function Eq. (5.12), where full lines signify the fitted range, and dashed lines are interpolations beyond this range.

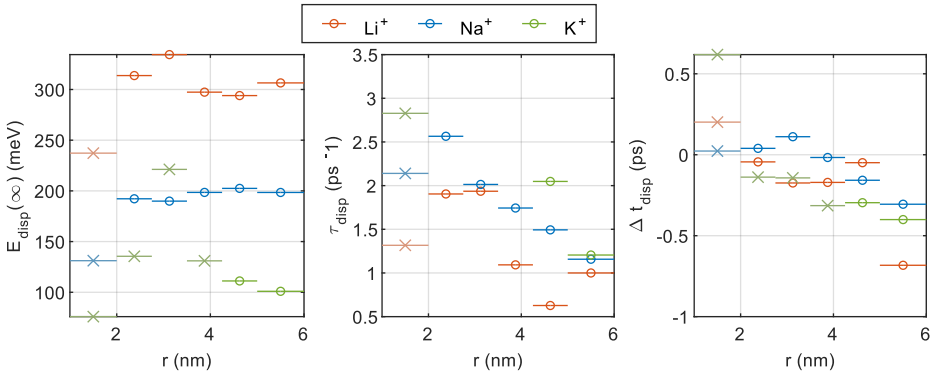

Figure 7.7: Fit results for the three parameters in the fitted function Eq. (5.12). The bars indicate the r range integrated over. Crosses indicate poor quality fits where the data clearly deviates from the model, while circles represent trustworthy fits. Note that some τ_{disp} values for poor fits to K^+ fall out of the shown range.

overestimation of the $n = 0$ ion yield at early times, like discussed in Chapter 5.

In order to quantitatively compare the energy dissipation results, the three fitting parameters (The asymptotic dissipated energy $E_{\text{disp}}(\infty)$, the characteristic lifetime τ_{disp} and the time shift Δt_{disp}) are shown in Fig. 7.7. Below, the results for these three parameters will be discussed.

$E_{\text{disp}}(\infty)$**:** Aside from the smallest range $r = 1\,\text{nm}$ to $2\,\text{nm}$, the trusted fits show that the final amount of dissipated energy is independent of r for all tested alkali ions, within the accuracy of the fits. This corresponds well with the physical interpretation of the process, as the solvation energy of the alkali ions is mostly a local phenomenon, and only has a weak dependence of the droplet size. The reason why the $r = 1\,\text{nm}$ to $2\,\text{nm}$ deviates might be that dissociation effects influence the result, so that we effectively measure the dissipated energy that is left after subtracting the repulsion induced energy. Furthermore, the three different alkali show markedly different $E_{\text{disp}}(\infty)$, like what was found in Chapter 5, in good accordance to their different solvation energies[40].

τ_{disp}**:** The found dissipation lifetimes are somewhat noisy, due to the noisy data. However, for Na^+ solvation, a clear trend is seen, where a larger r corresponds a lower τ_{disp}. This suggests that a larger droplet is able to dissipate

the solvation energy more quickly than a smaller one. The same trend is seen in the Li^+ data, and suggested in the K^+ data. The data suggests that Li^+ is able to dissipate energy most quickly, followed by Na^+ while K^+ seems to dissipate energy most slowly. τ_{disp} only expresses the lifetime of the exponential. When considering the differences in $E_{\text{disp}}(\infty)$ it is clear that Li^+ dissipates energy much faster than Na^+, which is again much faster than K^+. This is in accordance with the progression of the $Ak^+ - He$ pair potentials, if a stronger pair potential leads to quicker energy dissipation due to a stronger Ak^+-droplet coupling.

Δt_{disp}**:** The timeshift follows the trend of the lift-off time discussed for the Poisson fit in Section 7.4.1. Furthermore, the size of t_{lo} and Δt_{disp} correspond well within the uncertainty of the different fits, compare Fig. 7.3(b) Fig. 7.7(c). It seems that Δt_{disp} is indeed the lift-off time t_{lo}, and that the difference between these values are only due to different uncertainties in the methods used to retrieve them.

7.6 Discussion

7.6.1 *r* and droplet sizes

As discussed in Chapter 6, the Xe – Ak distance r seems to reflect the droplet radius R_D, with some convolution with the roaming radius of the Xe atom. Based on this, some results of this chapter can be said to reflect a droplet size dependence on the solvation process.

A clear trend of larger droplets dissipating energy from the solvation complex faster has been found. The corresponding helium attachment rates λ_{He} have not been found to have a clear droplet size dependence, however, this could be obfuscated by noise in the signal. The reason why this noise is less relevant for the energy dissipation result could be that all n are used for the $\langle E_{\text{disp}} \rangle$ calculation, while only a few n can be included in the Poisson fits used to extract λ_{He}.

The lift-off time t_{lo}, or equivalently Δt_{disp}, has been found to be dependent on r. The physical interpretation is that this is an effect of the strength of the $Xe^+ - Ak^+He_n$ repulsion, and thereby a direct effect of r, rather than the droplet radius R_D. Similarly, the many effects of repulsion induced dissociation should be thought of as r effects rather than R_D effects.

7.6.2 Experimental limitations

The experimental data presented in this chapter was originally recorded with the analysis presented in Chapter 5 in mind. Thereby, the experimental conditions, and especially recording times, were set based on integrating the signal over a single broad range of r. Subdividing this range into 6 different r ranges has obviously limited the amount of counts in each range, leading to noise in the signal. However, in potential future experiments, this can be improved.

The Na^+ and Li^+ data was recorded with the 1 kHz laser system available at the time. With the newer 5 kHz laser system, 5 times as much data could be recorded in the same amount of time, see Section 3.4. The 5 kHz laser system was used for the K^+ experiment, however, the recording time was limited to 5 hours. Simply by repeating the experiments with the 5 kHz laser system and long recording times, the experiment could be significantly improved.

When the probe laser intensity or focal volume is increased, so is the signal. The limiting factor in all three experiments is the intensity of H_2O^+ signal, which must be kept below the damage threshold of the MCP detector, see Section 3.6. If the amount of water in the vacuum chamber can be reduced, that shifts this restriction and more solvation signal could be obtained. Furthermore, if the density of co-doped droplets could be increased, then the solvation signal could be increased as well. However, the droplet density is already pushed to the upper limits of the capabilities of the vacuum setup by running the droplet source backing pressure at 50 bar, see Section 3.2.

An obvious extension of the experiment would be to repeat it for different average droplet sizes by changing the nozzle temperature. If the assumptions used in this chapter holds true, then the same r range should give the same solvation dynamics, even when the average droplet size is changed. Testing this experimentally would lend credibility to the experiment and analysis overall.

7.6.3 Future prospects

The results presented in this chapter are very much preliminary and subject to change when the improved experiment discussed above has been completed. Aside from providing further insight into the mechanisms behind results of the solvation experiment of Chapter 5, the prospect of resolving droplet size effects is interesting. Theoretical modelling of the droplet size dependence is however lacking.

The TDDFT calculations become much more computationally expensive when

the droplet size is increased. For this reason the TDDFT calculations in reference [40] are limited to droplets containing 2000 He atoms. Furthermore, the TDDFT simulation does not include the probe step, where the Ak^+He_n complex is ejected from the droplet. This step is critical to understanding the r dependence of the results shown in this chapter. Hopefully this effect can be included in the simulations in the future.

At the QFC2024 conference, Dr. Florent Calvo presented an alternative technique to simulate the solvation experiment, called ring polymer molecular dynamics. According to F. Calvo, these are less computationally expensive than the TDDFT calculations, and he was therefore able to include the probe step in the simulations. When these simulations are further developed in the future, they could hopefully provide a direct comparison with the results presented in this chapter.

7.7 Conclusion

The solvation data analysis of Chapter 5 has been expanded, resolving the solvation results in terms of the Xe – Ak distance r, which was shown in Chapter 6 to resemble the droplet radius R_D. This has been done in terms of the Poisson helium attachment model, and the dissipation of Ak^+He_N bond energy to the droplet. In the Poisson model, it is unclear if the helium attachment rate λ_{He} depends on the r. However, the lift-off time t_{lo} shows a clear r dependence, and the integration over different t_{lo} explain the linear-rise deviation from the Poisson model found in Chapter 5. In the energy dissipation, the final dissipated energy $E_{disp}(\infty)$ does not depend on r, reflecting that the solvation energy of the alkalis are local phenomena. On the other hand, the energy dissipation lifetime τ_{disp} does depend on r, suggesting that larger droplets are able to dissipate energy faster. Finally, both the Poisson model and the energy dissipation calculation gives lift-off times t_{lo} that are consistent with each other.

CHAPTER 8

Structure Determination of Alkali Heterodimers

In this chapter, I will present results determining the structure of alkali heterodimers on helium droplet surfaces. This deviates slightly from the focus of the other three result chapters, Chapter 5, Chapter 6 and Chapter 7, however, it has been included as it reflects the work I have done during my PhD and because the methods used points towards future extensions of the solvation experiment.

The results have been published in reference [3]. The analysis, results and figures of this chapter are based on reference [3].

8.1 Background

As discussed in Section 2.5 and Chapter 6, the alkali atoms and small clusters of these reside on the surface of helium droplets. The properties of the homonuclear alkali dimers on droplets have been studied by absorption spectroscopy, which find that the dimers are mainly found in the lowest-lying triplet state ($1^3\Sigma_u^+$), rather than the lower-energy singlet state ($1^1\Sigma_g^+$), but that they exhibit properties close to that of dimers in the gas phase [24, 66, 109, 110].

This result has been repeated using Coulomb explosion imaging, where the homonuclear dimer Ak_2 is doubly ionized and then fragments into two Ak^+ ions. From measuring the kinetic energy of these ions, the quantum state of the original

dimer can be determined, which also finds that the $1^3\Sigma_u^+$ state is more prevalent than the $1^1\Sigma_g^+$ state [62]. Furthermore, the same experiment extends the capabilities of the earlier spectroscopic studies by enabling the measurement of the full interatomic distance distribution of each state of the dimers, finding good agreement with theory [63]. The near instantaneous nature of the probing mechanism even enables studying laser induced dynamics of each of the quantum states of the dimers, like the alignment dynamics [61] and vibrational dynamics[1].

One limitation of the Coulomb explosion technique is that it only measures one of the created Ak^+ ions from Ak_2 dimer at a time. This is not a problem in the case of homonuclear dimers, as the undetected Ak^+ ion must have the equal and opposite momentum as the detected one, and the system is therefore well characterized. However, this is not the case of heteronuclear dimers AkAk'. Furthermore, due to the Poisson doping statistics described in Section 2.5, it is impossible to dope droplets just with the AkAk' heterodimers without also creating Ak_2 and Ak'_2 homodimers. Thereby, the measured Ak^+ ions will originate from both AkAk' and Ak_2 dimers, making the quantum states hard to distinguish, thereby also hindering the possibility of studies of the rotational and vibrational dynamics. The goal of this chapter is to mitigate these issues using coincident filtering.

8.2 Principle of the experiment

The goal of the experiment is to measure the internuclear separation (R) distribution of alkali homo- and hetero-dimers on the surfaces of helium droplets via Coulomb explosions. The alkali dimer is exposed to a focused femtosecond laser pulse, which ionizes it by multiphoton ionization, whereafter it breaks apart into two ions,

$$\mathrm{AkAk'} + N\hbar\omega \rightarrow (\mathrm{AkAk'})^{2+} + 2e^-, \tag{8.1}$$

$$(\mathrm{AkAk'})^{2+} \rightarrow \mathrm{Ak}^+ + \mathrm{Ak'}^+. \tag{8.2}$$

Note that the two valence electrons have been removed, and that the $\mathrm{AkAk'}^{2+}$ dication has closed shell structure, and is formed in only one state. Thereby, they can be described by a single repulsive potential curve, V_{dicat}. This makes alkali dimers especially good candidates for Coulomb explosion studies, compared to most other systems [102]. For the internuclear separation of the alkali dimers in

[1] Paper by N. Jyde et al. under preparation at the time of writing this thesis.

the $1^3\Sigma_u^+$ and $1^1\Sigma_g^+$ states, V_{dicat} is well approximated by a Coulomb potential,

$$V_{\text{dicat}} \approx V_{\text{Coul}} = \frac{14.4\,\text{eV}}{R(\text{Å})} + I_p(\text{Ak}) + I_p(\text{Ak'}), \tag{8.3}$$

where $I_p(\text{Ak})$ and $I_p(\text{Ak'})$ are the ionization potentials of the alkalis, and R is the internuclear distance between them.

Thereby, any given initial internuclear separation R of the dimer will lead to a kinetic energy release of $KER = 14.4\,\text{eV}/R(\text{Å})$. This one to one correspondence between KER and R forms the basis of the Coulomb explosion technique. KER has to be shared among the two alkali ions, and due to momentum conservation this sharing must obey,

$$p + p' = 0, \tag{8.4}$$

$$E + E' = \frac{p^2}{2m} + \frac{p'^2}{2m'} = KER, \tag{8.5}$$

$$\implies \frac{E}{KER} = \left(\frac{p^2}{2m}\right) / \left(\frac{p^2}{2m} + \frac{p'^2}{2m'}\right) = \frac{1}{1 + \frac{m}{m'}}, \tag{8.6}$$

where p, E and m denote the final momentum, kinetic energy and mass of the Ak^+ ion, while the prime denotes those properties for the Ak'^+ ion.

Thereby, if we measure E, and know what species the other alkali in the dimer AkAk' was, then we can reconstruct KER, and thereby R. By measuring R for many repetitions of the Coulomb explosion, the distribution of internuclear separations $P(R)$ can be measured, and this is the goal of the experiment.

What sets this experiment apart from the earlier Coulomb explosion studies of the alkali homodimers [62, 63] is the use of two body filtering to identify those Ak^+ ions that originate from a specific AkAk' dimer. Thereby, $P(R)$ can be measured for any AkAk' dimer present in the unavoidably mixed sample that is created when the droplets are doped. Furthermore, the technique can distinguish different isotopologues of the dimers, like for instance $^7\text{Li}^6\text{Li}$ from $^7\text{Li}_2$.

8.3 Experimental setup

A sketch of the experimental setup is shown in Fig. 8.1. The helium droplets were created by expanding helium at a stagnation pressure of 50 bar, and a nozzle

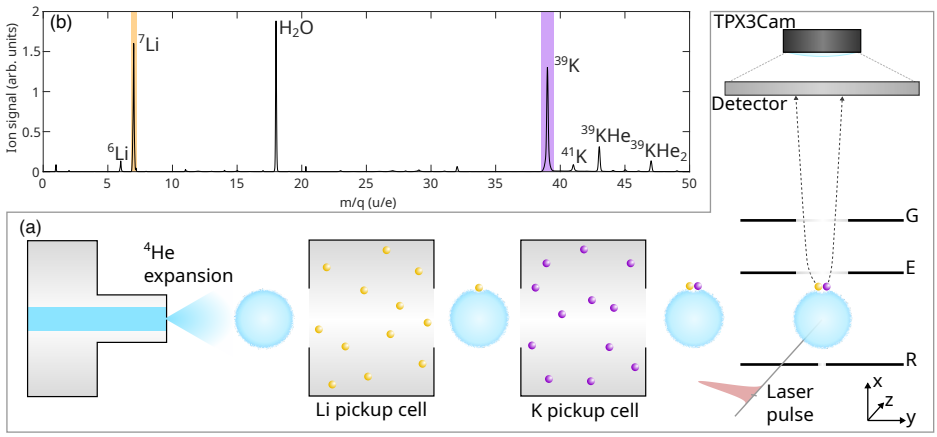

Figure 8.1: (a) Sketch of the experimental setup. Cold helium gas is expanded into vacuum to create helium droplets, which are doped with Li atoms and K atoms by passing though doping cells, creating LiK dimers. The droplets are overlapped with a fs laser pulse in the center of a VMI spectromer, and the velocity of the created Li^+ and K^+ ions are detected as positions on the MCP detector by the TPX3Cam camera. (b) an example m/q spectrum showing the presence of the different alkali isotopes in the experiment. Adapted from [3].

temperature of 16 K, giving an average droplet size of $\langle N \rangle = 9000$ atoms or $\langle R_D \rangle = 4.86\,\text{nm}$, see Section 2.4 and Table 2.1. The droplet beam passes through two oven doping cells, see Section 3.3.2, each containing an alkali sample Ak and Ak'. The vapor pressures of these cells were adjusted so that the droplets most likely pick up a single atom in each, resulting in droplets doped with the dimers AkAk', Ak_2 and Ak'_2, as well as some doped with monomers and few doped with trimers. The doped droplet beam flies through the center of a VMI spectrometer, see Section 3.5, where it is crossed by a beam of laser pulses ($\tau_p = 50\,\text{fs}$, $\lambda = 800\,\text{nm}$, $I_0 = 1.3 \times 10^{14}\,\text{W/cm}^2$), see Section 3.4. This induces a Coulomb explosion in the dimers, and the v_x and v_y velocity components of the resulting alkali ions are recorded as spatial positions on the MCP detector. Due to the use of the TPX3Cam, the TOF of each ion is recorded and the m/q ratio of each ion can be calculated. Thereby, Ak^+ and Ak'^+ ions can be distinguished, even when they originate from the same laser shot. The resulting data is a list of ion hits, with the laser shot number, v_x and v_y velocity components and m/q ratio recorded for each ion.

8.4 Doping with Li and K

In this section, data obtained while doping the droplets with Li and K atoms will be presented. This system is chosen because the energy channels in Li^+ (K^+) corresponding to the Coulomb explosion of LiK is separate from those of Li_2 (K_2), and thereby the effectiveness of the two-body coincidence filtering can be proven.

8.4.1 VMI images and kinetic energy distributions

The m/q spectrum obtained in the experiment is shown in Fig. 8.1(b), where it is seen that both ^{6}Li, ^{7}Li, ^{39}K and ^{41}K is present on the droplets. The specific alkali ions are chosen by selecting a specific m/q range, shown as colored regions in the figure. The v_x and v_y coordinates of all of these ion hits can be used to create VMI images, like what is shown in Fig. 8.2(a1, b1). In the $^7Li^+$ image, three major channels are seen. The middle one corresponds to the Coulomb explosion of the $^7Li_2$ dimer previously reported [63]. The inner one is interpreted as originating from the dissociation of singly ionized $^7Li_2{}^+$ dimers. The outermost channel only appears when the droplets are doped with both Li and K, and are postulated as originating from the Coulomb explosion of $^7Li^{39}K$ and $^7Li^{41}K$ dimers[2]. The same interpretation can be applied to the three most prevalent channels in the $^{39}K^+$ ion image. The VMI images are inverted using the POP algorithm, see Section 4.3, and calibrated, see Section 3.5.1, to give the distribution of ion kinetic energies, shown in Fig. 8.2(a2-b2).

8.4.2 Angular and radial covariance maps

To further our understanding of the peaks, we will use radial and angular covariance maps. The statistical covariance between two stochastic variables X and Y can be written as the two equivalent formulas

$$\begin{aligned} \mathrm{cov}(X,Y) &= E\left[(X-E[X])(Y-E[Y])\right] && (8.7)\\ &= E[XY]-E[X]E[Y], && (8.8) \end{aligned}$$

where $E[X]$ is the expectation value of X. That is, the covariance between the two variables express the expectation value of the product of deviation of each variable

[2]When we only look at the $^7Li^+$ data, we cannot distinguish between these two dimers.

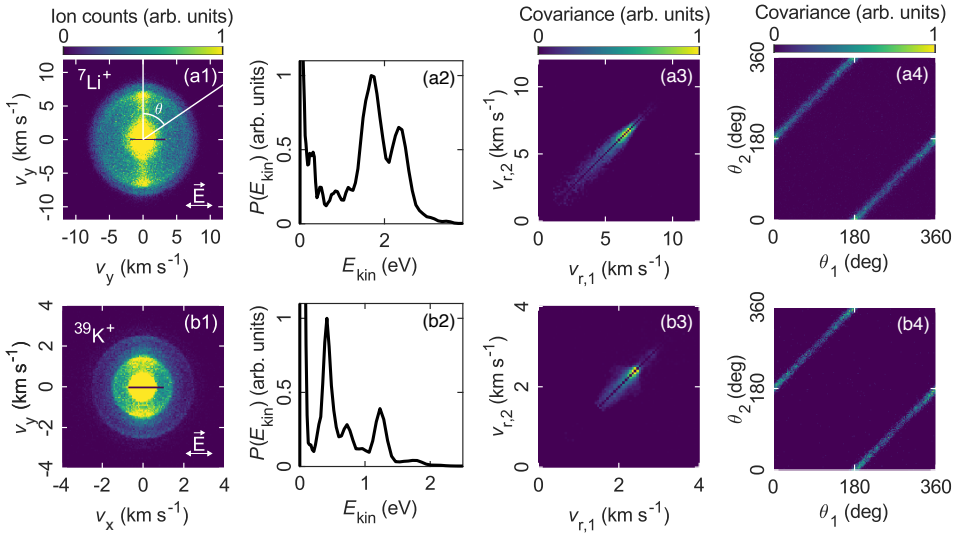

Figure 8.2: (a_1 - b_1) VMI images of the detected $^7Li^+$ and $^{39}K^+$ ions. (a_2 - b_2) Kinetic energy distributions of the same ions. (a_3 - b_3) Radial and (a_4 - b_4) angular covariance maps of the ion hits. Adapted from [3].

from its mean. The covariance is large when both variables tend to be far from their mean values at the same time.

In the use for these experiments, the variables in question are the number of ion hits per laser shot, I. These ion hits are binned along some axis, like the angle θ or radius v_r of the ion hits on the detector. Taking θ as an example, this gives an array of ion hits per laser shot

$$[I(\theta^{i=1}), I(\theta^{i=2}), I(\theta^{i=3}), ..., I(\theta^{i=n})], \tag{8.9}$$

where $I(\theta^i)$ is the number of ion hits per laser shot in the i'th θ bin, which is centered on θ^i, and n is the number of bins. From this a matrix of covariance can be created, with the (i, j)'th matrix element being

$$K_{I(\theta^i),I(\theta^j)} = E[I(\theta^i)I(\theta^j)] - E[I(\theta^i)]E[I(\theta^j)]. \tag{8.10}$$

The (i, j)'th covariance matrix element is large when there is correlation between $I(\theta^i)$ being larger than average when $I(\theta^j)$ is also larger than average.

The covariance matrix can be represented as a color map. For applied examples of this technique, see references [39, 48, 114]. Examples of angular covariance

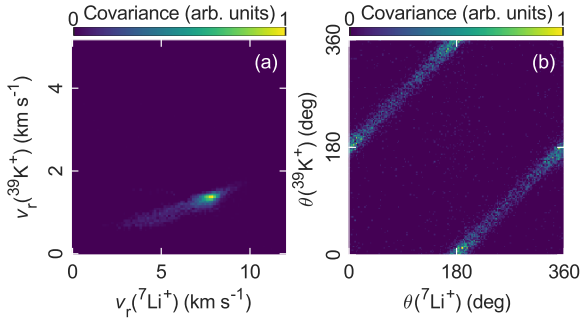

Figure 8.3: (a) Radial velocity and (b) angular covariance maps of the ion hits corresponding to $^7Li^+$ and $^{39}K^+$. Adapted from [3].

maps from the experiment can are shown in Fig. 8.2 (a_4-b_4), where θ_1 and θ_2 refers to the detector angles of two different ion hits of the same alkali species. Both of these show clear lines of covariance at $\theta_2 = \theta_1 \pm 180°$. This tells us that when we detect one $^7Li^+$ ($^{39}K^+$) ion at θ_1, then we are likely to detect another $^7Li^+$ ($^{39}K^+$) ion at $\theta_2 = \theta_1 \pm 180°$ within the same laser shot. This corresponds to the axial recoil between two ions created in the Coulomb explosion of the $^7Li_2$ ($^{39}K_2$) dimer. Furthermore, the radial covariance maps, shown in Fig. 8.2 (a_3-b_3), show that the two correlated ions appear at the same projected velocity on the detector. This velocity corresponds to the middle channel in the $^7Li^+$ images, and the outermost channel in the $^{39}K^+$ images, confirming the interpretation of these coming from the Coulomb explosion of the $^7Li_2$ and $^{39}K_2$ homodimers.

The covariance matrix can also be constructed for I for two different binnings, for instance, the angle of two different ions, like $\theta(^7Li^+)$ and $\theta(^{39}K^+)$. This is shown in Fig. 8.3(b), and once again shows a clear covariance line for $\theta(^7Li^+) = \theta(^{39}K^+) \pm 180°$. This confirms that we are creating and Coulomb exploding $^7Li^{39}K$ heterodimers.

The covariance map between $v_r(^7Li^+)$ and $v_r(^{39}K^+)$ in Fig. 8.3(a) shows a correlation that is different from that of the homodimers. To interpret this, we once again consider the momentum conservation criterion

$$p(^7Li^+) + p(^{39}K^+) = 0 \tag{8.11}$$

$$\implies v(^{39}K^+) = \frac{m(^7Li^+)}{m(^{39}K^+)} v(^7Li^+). \tag{8.12}$$

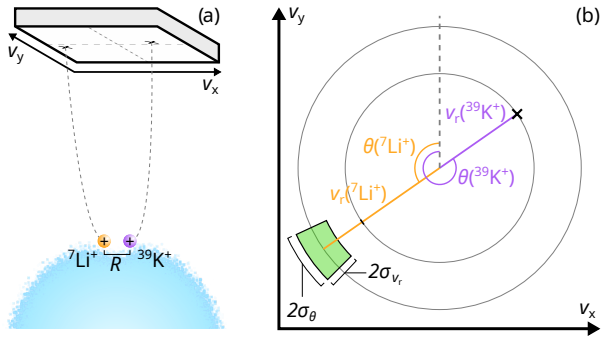

Figure 8.4: (a) Schematic showing how $^{39}K^+$ and $^7Li^+$ are detected from the Coulomb explosion of the $^7Li^{39}K$ heterodimer. (b) The principle of the coincidence filtering, the green area showing the range in which the filter looks for a $^7Li^+$ ion after detecting a $^{39}K^+$ ion at the position marked by the "x". Adapted from [3].

As this holds for the magnitudes of the velocities, it will also hold for the projected radial velocities v_r, as $v(^{39}K^+)$ and $v(^7Li^+)$ have exactly opposite directions, and are thereby equally reduced by the projection. The covariance line in Fig. 8.3(a) indeed follows this relation.

These found relations between the $^{39}K^+$ and $^7Li^+$ ion hits can be used to filter the data, keeping only those ion hits that follow the relations. This will be explained further in the next section.

8.4.3 Coincidence filtering

So far, we have been able to identify the presence of both homodimers($^7Li_2$ and $^{39}K_2$) and heterodimers ($^7Li^{39}K$) in our mixed sample on the droplets. These lead to partially overlapping channels in the $P(E_{\text{kin}})$ distributions, and we would therefore like to separate their contributions.

This is done with two-body coincidence filtering. For each ion detected, the filter looks through all other ions detected in the same laser shot, searching for ions with the diametrically opposite angle and a v_r that satisfies Eq. (8.12). As illustrated in Fig. 8.4(b) the other ion is searched for in a tolerated range, defined by the angular tolerance σ_θ and radial tolerance σ_{v_r}[3]. Thereby, the acceptance

[3]In Eq. (8.13) we see that σ_{v_r} actually has units of momentum, and should be called σ_p. This was not done to keep the notation somewhat consistent with reference [3].

criteria for the filter can be written generally for any two alkali ions as

$$-\sigma_\theta < |\theta(Ak^+) - \theta(Ak'^+)| - 180 < \sigma_\theta,$$
$$|m(Ak^+)v_r(Ak^+) - m(Ak'^+)v_r(Ak'^+)| < \sigma_{v_r}, \tag{8.13}$$

where the filter tolerances must be defined for each combination of alkali ions. The tolerances are found in practice by finding the width of the angular and radial covariance lines from plots such as those shown in Fig. 8.2(a_3-a_4) and (b_3-b_4) and Fig. 8.3.

It should be noted that the filter is a *positive identification* of two ions consistent with the Coulomb explosion of a given dimer. While random false positives from uncorrelated ion hits are possible, they are unlikely when the tolerances are kept small. Thereby, the filter can be used to extract the ions coming from any defined dimer out of the mixed sample of all the dimers, trimers, other oligomers and the isotopologues of all of these, present in the mixed ensemble on the helium droplets.

The effect of the coincidence filtering is shown in Fig. 8.5. Here it is seen that the $P(E_{\text{kin}})$ distributions of the three different dimers can be clearly separated using the filter. As a reference, $P(E_{\text{kin}})$ was obtained for $^7Li^+$ ($^{39}K^+$) ions in an experiment where the droplets were only doped with Li (K) atoms. The result, shown in Fig. 8.5(b1) ((b2)), is identical to the filtered data from the co-doped droplets, showing the filter is truly able to extract the ions that come from specific dimers. Based on this comparison, we assume that the filtering is also able to extract the ions that originate from the $^7Li^{39}K$ heterodimers.

Fig. 8.5(c1-c2) shows $P(E_{\text{kin}})$ for the $^7Li^+$ and $^{39}K^+$ ions identified as coming from the $^7Li^{39}K$ heterodimer. The fact that each $P(E_{\text{kin}})$ only has a single peak suggests that the heterodimer is only formed in a single quantum state on the droplets. The mode of the peaks are at 2.38 eV and 0.42 eV for $^7Li^+$ and $^{39}K^+$ ions respectively. This is consistent with the values 2.46 eV and 0.44 eV, which are the expected kinetic energies of the ions coming from the fragmentation of the $(^7Li^{39}K)^{2+}$ dication starting from the equilibrium distance (4.97 Å) of the triplet $1^3\Sigma_u^+$ state of the $^7Li^{39}K$ heterodimer [97]. Thereby, we have identified that the heterodimer is only formed in the triplet state on the helium droplets.

8.4.4 Distribution of internuclear distances

As the distribution of internuclear distances of the Li_2 and K_2 homodimers have previously been reported [63], we only focus on the internuclear distance distribution of the $^7Li^{39}K$ heterodimer here. As explained in Section 8.2, the kinetic energy

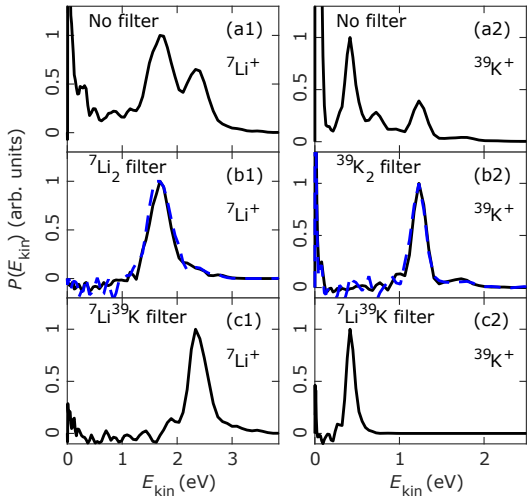

Figure 8.5: Kinetic energy distribution $P(E_{\mathrm{kin}})$ of (a1-c1) $^7Li^+$ and (a2-c2) $^{39}K^+$ are shown in black solid lines, calculated from the ions that pass through the two body filter indicated in each panel. Also shown in blue dashed lines are the $P(E_{\mathrm{kin}})$ of (b1) $^7Li^+$ and (b2) $^{39}K^+$ obtained from droplets doped only with (b1) Li or (b2) K atoms. Adapted from [3].

of either $^7Li^+$ or $^{39}K^+$ can be used to calculate the internuclear separation of the $^7Li^{39}K$ dimer they came from. The result obtained from $^7Li^+$ ions $P_{^7\mathrm{Li}}(R)$ is shown in Fig. 8.6 a red dotted line, while the results obtained from $^{39}K^+$ $P_{^{39}\mathrm{K}}(R)$ is shown in black dashed lines. For comparison, the norm square of the internuclear separation wavefunction $|\Psi(R)|^2$ is also plotted in a full blue line, calculated by solving the vibrational Schrödinger equation of the potential found in reference [97].

The modes of $P_{^7\mathrm{Li}}(R)$ and $P_{^{39}\mathrm{K}}(R)$ are 5.10 Å and 5.14 Å, respectively. This is in good agreement with the theoretical $|\Psi(R)|^2$, which has its mode at 5.05 Å. $|\Psi(R)|^2$. The magnitude of the deviation is in line with what was previously reported for the homodimers on helium droplets [63]. The FWHM of $P_{^7\mathrm{Li}}(R)$ and $P_{^{39}\mathrm{K}}(R)$ are 0.86 Å and 1.5 Å respectively. This is consistent with the $^{39}K^+$ $P(E_{\mathrm{kin}})$ peak lying at a much lower energy than the corresponding $^7Li^+$ peak, as the relative energy resolution of the VMI spectrometer is worse at lower energies.

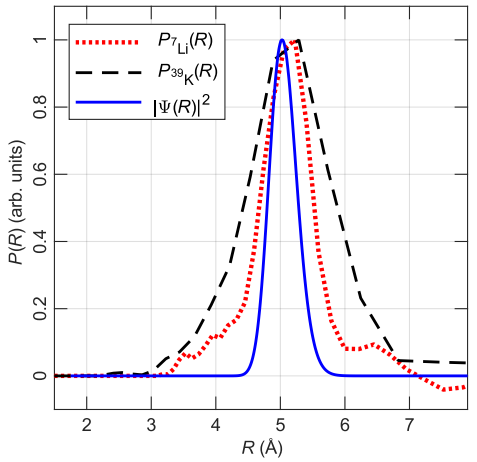

Figure 8.6: The internuclear separation distribution $P(R)$ of the $^7Li^{39}K$ dimer found from the kinetic energy distribution of $^7Li^+$ ions (red dotted line) and $^{39}K^+$ ions (black dashed line) after the application of the coincidence filter. Also shown is the theoretical square of the internuclear separation wavefunction $|\Psi(R)|^2$ for the vibrational ground state of the triplet $1^3\Sigma_u^+$ state of the $^7Li^{39}K$ dimer. Adapted from [3].

8.5 Doping with Na and K

In the previous section, it was demonstrated how the coincidence filter can be used to isolate the ion hits that come from a specific dimer, and how this enabled measuring $P(R)$ for the $^7Li^{39}K$ heterodimer. In this section, this analysis will be for a more challenging case, namely the $^{23}Na^{39}K$ heterodimer created by doping helium droplets with Na and K atoms.

The $P(E_{kin})$ distributions for the recorded $^{23}Na^+$ and $^{39}K^+$ ions, both unfiltered and using the relevant dimer filters, are shown in Fig. 8.7. The unfiltered data in Fig. 8.7(a2) gives a slight indication of two strongly overlapping peaks, while Fig. 8.7(a1) only really shows the expected singlet and triplet peaks from the Coulomb explosion of the Na_2 homodimers. We thereby see that the Coulomb explosion of the $^{23}Na^{39}K$ produces $P(E_{kin})$ distributions that overlap strongly with those from the $^{23}Na^{23}Na$, $^{39}K^{39}K$ and $^{39}K^{41}K$ dimers. This is in contrast to the case for $^7Li^{39}K$, because the masses of ^{23}Na and ^{39}K are closer than those of ^7Li and ^{39}K.

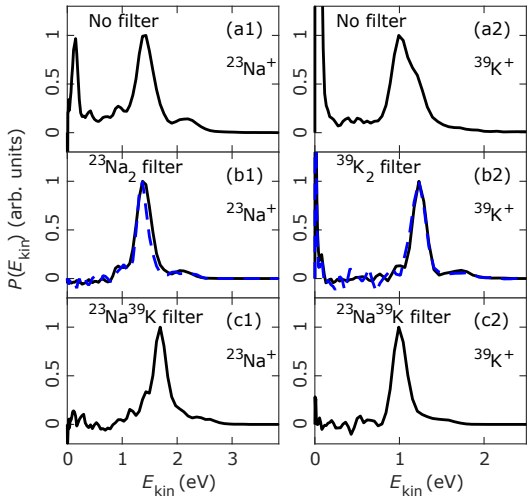

Figure 8.7: Kinetic energy distribution $P(E_{\text{kin}})$ of (a1-c1) $^{23}Na^+$ and (a2-c2) $^{39}K^+$ are shown in solid black lines, calculated using only the ions that pass through the coincidence filter indicated in each panel. Also shown in blue dashed lines are the $P(E_{\text{kin}})$ of (b1) $^{23}Na^+$ and (b2) $^{39}K^+$, obtained from droplets doped only with Na or K. Adapted from [3].

Nevertheless, we see that the coincidence filter is able to extract distinct peaks for the different dimers in Fig. 8.7(b1-c2). Once again, we compare the results from the $^{23}Na_2$ ($^{39}K_2$) filter with data obtained when the droplets were only doped with Na (K), showing that the filtered results are indeed identical to those where only the homodimers are present. When applying the $^{23}Na^{39}K$ filter, $P(E_{\text{kin}})$ for $^{23}Na^+$ in Fig. 8.7(c1) has a major peak with the mode at 1.68 eV and the suggestions of a minor peak at ∼2.5 eV. This is consistent with the theoretical values of 1.65 eV and 2.6 eV that the $^{23}Na^+$ acquires from the Coulomb explosion of $^{23}Na^{39}K$ dimers in the triplet $1^3\Sigma_u^+$ and singlet $1^1\Sigma_g^+$ states respectively [30]. $P(E_{\text{kin}})$ for the $^{39}K^+$ ions, see Fig. 8.7(c2), show a similarly good agreement with expected values for the Coulomb explosion of the $1^3\Sigma_u^+$ and $1^1\Sigma_g^+$ states of the $^{23}Na^{39}K$ dimer. Thereby, these measurements show that most $^{23}Na^{39}K$ heterodimers are formed in the triplet $1^3\Sigma_u^+$ state on the droplets, while a minority are formed in the singlet $1^1\Sigma_g^+$ state. This follows the trend that was previously established for the alkali homodimers [62].

Once again, two internuclear separation distributions for the $^{23}Na^{39}K$ dimer can be found from the $P(E_{\text{kin}})$ of either the $^{23}Na^+$ or $^{39}K^+$ ions. These are shown

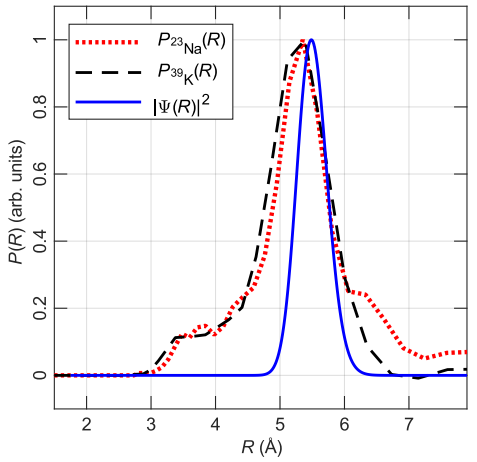

Figure 8.8: Internuclear separation distributions $P(R)$ of the $^{23}Na^{39}K$ dimer found from the kinetic energy distribution of $^{23}Na^+$ ions (red dotted line) and $^{39}K^+$ ions (black dashed line) after the application of the coincidence filter. Also shown is the square of the internuclear separation wavefunction $|\Psi(R)|^2$ for the vibrational ground state of the triplet $1^3\Sigma_u^+$ state of the $^{23}Na^{39}K$ dimer (blue solid line). Adapted from [3].

in Fig. 8.8. The modes of $P_{^{23}Na}(R)$ and $P_{^{39}K}(R)$ are 5.33 Å and 5.28 Å respectively, close to that of $|\Psi(R)|^2$ which is 5.50 Å, obtained by solving the Schrödinger equation for the potential from reference [15]. The FWHM of $P_{^{23}Na}(R)$ and $P_{^{39}K}(R)$ are 0.92 Å and 1.1 Å respectively, while that of $|\Psi(R)|^2$ is 0.55 Å. The fact that the experimental are approximately twice as wide as the theoretical one is consistent with previous results for the homodimers [63]. We once again see that $P_{^{23}Na}(R)$ for the lighter species is narrower than $P_{^{39}K}(R)$ for the heavier species. This is consistent with the energy sharing and the uncertainty of the VMI spectrometer discussed for $^7Li^{39}K$, however, the difference is smaller due to the more similar masses of ^{23}Na and ^{39}K compared to ^7Li and ^{39}K.

8.6 Conclusion and outlook

In this chapter, it has been demonstrated that two-body coincidence filtering can be used to separate ion hits according to which molecules were Coulomb exploded to

create the ions. The demonstration has been limited to the $^{7}Li^{39}K$ and $^{23}Na^{39}K$, and shows that we are able to extract the quantum state and internuclear separation distributions of these dimers. This is possible in spite of the $^{7}Li^{39}K$ ($^{23}Na^{39}K$) dimers appearing as only one possibility out of the mixed sample of the LiK, Li_2 and K_2 (NaK, Na_2 and K_2) isotopologues. For $^{23}Na^{39}K$ it has been demonstrated that even ions that strongly overlap in their kinetic energy distributions can be separated without issue. The technique can therefore easily be extended to any other alkali dimer.

Additionally, as the ion species are identified by their m/q ratio, the technique is able to perfectly separate different isotopologues. This pertains to both different isotopologues of the heterodimers, like $^{6}Li^{39}K$ and $^{7}Li^{41}K$, and to the isotopologues of the homodimers, like $^{6}Li_2$, $^{7}Li_2$ and $^{6}Li^{7}Li$.

The physical process of the Coulomb explosion happens on a femtosecond timescale, which allows the technique to be used even in pump-probe schemes measuring the time dynamics of the alkali dimers. This could be used to extend previous studies on the rotational dynamics [61]. This is especially interesting as these dynamics depend strongly on the mass of the two particles in the dimer. For instance, the rotation dynamics of the different Li_2 dimer isotopologues should be different, due to their different moments of inertia.

Lastly, the technique could be extended to other systems like alkali-metal-alkaline-earth dimers [67]. And while surface-bound species provide the cleanest ion velocities, the technique could also be used for identifying dimers formed inside the helium droplets [90, 101]. This could even be extended to a time dynamic study of dimer formation between for instance the Ak^+ ion and Xe atom used in the solvation experiment of Chapter 5, or other systems where the Xe atom is replaced by a molecule.

CHAPTER 9

Conclusion and outlook

This chapter will summarize the main results presented in the thesis, and discuss some possible future extensions of the work.

9.1 Conclusion

As presented in Chapter 5, the first steps of the solvation dynamics of alkali ions introduced into helium droplets have been measured experimentally. This novel result is realized in a femtosecond pump-probe scheme, where the pump pulse ionizes an alkali atom Ak to induce solvation, and the probe pulse ionizes a co-dopant (xenon Xe) to expel the alkali-helium solvation complex Ak^+He_n from the droplets. Thereby, the distribution of the number of helium atoms in the alkali ion solvation complex, $P_t(n)$, can be measured as a function of time. The dynamics have been quantified in two ways: A Poisson model fit to $P_t(n)$ shows good agreement, and shows that the first 5 (3, 11) helium atoms attach at a rate of $\lambda_{\mathrm{He}} = 1.8\,\mathrm{He/ps}$ ($1.8\,\mathrm{He/ps}$, $1.7\,\mathrm{He/ps}$) to Na^+ (Li^+, K^+). The measured helium attachment rates are in agreement with TDDFT simulations of the process, when compared with the buildup of helium atoms in the first and partially in the second solvation shell. The deviations from the Poisson model for larger numbers of attached helium atoms is well explained when comparing the ab-initio calculated evaporation energies E_{evap}. Under a set of assumptions about what happens to the solvation complexes after they have left the droplet surface, the average complex

binding energy dissipated from the solvation complex into the droplet $E_{\mathrm{disp}}(t)$ was measured as a function of time, and found to correspond well to the behavior expected from Newton's law of cooling.

In order to further the understanding of the co-doped helium droplets, the distance between the Xe atoms and the Ak atoms, r, was measured in Chapter 6. This was done by laser-induced Coulomb explosion, by simultaneously ionizing the Xe atom and Ak atom and measuring the kinetic energy of the created Ak^+He_n ions. The experiment was unable to measure the kinetic energy of the Xe^+ ions, for this reason, the distance r was determined from the kinetic energy of the Ak^+He_n ions alone. Comparing two assumptions about the $Xe^+ - Ak^+He_n$ momentum sharing, it was found that the Xe^+ ion seemingly moves freely inside the droplet during the Coulomb explosion. The distribution of r was found to agree well with the expected droplet radius distribution across a range of average droplet sizes, however, the effect of the Xe atom roaming within the droplet could not be disentangled in this experiment.

Chapter 7 ties together Chapter 5 and Chapter 6 by resolving the solvation results in terms of the $Xe - Ak^+He_n$ distance r. It was shown that the time-shift in the Poisson model t_{lo} is strongly dependent on r, and that integrating over a range of r in Chapter 5 could lead to the deviations from the Poisson model seen at earlier times. The helium attachment rate was strongly affected by noise in the experiment, but showed no clear dependence on r. The final amount of dissipated energy was found to be largely independent of r, while the rate at which it is dissipated had a significant r-dependence. This observation indicates that larger droplets are able to dissipate energy more quickly. All of these results are, however, limited by the amount of signal recorded, and could be improved in a repeated experiment utilizing the newly installed 5 kHz laser system to maximize the data acquisition rate.

Chapter 8 demonstrates that it is possible to extract the Coulomb explosion ion signal from specific dimers using coincident filtering, even when measuring a mixed ensemble of several different dimers. This was then used to record the internuclear distance distributions of the previously unmeasured homodimers $^7Li^{39}K$ and $^{23}Na^{39}K$. The results correspond to the expected squares of the internuclear wavefunctions to a similar degree as what has previously been reported for the homodimers. Furthermore, the technique is able to uniquely identify the isotopologues of the homo- and hetero-dimers, enabling greater accuracy in future static and dynamics Coulomb explosion studies.

9.2 Solvation of other ionic species

In Chapter 5, the experimental study of the solvation of the Li^+, Na^+ and K^+ ions in helium droplets has been presented. A natural question if the same technique could be used to measure the solvation dynamics of other ionic species. One necessity is that the neutral precursor atom for the cation must reside on the droplet surface. This limits the options to two groups of elements in the periodic system, the alkali cations and the alkaline earth cations.

9.2.1 Other alkali metals

The other alkali metals, rubidium Rb and cesium Cs[1], are known to reside on the droplet surface [10, 95, 107]. In principle, their solvation dynamics could be measured in the exact same experimental scheme as that which has been introduced in Chapter 5.

Rubidium has two naturally occurring isotopes (72% ^{85}Rb, 28% ^{87}Rb [20]), and the solvation dynamics could be measured for both. However, the maximum complex size we could measure would be $^{85}Rb^+He_9$, as $^{85}Rb^+He_{10}$ has a mass of 125 u, overlapping with the isotopes of Xe^+ we see in the mass spectrum. This would be a significant limitation of the experiment, and an alternative, heavier counter ion should probably be used. Following the trend of the lighter alkali metals, we would expect the Rb^+ $E_{\mathrm{evap}}(N)$ curve to be similar to, but with even lower E_{evap}, compared to that of K^+ shown in Fig. 5.5. Thereby, I would expect the rubidium signal to be even more heavily affected by dissociation effect than the case of K^+.

Cesium has only one naturally occurring isotope (^{133}Cs [20]), however, this puts all Cs^+He_n complexes in direct mass overlap with the Xe^+ isotopes and their helium attachments. Thereby, measuring the cesium solvation dynamics would require a much heavier co-dopant. Furthermore, binding of the helium atoms is probably even weaker than it would be for Rb^+, leading to even more dissociation.

As for alternative heavier co-dopants, xenon is the heaviest non-radioactive noble gas. However, other heavy elements could be used if the doping scheme was changed. Gold (Natural abundance 100% ^{197}Au [20]) might be a good candidate, with its high mass, non-toxicity, and an ionization potential of 9.2 eV. The slightly

[1] Note that only a few grams of francium Fr exist in the earth crust at any given time [86], and even the most stable isotope has a half life of 22 minutes. This makes Fr an unsuitable candidate for study.

lower ionization potential might even lead to a better saturation of the ionization than what we achieve for xenon. This would however require the use of a second doping oven cell, and would require a higher oven temperature than the $\sim$450 °C maximum of the current oven cell design. To achieve a vapor pressure comparable to those used for the alkalis in this thesis ($\sim 5 \times 10^{-6}$ mbar), gold would have to be heated to $\sim$1000 °C [4].

TDDFT calculations similar to those presented in Chapter 5 have already been carried out for Rb^+ and Cs^+ [40]. These calculations find a similar, but slightly slower, helium attachment rate compared to the lighter alkali ions. However, the simulations show that the heavier alkali ions plunge into the droplet before their solvation complexes are fully formed. Maybe exploring this effect experimentally could make it worthwhile to overcome the technical challenges associated with these experiments.

9.2.2 Alkaline earth metals

The Ca, Sr and Ba atoms are believed to reside on the droplet surface, while Mg atoms might be situated in a bubble just below the surface [11, 94]. Thereby, it should be possible to repeat the solvation experiment for these species, perhaps both for their singly and doubly ionized states.

From an experimental point of view, reference [94] has achieved single-atom doping of Mg, Ca, Sr and Ba by varying the temperature in a doping oven cell between 230 °C and 438 °C. This corresponds well to vapor pressures close to $\sim 5 \times 10^{-6}$ mbar [4], the same which has been used for single alkali-atom doping for the experiments presented in this thesis. The first ionization potential of the alkaline earth atoms are between 5.2 eV and 7.6 eV, still significantly lower than that of xenon atoms [60]. Thereby, the laser scheme presented in Chapter 5 could be used with minor tweaking. For the second ionization, however, the alkaline earths' ionization potential is similar to xenon's first ionization potential. For this, specific resonance enhanced multiphoton ionization (REMPI) schemes for the different alkaline earth atoms might allow the selective ionization of these without the ionization of xenon. Multiple of such resonance enhanced schemes have been found for the $Ba \longrightarrow Ba^{2+}$ transition with wavelengths in the range 280 nm to 700 nm [120], that is, within the capability of the OPAs available in our laser setup.

From a chemical point of view, this is very interesting, because it gives access to two new kinds of systems when compared to the alkali metals. Singly ionized alkaline earth atoms have an unpaired electron in their outer shell, which much change

the interaction with the helium. The helium attachments to Ca^+ have previously been measured by electron impact ionization of Ca doped helium droplets [18]. The evaporation energy curve of Ca^+He_n shows a much weaker evaporation energy than that of the alkalis [18], which could indicate that dissociation effects could limit these studies. The doubly ionized alkaline earths attract helium more strongly with their double charge. It would be very interesting to see how this changes the solvation dynamics, and thereby expand the scope of this model system of ion solvation.

9.3 Droplet diameter measurement

The Ak – Xe distance measurement presented in Chapter 6 is limited by the fact that the distance is a convolution of the droplet radius distribution and the roaming of the xenon atom inside the droplet. During a discussion with Prof. Paul Scheier at the conference QFC2024, an idea of how the droplet diameter could be measured more directly came up.

It is well known that multiple charges can coexist on the surfaces of large helium droplets [68]. These charges arrange themselves to maximize their internal distance, thereby minimizing their Coulomb repulsion, with each droplet size having a maximum number of allowable charges depending on their size. Thereby, if a droplet has two charges specifically, these two charges are expected to exist on polar opposite sides of the droplet, and the distance between them must be the droplet radius. When these charged droplets are doped, the dopants are ionized by electron transfer, conserving the location of the charge. Thereby, doubly charged droplets could be doped with Ca atoms, to create droplets on which two Ca^+ ions are located at polar opposite sides of the droplet. Furthermore, the experimental technique used to create the droplets in a specific charge state is also able to select a specific droplet size, based on the total mass-over-charge ratio of the droplet [112].

These ions could be ionized a second time by a femtosecond laser pulse, forming two Ca^{2+} ions. For a specifically selected droplet size, the repulsion between these would overcome the attraction to the droplet, creating a Coulomb explosion. The kinetic energies of the Ca^{2+} would be indicative of the distance between them, and thereby the droplet diameter, similar to what was done in Chapter 6. By controlling the selected droplet mass-over-charge ratio, which measures the number of helium atoms in the droplet, the density of the droplets could be measured, similar to what has previously been done by comparing scattering angles

and cross-sections in the same experiment [50]. Furthermore, by repeating the Ak – Xe distance measurement from Chapter 6 on droplets with the same size, the position of the Xe atom could be deduced by comparing with the measurement of the droplet diameter.

9.4 Complex formation

In the solvation experiment presented in Chapter 5, the pump-probe delay was limited to a maximum of 20 ps, where the alkali ion is still mostly on the droplet surface. After a longer time, however, the alkali ion reaches the center of the droplet [70, 71], the average location of the Xe atom. According to the TDDFT calculations, this happens on the timescale of hundreds of picoseconds [2, 40]. Thereby, one would expect the alkali ion to reach the xenon atom and form a bond with it at longer pump-probe delays. This is very interesting, because it enables measuring the time dynamics of a reaction between two species.

During the solvation experiments presented in Chapter 5, attempts at this measurement were made, simply by setting a longer pump-probe delay. Hereby, the hope was to detect some kind indication of the Coulomb explosion of a closely bound $Xe-Ak^+$ complex inside the droplets, for example by finding radial and angular covariance similar to what was shown for the alkali heterodimers in Chapter 8. This did, however, prove unsuccessful.

As of the writing of this thesis, Jeppe K. Christensen and Jean Goudot have had more luck in a slightly different system. Here droplets were doped with sodium (Na), as well dimers of benzene (Bz) or iodobenzene (IBz). With a pump pulse that selectively ionized Na and a probe pulse that ionized the co-dopant, they detected covariance between the Na^+Bz and Bz^+ signals. One reason why this only seems to work when detecting Na^+Bz-Bz^+ signals, and not $Na^+ - Bz^+$ signals, might be that the Na^+ signal spreads out over many helium attachments Na^+He_n. On the contrary, not a lot of helium attachment is seen to Na^+Bz, making it easier to detect Na^+Bz-Bz^+ covariance signals. The data even shows that the complex signal builds up over some hundreds of picoseconds before reaching a plateau. The rise-time increases with the droplet size, indicating that this is an effect of the time it takes for the Na^+ cation to reach the droplet center. These results are still very much preliminary, but also very promising, and they show that the co-doped helium droplets can be used to study more chemical reactions than just solvation.

APPENDIX A

Coordinate transformation of lognormal distributions

Because the distribution of droplet sizes from a subcritical expansion is a lognormal distribution, see Section 2.4, it is worthwhile to investigate some of the mathematical properties of this distribution.

A.1 The lognormal distribution

First, we must define what a lognormal distribution is. If a stochastic variable z follows a normal distribution, then the variable $x = \exp(z)$ follows a lognormal distribution, and has the probability density function [19, Sec. 1.3.4.7]

$$P(x;\mu,\delta) = \frac{1}{x\delta\sqrt{2\pi}} \exp\left(-\frac{(\ln(x)-\mu)^2}{2\delta^2}\right). \tag{A.1}$$

The lognormal distribution is fully described by the two parameters μ and δ. From these parameters, the mean of the distribution can be written as

$$\langle x \rangle = \exp\left(\mu + \delta^2/2\right), \tag{A.2}$$

A.2 Coordinate transformations of probability density functions

If a continuous variable x follows the probability density function $P(x)$ is transformed into a variable $y = f(x)$, then $P(y)$ will be given as

$$P(y) = \left|\frac{dx}{dy}\right| P(x(y)). \tag{A.3}$$

This is easily realized by considering that the coordinate transformation must conserve the probability within any given range, which can be expressed by the integrals

$$\int_{x_1}^{x_2} P(x)dx = \int_{f(x_1)}^{f(x_2)} P(y)dy. \tag{A.4}$$

We see that this is simply a case of integration by substitution, see reference [108, sec. 5.5], and thereby $P(y)$ must be given as in Eq. (A.3).

A.3 Transformation of lognormal distributions

In accordance to GSNS rules, I hereby state that parts of the following subsection were also used in the progress report for my qualification exam.

The transformation of the lognormal distribution when the coordinate transformation follows the formula

$$y = ax^p, \tag{A.5}$$

turns out to be especially convenient. We note immediately that a is chosen to be positive, and because x must be positive to follow a lognormal distribution, then y is also positive if it follows the above equation.

First we need to find dx/dy

$$x(y) = \left(\frac{y}{a}\right)^{1/p} \tag{A.6}$$

$$\frac{dx}{dy} = \frac{1}{pa^{1/p}} y^{\frac{1}{p}-1} \tag{A.7}$$

The lognormal probability density function of x is given by μ_x and δ_x:

$$P(x;\mu_x,\delta_x) = \frac{1}{x\delta_x\sqrt{2\pi}} \exp\left(-\frac{(\ln(x)-\mu_x)^2}{2\delta_x^2}\right) \tag{A.8}$$

By using Eq. (A.3), we can find the distribution of y as

$$P(y;\mu_y,\delta_y) = \left|\frac{1}{pa^{1/p}} y^{\frac{1}{p}-1}\right| \frac{1}{\left(\frac{y}{a}\right)^{1/p}\delta_x\sqrt{2\pi}} \exp\left(-\frac{\left(\ln\left(\left(\frac{y}{a}\right)^{1/p}\right)-\mu_x\right)^2}{2\delta_x^2}\right) \tag{A.9}$$

$$= \left|\frac{1}{yp}\right| \frac{1}{\left(\delta_x\sqrt{2\pi}\right)} \exp\left(-\frac{\left(\frac{1}{p}(\ln(y)-\ln(a))-\mu_x\right)^2}{2\delta_x^2}\right) \tag{A.10}$$

$$= \frac{1}{\left(y\left(|p|\delta_x\right)\sqrt{2\pi}\right)} \exp\left(-\frac{1}{p^2}\frac{((\ln(y)-\ln(a))-p\mu_x)^2}{2\delta_x^2}\right) \tag{A.11}$$

$$= \frac{1}{\left(y\left(|p|\delta_x\right)\sqrt{2\pi}\right)} \exp\left(-\frac{\left(\ln(y)-(p\mu_x+\ln(a))\right)^2}{2\left(|p|\delta_x\right)^2}\right) \tag{A.12}$$

The result here is that y also follows a lognormal distribution, as we can see by comparing the above result with A.8. So, in conclusion, when y is given as $y = ax^p$, and x follows a lognormal distribution with variables δ_x and μ_x, then y also follows a lognormal distribution with the variables

$$\delta_y = |p|\delta_x, \tag{A.13}$$

$$\mu_y = p\mu_x + \ln(a). \tag{A.14}$$

A.3.1 Mean of transformed lognormal distribution

The mean of the variable $y = ax^p$ that follows the transformed lognormal distribution $P(y; \mu_y, \delta_y)$ can be found using Eq. (A.2) to be

$$\langle y \rangle = \exp\left(\mu_y + \frac{(\delta_y)^2}{2}\right) \tag{A.15}$$

$$= \exp\left(p\mu_x + \ln(a) + \frac{(|p|\delta_x)^2}{2}\right) \tag{A.16}$$

$$= a\exp\left(p\mu_x + p^2\frac{\delta_x^2}{2}\right) \tag{A.17}$$

$$= a\exp\left(\mu_x + \frac{\delta_x^2}{2}\right)^p \exp\left(\frac{\delta_x^2}{2}\right)^p \tag{A.18}$$

$$\implies \langle y \rangle = a\langle x \rangle^p \exp\left(\frac{\delta_x^2}{2}\right)^p. \tag{A.19}$$

Unfortunately, we see that the average does not simply follow $\langle y \rangle = a\langle x \rangle^p$, due to the lognormal distribution being asymmetrical about the mean. However, we see that the deviation is only the simple correction $\exp(\delta_x^2/2)^p$.

Bibliography

[1] A. F. Al-Refaie, M. Johny, J. Correa, D. Pennicard, P. Svihra, A. Nomerotski, S. Trippel, and J. Küpper. PymePix: A python library for SPIDR readout of Timepix3. *Journal of Instrumentation*, 14(10):P10003–P10003, October 2019. ISSN 1748-0221. doi: 10.1088/1748-0221/14/10/P10003. 47

[2] Simon H. Albrechtsen, Constant A. Schouder, Alberto Viñas Muñoz, Jeppe K. Christensen, Christian Engelbrecht Petersen, Martí Pi, Manuel Barranco, and Henrik Stapelfeldt. Observing the primary steps of ion solvation in helium droplets. *Nature*, 623(7986):319–323, November 2023. ISSN 1476-4687. doi: 10.1038/s41586-023-06593-5. vi, 21, 57, 60, 61, 62, 64, 65, 68, 70, 73, 75, 77, 85, 115, 156

[3] Simon H Albrechtsen, Jeppe K. Christensen, Rico Mayro P. Tanyag, Henrik H. Kristensen, and Henrik Stapelfeldt. Laser-induced Coulomb explosion of heteronuclear alkali-metal dimers on helium nanodroplets. *Phys. Rev. A*, 109:043112, 2024. doi: 10.1103/PhysRevA.109.043112. 137, 140, 142, 143, 144, 146, 147, 148, 149

[4] C. B. Alcock, V. P. Itkin, and M. K. Horrigan. Vapour Pressure Equations for the Metallic Elements: 298–2500K. *Canadian Metallurgical Quarterly*, 23 (3):309–313, July 1984. ISSN 0008-4433. doi: 10.1179/cmq.1984.23.3.309. 30, 154

[5] D. R. Allum, P. V. E. McClintock, and A. Phillips. The Breakdown of Superfluidity in Liquid ^{4}He: An Experimental Test of Landau's Theory. *Philosophical Transactions of the Royal Society of London. Series A, Mathematical and Physical Sciences*, 284(1320):179–224, January 1977. doi: 10.1098/rsta.1977.0008. 11

[6] Amsterdam Scientific Instruments (ASI). Technology. https://www.amscins.com/resources/technology/. 47

[7] Lukas An Der Lan, Peter Bartl, Christian Leidlmair, Harald Schöbel, Roland Jochum, Stephan Denifl, Tilmann D. Märk, Andrew M. Ellis, and Paul Scheier. The submersion of sodium clusters in helium nanodroplets: Identification of the surface $\rightarrow$ interior transition. *The Journal of Chemical Physics*, 135(4):044309, July 2011. ISSN 0021-9606, 1089-7690. doi: 10.1063/1.3610388. 20

[8] Lukas An der Lan, Peter Bartl, Christian Leidlmair, Roland Jochum, Stephan Denifl, Olof Echt, and Paul Scheier. Solvation of Na+, K+, and Their Dimers in Helium. *Chemistry – A European Journal*, 18(14):4411–4418, April 2012. ISSN 0947-6539. doi: 10.1002/chem.201103432. 4, 58

[9] Lukas An Der Lan, Peter Bartl, Christian Leidlmair, Harald Schöbel, Stephan Denifl, Tilmann D. Märk, Andrew M. Ellis, and Paul Scheier. Submersion of potassium clusters in helium nanodroplets. *Physical Review B*, 85(11):115414, March 2012. ISSN 1098-0121, 1550-235X. doi: 10.1103/PhysRevB.85.115414. 20

[10] Francesco Ancilotto, Peter B. Lerner, and Milton W. Cole. Physics of solvation. *Journal of Low Temperature Physics*, 101(5-6):1123–1146, December 1995. ISSN 0022-2291, 1573-7357. doi: 10.1007/BF00754527. 4, 20, 60, 153

[11] Francesco Ancilotto, Manuel Barranco, François Coppens, Jussi Eloranta, Nadine Halberstadt, Alberto Hernando, David Mateo, and Martí Pi. Density functional theory of doped superfluid liquid helium and nanodroplets. *International Reviews in Physical Chemistry*, 36(4):621–707, October 2017. ISSN 0144-235X. doi: 10.1080/0144235X.2017.1351672. 21, 154

[12] Selby Angus and K. M. de Reuck. *International Thermodynamic Tables of the Fluid State, Helium-4, 1975*. Pergamon Press, London Elmsford, N.Y, 1st ed edition, 1976. ISBN 978-0-08-020957-9. 10, 12

[13] P. W. Atkins, Julio De Paula, and James Keeler. *Atkins' Physical Chemistry*. Oxford University Press, Oxford, United Kingdom ; New York, NY, eleventh edition edition, 2018. ISBN 978-0-19-876986-6. 19

[14] Slim Awali, Lionel Poisson, Benoît Soep, Marc-André Gaveau, Marc Briant, Christophe Pothier, Jean-Michel Mestdagh, Mounir Ben El Hadj Rhouma, Majdi Hochlaf, Vincent Mazet, and Sylvain Faisan. Time resolved observation of the solvation dynamics of a Rydberg excited molecule deposited on an argon cluster-I: DABCO* at short times. *Physical Chemistry Chemical Physics*, 16(2):516–526, December 2013. ISSN 1463-9084. doi: 10.1039/C3CP53172D. 60

[15] M. Aymar and O. Dulieu. Calculations of transition and permanent dipole moments of heteronuclear alkali dimers NaK, NaRb and NaCs. *Molecular Physics*, 105(11-12):1733–1742, June 2007. ISSN 0026-8976, 1362-3028. doi: 10.1080/00268970701494016. 149

[16] M. Barranco, F. Garcias, Ll. Serra, and M. Casas. The Structure and Response of Doped 3He Clusters. *Journal of Low Temperature Physics*, 113 (3/4):381–386, 1998. ISSN 00222291. doi: 10.1023/A:1022527506771. 58

[17] Manuel Barranco, Rafael Guardiola, Susana Hernández, Ricardo Mayol, Jesús Navarro, and Martí Pi. Helium Nanodroplets: An Overview. *Journal of Low Temperature Physics*, 142(1-2):1–81, January 2006. ISSN 0022-2291, 1573-7357. doi: 10.1007/s10909-005-9267-0. 60

[18] Massimiliano Bartolomei, Paul Martini, Ricardo Pérez de Tudela, Tomás González-Lezana, Marta I. Hernández, José Campos-Martínez, Javier Hernández-Rojas, José Bretón, and Paul Scheier. Ca+ Ions Solvated in Helium Clusters. *Molecules*, 26(12):3642, January 2021. ISSN 1420-3049. doi: 10.3390/molecules26123642. 58, 155

[19] Olaf Behnke, Kevin Kröninger, Grégory Schott, and Thomas Schörner-Sadenius, editors. *Data Analysis in High Energy Physics: A Practical Guide to Statistical Methods*. Wiley-VCH Verlag GmbH & Co. KGaA, Weinheim, Germany, 2013. ISBN 978-3-527-41058-3. 71, 157

[20] Michael Berglund and Michael E. Wieser. Isotopic compositions of the elements 2009 (IUPAC Technical Report). *Pure and Applied Chemistry*, 83 (2):397–410, January 2011. ISSN 1365-3075, 0033-4545. doi: 10.1351/PAC-REP-10-06-02. 9, 153

[21] Andreas Braun. *Photodissociation Studies of CH_3I and CF_3I in Fluid ^{4}Helium Nanodroplets*. PhD thesis, École Polytechnique Fédérale de Lausanne, 2004. 14, 16, 17

[22] Marc Briant, Jean-Michel Mestdagh, Marc-André Gaveau, and Lionel Poisson. Reaction dynamics within a cluster environment. *Physical Chemistry Chemical Physics*, 24(17):9807–9835, May 2022. ISSN 1463-9084. doi: 10.1039/D1CP05783A. 60

[23] Hubertus Bromberger, Christopher Passow, David Pennicard, Rebecca Boll, Jonathan Correa, Lanhai He, Melby Johny, Christina C. Papadopoulou, Atia Tul-Noor, Joss Wiese, Sebastian Trippel, Benjamin Erk, and Jochen Küpper. Shot-by-shot 250 kHz 3D ion and MHz photoelectron imaging using Timepix3. *Journal of Physics B: Atomic, Molecular and Optical Physics*, 55 (14):144001, June 2022. ISSN 0953-4075. doi: 10.1088/1361-6455/ac6b6b. 47, 50

[24] F. R. Brühl, R. A. Miron, and W. E. Ernst. Triplet states of rubidium dimers on helium nanodroplets. *The Journal of Chemical Physics*, 115(22):10275, 2001. ISSN 00219606. doi: 10.1063/1.1418747. 137

[25] David W. Chandler and Paul L. Houston. Two-dimensional imaging of state-selected photodissociation products detected by multiphoton ionization. *The Journal of Chemical Physics*, 87(2):1445–1447, July 1987. ISSN 0021-9606, 1089-7690. doi: 10.1063/1.453276. 41

[26] C.E. Chase, E. Maxwell, and W.E. Millett. The dielectric constant of liquid helium. *Physica*, 27(12):1129–1145, December 1961. ISSN 00318914. doi: 10.1016/0031-8914(61)90054-4. 12

[27] Adam S. Chatterley, Lars Christiansen, Constant A. Schouder, Anders V. Jørgensen, Benjamin Shepperson, Igor N. Cherepanov, Giacomo Bighin, Robert E. Zillich, Mikhail Lemeshko, and Henrik Stapelfeldt. Rotational Coherence Spectroscopy of Molecules in Helium Nanodroplets: Reconciling the Time and the Frequency Domains. *Physical Review Letters*, 125(1): 013001, July 2020. doi: 10.1103/PhysRevLett.125.013001. 58

[28] M. Y. Choi, G. E. Douberly, T. M. Falconer, W. K. Lewis, C. M. Lindsay, J. M. Merritt, P. L. Stiles, and R. E. Miller. Infrared spectroscopy of helium

nanodroplets: Novel methods for physics and chemistry. *International Reviews in Physical Chemistry*, 25(1):15, 2006. ISSN 0144-235X. doi: 10.1080/01442350600625092. 58

[29] J.S. Coursey, D.J. Schwab, J.J. Tsai, and Dragoset. Atomic Weights and Isotopic Compositions (version 4.1), 2015. 91, 107

[30] Johannes Deiglmayr, Mireille Aymar, Roland Wester, Matthias Weidemüller, and Olivier Dulieu. Calculations of static dipole polarizabilities of alkali dimers: Prospects for alignment of ultracold molecules. *The Journal of Chemical Physics*, 129(6):064309, August 2008. ISSN 0021-9606. doi: 10.1063/1.2960624. 148

[31] Bernhard Dick. Inverting ion images without Abel inversion: Maximum entropy reconstruction of velocity maps. *Phys. Chem. Chem. Phys.*, 16(2): 570–580, 2014. ISSN 1463-9076, 1463-9084. doi: 10.1039/C3CP53673D. 67, 91, 122

[32] Gary E. Douberly and Roger E. Miller. Rotational Dynamics of HCN-M (M = Na, K, Rb, Cs) van der Waals Complexes Formed on the Surface of Helium Nanodroplets. *The Journal of Physical Chemistry A*, 111(31): 7292–7302, August 2007. ISSN 1089-5639. doi: 10.1021/jp070042a. 119

[33] G. Droppelmann, O. Bünermann, C. P. Schulz, and F. Stienkemeier. Formation Times of RbHe Exciplexes on the Surface of Superfluid versus Normal Fluid Helium Nanodroplets. *Physical Review Letters*, 93(2):023402, July 2004. doi: 10.1103/PhysRevLett.93.023402. 62

[34] Eksma Optics. BBO – BETA BARIUM BORATE Datasheet, October 2022. 34

[35] André T. J. B Eppink and David H. Parker. Velocity map imaging of ions and electrons using electrostatic lenses: Application in photoelectron and photofragment ion imaging of molecular oxygen. *Review of Scientific Instruments*, 68(9):3477–3484, 1997. doi: 10.1063/1.1148310. 41, 43

[36] Martin Ester, Hans-Peter Kriegel, Jörg Sander, and Xiaowei Xu. A Density-Based Algorithm for Discovering Clusters in Large Spatial Databases with Noise. In *Proceedings of 2nd International Conference on Knowledge Discovery and Data Mining (KDD-96)*, Portland, Oregon, USA, 1996. 49

[37] K. Fehre, D. Trojanowskaja, J. Gatzke, M. Kunitski, F. Trinter, S. Zeller, L. Ph. H. Schmidt, J. Stohner, R. Berger, A. Czasch, O. Jagutzki, T. Jahnke, R. Dörner, and M. S. Schöffler. Absolute ion detection efficiencies of microchannel plates and funnel microchannel plates for multi-coincidence detection. *Review of Scientific Instruments*, 89(4):045112, April 2018. ISSN 0034-6748, 1089-7623. doi: 10.1063/1.5022564. 46

[38] M. Fisher-Levine and A. Nomerotski. TimepixCam: A fast optical imager with time-stamping. *Journal of Instrumentation*, 11(03):C03016, March 2016. ISSN 1748-0221. doi: 10.1088/1748-0221/11/03/C03016. 47

[39] Leszek J. Frasinski. Covariance mapping techniques. *Journal of Physics B: Atomic, Molecular and Optical Physics*, 49(15):152004, 2016. ISSN 0953-4075. doi: 10.1088/0953-4075/49/15/152004. 142

[40] Ernesto García-Alfonso, Manuel Barranco, Nadine Halberstadt, and Martí Pi. Time-resolved solvation of alkali ions in superfluid helium nanodroplets. *The Journal of Chemical Physics*, 160(16):164308, April 2024. ISSN 0021-9606. doi: 10.1063/5.0205951. 3, 21, 60, 62, 89, 92, 96, 97, 115, 116, 133, 136, 154, 156

[41] W. E. Gifford and R. C. Longsworth. Surface Heat Pumping. In K. D. Timmerhaus, editor, *Advances in Cryogenic Engineering*, pages 171–179. Springer US, Boston, MA, 1966. ISBN 978-1-4757-0524-9 978-1-4757-0522-5. doi: 10.1007/978-1-4757-0522-5_18. 27

[42] Tomás González-Lezana and and group. Evaporation energy of Na+ and K+ in helium, February 2024. 71, 72

[43] Tomás González-Lezana, Olof Echt, Michael Gatchell, Massimiliano Bartolomei, José Campos-Martínez, and Paul Scheier. Solvation of ions in helium. *International Reviews in Physical Chemistry*, 39(4):465–516, October 2020. ISSN 0144-235X. doi: 10.1080/0144235X.2020.1794585. 4, 58

[44] Susan T. Graul and Michael T. Bowers. Vibrational Excitation in Products of Nucleophilic Substitution: The Dissociation of Metastable X-(CH3Y) in the Gas Phase. *Journal of the American Chemical Society*, 116(9):3875–3883, May 1994. ISSN 0002-7863, 1520-5126. doi: 10.1021/ja00088a024. 77

[45] Slava Grebenev, J. Peter Toennies, and Andrei F. Vilesov. Superfluidity Within a Small Helium-4 Cluster: The Microscopic Andronikashvili Experiment. *Science*, 279(5359):2083–2086, March 1998. doi: 10.1126/science.279.5359.2083. 12, 58

[46] David J. Griffiths. *Introduction to Electrodynamics*. Cambridge University Press, Cambridge, United Kingdom ; New York, NY, fourth edition edition, 2018. ISBN 978-1-108-42041-9. 101, 107

[47] Hamamatsu. MCP and MCP assembly, January 2016. 46

[48] Jonas L Hansen, Jens H Nielsen, Christian Bruun Madsen, Anders Thyboe Lindhardt, Mikael P Johansson, Troels Skrydstrup, Lars Bojer Madsen, and Henrik Stapelfeldt. Control and femtosecond time-resolved imaging of torsion in a chiral molecule. *The Journal of Chemical Physics*, 136(20):204310–204310–10, May 2012. ISSN 00219606. doi: 10.1063/1.4719816. 142

[49] Jan Harms, Matthias Hartmann, J.Peter Toennies, Andrei F. Vilesov, and Boris Sartakov. Rotational Structure of the IR Spectra of Single SF6Molecules in Liquid4He and3He Droplets. *Journal of Molecular Spectroscopy*, 185(1):204–206, September 1997. ISSN 00222852. doi: 10.1006/jmsp.1997.7343. 58

[50] Jan Harms, J. Peter Toennies, and Franco Dalfovo. Density of superfluid helium droplets. *Physical Review B*, 58(6):3341–3350, August 1998. ISSN 0163-1829, 1095-3795. doi: 10.1103/PhysRevB.58.3341. 13, 14, 15, 16, 156

[51] Matthias Hartmann, Nikolas Pörtner, Boris Sartakov, J. Peter Toennies, and Andrei F. Vilesov. High resolution infrared spectroscopy of single SF6 molecules in helium droplets. I. Size effects in He4 droplets. *The Journal of Chemical Physics*, 110(11):5109–5123, March 1999. ISSN 0021-9606, 1089-7690. doi: 10.1063/1.479111. 12

[52] P.G. Hoel, S.C. Port, and C.J. Stone. *Introduction to Probability Theory*. Houghton Mifflin Series in Statistics. Houghton Mifflin, 1971. ISBN 978-0-395-04636-4. 106

[53] Kyung Hwan Kim, Jeongho Kim, Jae Hyuk Lee, and Hyotcherl Ihee. Topical Review: Molecular reaction and solvation visualized by time-resolved X-ray solution scattering: Structure, dynamics, and their solvent dependence. *Structural Dynamics*, 1(1):011301, January 2014. doi: 10.1063/1.4865234. 3

[54] Wlodzimierz Jarzeba, Gilbert C. Walker, Alan E. Johnson, Michael A. Kahlow, and Paul F. Barbara. Femtosecond microscopic solvation dynamics of aqueous solutions. *The Journal of Physical Chemistry*, 92(25):7039–7041, December 1988. ISSN 0022-3654. doi: 10.1021/j100336a002. 3, 59

[55] Ralph Jimenez, Graham R. Fleming, P. V. Kumar, and M. Maroncelli. Femtosecond solvation dynamics of water. *Nature*, 369(6480):471–473, June 1994. ISSN 1476-4687. doi: 10.1038/369471a0. 3

[56] Michael A. Kahlow, Wl/odzimierz Jarzęba, Thomas P. DuBruil, and Paul F. Barbara. Ultrafast emission spectroscopy in the ultraviolet by time-gated upconversion. *Review of Scientific Instruments*, 59(7):1098–1109, July 1988. ISSN 0034-6748, 1089-7623. doi: 10.1063/1.1139734. 3, 59

[57] P. Kapitza. Viscosity of Liquid Helium below the λ-Point. *Nature*, 141 (3558), January 1938. ISSN 0028-0836. doi: 10.1038/141074a0. 11

[58] Ursula Keller. *Ultrafast Lasers: A Comprehensive Introduction to Fundamental Principles with Practical Applications*. Graduate Texts in Physics. Springer International Publishing, Cham, 2021. ISBN 978-3-030-82531-7 978-3-030-82532-4. doi: 10.1007/978-3-030-82532-4. 37

[59] Kyung Hwan Kim, Jong Goo Kim, Shunsuke Nozawa, Tokushi Sato, Key Young Oang, Tae Wu Kim, Hosung Ki, Junbeom Jo, Sungjun Park, Changyong Song, Takahiro Sato, Kanade Ogawa, Tadashi Togashi, Kensuke Tono, Makina Yabashi, Tetsuya Ishikawa, Joonghan Kim, Ryong Ryoo, Jeongho Kim, Hyotcherl Ihee, and Shin-ichi Adachi. Direct observation of bond formation in solution with femtosecond X-ray scattering. *Nature*, 518(7539):385–389, February 2015. ISSN 1476-4687. doi: 10.1038/nature14163. 3

[60] A. Kramida, Yu. Ralchenko, J. Reader, and and NIST ASD Team. NIST Atomic Spectra Database (ver. 5.11). NIST Atomic Spectra Database (ver.

5.11), [Online]. Available: <tt>https://physics.nist.gov/asd</tt> [2016, January 31]. National Institute of Standards and Technology, Gaithersburg, MD., 2023. 9, 63, 99, 154

[61] Lorenz Kranabetter, Henrik H. Kristensen, Areg Ghazaryan, Constant A. Schouder, Adam S. Chatterley, Paul Janssen, Frank Jensen, Robert E. Zillich, Mikhail Lemeshko, and Henrik Stapelfeldt. Nonadiabatic Laser-Induced Alignment Dynamics of Molecules on a Surface. *Physical Review Letters*, 131(5):053201, August 2023. doi: 10.1103/PhysRevLett.131.053201. 138, 150

[62] Henrik H. Kristensen, Lorenz Kranabetter, Constant A. Schouder, Christoph Stapper, Jacqueline Arlt, Marcel Mudrich, and Henrik Stapelfeldt. Quantum-State-Sensitive Detection of Alkali Dimers on Helium Nanodroplets by Laser-Induced Coulomb Explosion. *Physical Review Letters*, 128(9):093201, March 2022. ISSN 0031-9007, 1079-7114. doi: 10.1103/PhysRevLett.128.093201. 5, 67, 104, 122, 138, 139, 148

[63] Henrik H. Kristensen, Lorenz Kranabetter, Constant A. Schouder, Jacqueline Arlt, Frank Jensen, and Henrik Stapelfeldt. Laser-induced Coulomb explosion imaging of alkali-metal dimers on helium nanodroplets. *Physical Review A*, 107(2):023104, February 2023. doi: 10.1103/PhysRevA.107.023104. 5, 138, 139, 141, 145, 146, 149

[64] Tatu Kumpulainen, Bernhard Lang, Arnulf Rosspeintner, and Eric Vauthey. Ultrafast Elementary Photochemical Processes of Organic Molecules in Liquid Solution. *Chemical Reviews*, 117(16):10826–10939, August 2017. ISSN 0009-2665. doi: 10.1021/acs.chemrev.6b00491. 3

[65] Yongkyung Kwon, Patrick Huang, Mehul V. Patel, Dörte Blume, and K. Birgitta Whaley. Quantum solvation and molecular rotations in superfluid helium clusters. *The Journal of Chemical Physics*, 113(16):6469, 2000. ISSN 00219606. doi: 10.1063/1.1310608. 58

[66] Florian Lackner, Johannes Poms, Günter Krois, Johann V. Pototschnig, and Wolfgang E. Ernst. Spectroscopy of Lithium Atoms and Molecules on Helium Nanodroplets. *The Journal of Physical Chemistry A*, 117(46):11866–11873, November 2013. ISSN 1089-5639. doi: 10.1021/jp4030238. 137

[67] Florian Lackner, Günter Krois, Thomas Buchsteiner, Johann V. Pototschnig, and Wolfgang E. Ernst. Helium-Droplet-Assisted Preparation of Cold RbSr Molecules. *Physical Review Letters*, 113(15):153001, October 2014. doi: 10.1103/PhysRevLett.113.153001. 150

[68] Felix Laimer, Lorenz Kranabetter, Lukas Tiefenthaler, Simon Albertini, Fabio Zappa, Andrew M. Ellis, Michael Gatchell, and Paul Scheier. Highly Charged Droplets of Superfluid Helium. *Physical Review Letters*, 123 (16):165301, October 2019. ISSN 0031-9007, 1079-7114. doi: 10.1103/PhysRevLett.123.165301. 155

[69] L. Landau. Theory of the superfluidity of helium II. *Physical Review*, 60(4): 356–358, August 1941. ISSN 0031-899X. doi: 10.1103/PhysRev.60.356. 11

[70] Antonio Leal, David Mateo, Alberto Hernando, Martí Pi, Manuel Barranco, Alessandro Ponti, Fausto Cargnoni, and Marcel Drabbels. Picosecond solvation dynamics of alkali cations in superfluid $^{4}\mathrm{He}$ nanodroplets. *Physical Review B*, 90(22):224518, December 2014. doi: 10.1103/PhysRevB.90.224518. 60, 156

[71] Antonio Leal, Xiaohang Zhang, Manuel Barranco, Fausto Cargnoni, Alberto Hernando, David Mateo, Massimo Mella, Marcel Drabbels, and Martí Pi. Dynamics of photoexcited Ba+ cations in 4He nanodroplets. *The Journal of Chemical Physics*, 144(9):094302, March 2016. ISSN 0021-9606. doi: 10.1063/1.4942850. 156

[72] R. T. Learn, E. Varga, V. Vadakkumbatt, and J. P. Davis. Precision measurements of the zero-temperature dielectric constant and density of liquid He 4. *Physical Review B*, 106(21):214509, December 2022. ISSN 2469-9950, 2469-9969. doi: 10.1103/PhysRevB.106.214509. 12

[73] Kevin K. Lehmann. Potential of a neutral impurity in a large 4He cluster. *Molecular Physics*, 97(5):645–666, September 1999. ISSN 0026-8976. doi: 10.1080/002689799163497. 118

[74] M. Lewerenz, B. Schilling, and J. P. Toennies. A new scattering deflection method for determining and selecting the sizes of large liquid clusters of 4He. *Chemical Physics Letters*, 206(1–4):381–387, April 1993. ISSN 0009-2614. doi: 10.1016/0009-2614(93)85569-A. 13

[75] X. Li, A. Rudenko, M. S. Schöffler, N. Anders, Th. M. Baumann, S. Eckart, B. Erk, A. De Fanis, K. Fehre, R. Dörner, L. Foucar, S. Grundmann, P. Grychtol, A. Hartung, M. Hofmann, M. Ilchen, Ch. Janke, G. Kastirke, M. Kircher, K. Kubicek, M. Kunitski, T. Mazza, S. Meister, N. Melzer, J. Montano, V. Music, G. Nalin, Y. Ovcharenko, Ch. Passow, A. Pier, N. Rennhack, J. Rist, D. E. Rivas, I. Schlichting, L. Ph. H. Schmidt, Ph. Schmidt, J. Siebert, N. Strenger, D. Trabert, F. Trinter, I. Vela-Perez, R. Wagner, P. Walter, M. Weller, P. Ziolkowski, A. Czasch, D. Rolles, M. Meyer, T. Jahnke, and R. Boll. Coulomb explosion imaging of small polyatomic molecules with ultrashort x-ray pulses. *Physical Review Research*, 4(1):013029, January 2022. doi: 10.1103/PhysRevResearch.4.013029. 100

[76] Yizhak Marcus. *Ions in Solution and Their Solvation*. Wiley, 1 edition, August 2015. ISBN 978-1-118-88914-5 978-1-118-89233-6. doi: 10.1002/9781118892336. 58, 59

[77] A. Masson, L. Poisson, M.-A. Gaveau, B. Soep, J.-M. Mestdagh, V. Mazet, and F. Spiegelman. Dynamics of highly excited barium atoms deposited on large argon clusters. I. General trends. *The Journal of Chemical Physics*, 133(5):054307, August 2010. ISSN 0021-9606. doi: 10.1063/1.3464489. 60

[78] Peter W. Milonni and Joseph H. Eberly. *Laser Physics*. John Wiley & Sons, April 2010. ISBN 978-0-470-40970-1. 34

[79] John H. Moore, Christopher C. Davis, and Michael A. Coplan. *Building Scientific Apparatus*. Cambridge University Press, Leiden, 4th ed edition, 2009. ISBN 978-0-511-58009-3. 25, 26

[80] M. Mudrich, F. Stienkemeier, G. Droppelmann, P. Claas, and C. P. Schulz. Quantum Interference Spectroscopy of Rubidium-Helium Exciplexes Formed on Helium Nanodroplets. *Physical Review Letters*, 100 (2):023401, January 2008. ISSN 0031-9007, 1079-7114. doi: 10.1103/PhysRevLett.100.023401. 63

[81] S. Müller, M. Mudrich, and F. Stienkemeier. Alkali-helium snowball complexes formed on helium nanodroplets. *The Journal of Chemical Physics*, 131(4):044319, July 2009. ISSN 0021-9606. doi: 10.1063/1.3180819. 59

[82] Adi Natan. Polaronionpeeling (`https://github.com/adinatan/PolarOnionPeeling`), github, 2024. 54

[83] National Institute of Standards and Technology. Computational Chemistry Comparison and Benchmark DataBase. http://cccbdb.nist.gov/. 21

[84] Newport. UTM Series Mid-Range Travel Translation Stages, June 1997. 33

[85] Andrei Nomerotski. Imaging and time stamping of photons with nanosecond resolution in Timepix based optical cameras. *Nuclear Instruments and Methods in Physics Research Section A: Accelerators, Spectrometers, Detectors and Associated Equipment*, 937:26–30, September 2019. ISSN 0168-9002. doi: 10.1016/j.nima.2019.05.034. 47

[86] Luis A. Orozco. FRANCIUM. *Chemical & Engineering News Archive*, 81 (36):159, September 2003. ISSN 0009-2347, 2157-4936. doi: 10.1021/cen-v081n036.p159. 153

[87] R. Paschotta. Gaussian Beams - an encyclopedia article. In *RP Photonics Encyclopedia*. RP Photonics AG, 2005. doi: 10.61835/mla. 40

[88] Frank L. Pedrotti, Leno M. Pedrotti, and Leno S. Pedrotti. *Introduction to Optics:*. Cambridge University Press, 3 edition, December 2017. ISBN 978-1-108-42826-2 978-1-108-55249-3. doi: 10.1017/9781108552493. 35

[89] John M. Pfotenhauer and Russell J. Donnelly. Heat Transfer in Liquid Helium. In *Advances in Heat Transfer*, volume 17, pages 65–158. Elsevier, 1985. ISBN 978-0-12-020017-7. doi: 10.1016/S0065-2717(08)70285-5. 11

[90] James D. Pickering, Benjamin Shepperson, Lars Christiansen, and Henrik Stapelfeldt. Femtosecond laser induced Coulomb explosion imaging of aligned OCS oligomers inside helium nanodroplets. *J. Chem. Phys.*, 149 (15):154306, 2018. doi: 10.1063/1.5049555. 150

[91] Johannes Poms, Andreas W. Hauser, and Wolfgang E. Ernst. Helium nanodroplets doped with xenon and rubidium atoms: A case study of van der Waals interactions between heliophilic and heliophobic dopants. *Physical Chemistry Chemical Physics*, 14(43):15158, 2012. ISSN 1463-9076, 1463-9084. doi: 10.1039/c2cp42333b. 119

[92] Monisha Rastogi, Christian Leidlmair, Lukas An der Lan, Josu Ortiz de Zárate, Ricardo Pérez de Tudela, Massimiliano Bartolomei, Marta I. Hernández, José Campos-Martínez, Tomás González-Lezana, Javier Hernández-Rojas, José Bretón, Paul Scheier, and Michael Gatchell. Lithium ions solvated in helium. *Physical Chemistry Chemical Physics*, 20(40): 25569–25576, October 2018. ISSN 1463-9084. doi: 10.1039/C8CP04522D. 4, 58, 71, 72

[93] Christian Reichardt and Thomas Welton. *Solvents and Solvent Effects in Organic Chemistry*. Wiley, 1 edition, October 2010. ISBN 978-3-527-32473-6 978-3-527-63222-0. doi: 10.1002/9783527632220. 3, 58

[94] Yanfei Ren and Vitaly V. Kresin. Surface location of alkaline-earth-metal-atom impurities on helium nanodroplets. *Physical Review A*, 76(4):043204, October 2007. doi: 10.1103/PhysRevA.76.043204. 154

[95] Michael Renzler, Matthias Daxner, Lorenz Kranabetter, Alexander Kaiser, Andreas W. Hauser, Wolfgang E. Ernst, Albrecht Lindinger, Robert Zillich, Paul Scheier, and Andrew M. Ellis. Communication: Dopant-induced solvation of alkalis in liquid helium nanodroplets. *The Journal of Chemical Physics*, 145(18):181101, November 2016. ISSN 0021-9606. doi: 10.1063/1.4967405. 20, 153

[96] G. M. Roberts, J. L. Nixon, J. Lecointre, E. Wrede, and J. R. R. Verlet. Toward real-time charged-particle image reconstruction using polar onion-peeling. *Review of Scientific Instruments*, 80(5):053104, May 2009. ISSN 0034-6748, 1089-7623. doi: 10.1063/1.3126527. 54

[97] S. Rousseau, A.R. Allouche, M. Aubert-Frécon, S. Magnier, P. Kowalczyk, and W. Jastrzebski. Theoretical study of the electronic structure of KLi and comparison with experiments. *Chemical Physics*, 247(2):193–199, August 1999. ISSN 03010104. doi: 10.1016/S0301-0104(99)00206-2. 145, 146

[98] Claude Rulliere. *Femtosecond Laser Pulses: Principles and Experiments*. Springer, 2nd edition, 2005. ISBN 0-387-01769-0. 38

[99] A. Scheidemann, J. P. Toennies, and J. A. Northby. Capture of neon atoms by He 4 clusters. *Physical Review Letters*, 64(16):1899–1902, April 1990. ISSN 0031-9007. doi: 10.1103/PhysRevLett.64.1899. 27

[100] Arne Schiller, Paul Martini, Elias Emile Jabbour Al Maalouf, and Paul Scheier. Submersion of rubidium clusters in helium nanodroplets. *The European Physical Journal D*, 75(4):124, April 2021. ISSN 1434-6079. doi: 10.1140/epjd/s10053-021-00112-9. 20

[101] Constant Schouder, Adam S. Chatterley, Melby Johny, Flora Hübschmann, Ahmed F. Al-Refaie, Florent Calvo, Jochen Küpper, and Henrik Stapelfeldt. Laser-induced Coulomb explosion imaging of (C6H5Br)2 and C6H5Br–I2 dimers in helium nanodroplets using a Tpx3Cam. *Journal of Physics B: Atomic, Molecular and Optical Physics*, 54(18):184001, October 2021. ISSN 0953-4075. doi: 10.1088/1361-6455/ac04c4. 150

[102] Constant A. Schouder, Adam S. Chatterley, Lars Bojer Madsen, Frank Jensen, and Henrik Stapelfeldt. Laser-induced coulomb-explosion imaging of the cs_2 dimer: The effect of non-coulombic interactions. *Physical Review A*, 102(6):063125, December 2020. doi: 10.1103/PhysRevA.102.063125. 101, 138

[103] C. P. Schulz, P. Claas, and F. Stienkemeier. Formation of K^*He exciplexes on the surface of helium nanodroplets studied in real time. *Physical Review Letters*, 87(15):153401, September 2001. doi: 10.1103/PhysRevLett.87.153401. 62, 63

[104] Benjamin Shepperson, Adam S. Chatterley, Anders A. Søndergaard, Lars Christiansen, Mikhail Lemeshko, and Henrik Stapelfeldt. Strongly aligned molecules inside helium droplets in the near-adiabatic regime. *The Journal of Chemical Physics*, 147(1):013946, June 2017. ISSN 0021-9606. doi: 10.1063/1.4983703. 23

[105] Alkwin Slenczka and Jan Peter Toennies, editors. *Molecules in Superfluid Helium Nanodroplets: Spectroscopy, Structure, and Dynamics*, volume 145 of *Topics in Applied Physics*. Springer International Publishing, Cham, 2022. ISBN 978-3-030-94895-5 978-3-030-94896-2. doi: 10.1007/978-3-030-94896-2. 27

[106] Henrik Stapelfeldt, Eric Constant, Hirofumi Sakai, and Paul B. Corkum. Time-resolved Coulomb explosion imaging: A method to measure structure and dynamics of molecular nuclear wave packets. *Physical Review A*, 58(1):426–433, July 1998. doi: 10.1103/PhysRevA.58.426. 100

[107] Casey Stark and Vitaly V. Kresin. Critical sizes for the submersion of alkali clusters into liquid helium. *Physical Review B*, 81(8):085401, February 2010. doi: 10.1103/PhysRevB.81.085401. 3, 20, 153

[108] James Stewart. *Calculus: concepts and contexts*. Thomson, Brooks/Cole, Belmont, Calif., 3. ed., metric int. version, student ed edition, 2006. ISBN 978-0-534-40983-8. 158

[109] F. Stienkemeier, J. Higgins, W. E. Ernst, and G. Scoles. Laser Spectroscopy of Alkali-Doped Helium Clusters. *Physical Review Letters*, 74(18):3592–3595, May 1995. doi: 10.1103/PhysRevLett.74.3592. 137

[110] Frank Stienkemeier and Kevin K. Lehmann. Spectroscopy and dynamics in helium nanodroplets. *Journal of Physics B*, 39(8):R127, 2006. ISSN 0953-4075. doi: 10.1088/0953-4075/39/8/R01. 137

[111] Jan Thøgersen, Adam S. Chatterley, Tobias Weidner, and Frank Jensen. Peptide Bond of Aqueous Dipeptides Is Resilient to Deep Ultraviolet Irradiation. *Journal of the American Chemical Society*, 145(17):9777–9785, May 2023. ISSN 0002-7863, 1520-5126. doi: 10.1021/jacs.3c01469. 59

[112] L. Tiefenthaler, J. Ameixa, P. Martini, S. Albertini, L. Ballauf, M. Zankl, M. Goulart, F. Laimer, K. von Haeften, F. Zappa, and P. Scheier. An intense source for cold cluster ions of a specific composition. *Review of Scientific Instruments*, 91(3):033315, March 2020. ISSN 0034-6748. doi: 10.1063/1.5133112. 155

[113] J. Peter Toennies and Andrey F Vilesov. Superfluid Helium Droplets: A Uniquely Cold Nanomatrix for Molecules and Molecular Complexes. *Angewandte Chemie International Edition*, 43(20):2622–2648, May 2004. ISSN 1521-3773. doi: 10.1002/anie.200300611. 4, 10, 11, 12, 13, 14, 19, 69

[114] Claire Vallance, David Heathcote, and Jason W. L. Lee. Covariance-Map Imaging: A Powerful Tool for Chemical Dynamics Studies. *The Journal of Physical Chemistry A*, 125(5):1117–1133, February 2021. ISSN 1089-5639. doi: 10.1021/acs.jpca.0c10038. 142

[115] J. Visser, M. Van Beuzekom, Henk Boterenbrood, B. Van Der Heijden, J.I. Muñoz, S. Kulis, B. Munneke, and F. Schreuder. SPIDR: A read-out system

for Medipix3 & Timepix3. *Journal of Instrumentation*, 10(12):C12028–C12028, December 2015. ISSN 1748-0221. doi: 10.1088/1748-0221/10/12/C12028. 47

[116] Benjamin J. Whitaker, editor. *Imaging in Molecular Dynamics: Technology and Applications*. Cambridge University Press, Cambridge, 2003. ISBN 978-0-521-81059-3. doi: 10.1017/CBO9780511535437. 54, 100

[117] Wikipedia contributors. Newton's law of cooling. *Wikipedia*, May 2024. 85

[118] Wikipedia contributors. Solvation. *Wikipedia*, June 2024. 1

[119] S. Zeller, M. Kunitski, J. Voigtsberger, M. Waitz, F. Trinter, S. Eckart, A. Kalinin, A. Czasch, L. Ph H. Schmidt, T. Weber, M. Schoeffler, T. Jahnke, and R. Doerner. Determination of Interatomic Potentials of He-2, Ne-2, Ar-2, and H-2 by Wave Function Imaging. *Physical Review Letters*, 121(8): 083002, August 2018. ISSN 0031-9007. doi: 10.1103/PhysRevLett.121.083002. 100

[120] Y Zhu, R R Jones, W Sandner, T F Gallagher, P Camus, P Pillet, and J Boulmer. Multiphoton double ionisation of Ba from 280 to 700 nm. *Journal of Physics B: Atomic, Molecular and Optical Physics*, 22(4):585–599, February 1989. ISSN 0953-4075, 1361-6455. doi: 10.1088/0953-4075/22/4/006. 154

[121] Eva Zunzunegui-Bru, Elisabeth Gruber, Teresa Lázaro, Massimiliano Bartolomei, Marta I. Hernández, José Campos-Martínez, Tomás González-Lezana, Stefan Bergmeister, Fabio Zappa, Paul Scheier, Ricardo Pérez de Tudela, Javier Hernández-Rojas, and José Bretón. Observation of Multiple Ordered Solvation Shells in Doped Helium Droplets: The Case of $He_N Ca^{2+}$. *The Journal of Physical Chemistry Letters*, pages 3126–3131, March 2023. ISSN 1948-7185, 1948-7185. doi: 10.1021/acs.jpclett.3c00224. 58